Anastasia Maria Patrikiadou

Modeling of thermophysical properties of hydrogen-containing mixtures with application to production, transport and storage of hydrogen

Master's thesis in Energy and Process Engineering
Supervisor: Professor Even Solbraa
Co-supervisor: Eleni Panteli
June 2023

Master's thesis

NTNU
Norwegian University of
Science and Technology

Anastasia Maria Patrikiadou

Modeling of thermophysical properties of hydrogen-containing mixtures with application to production, transport and storage of hydrogen

NTNU
Norwegian University of
Science and Technology

Acknowledgments

Abstract

As the world is grappling with an unprecedented energy and climate change crisis, it has become imperative to transition from traditional fossil fuels to alternative, sustainable energy sources with low or zero carbon footprint. Hydrogen, being a clean energy carrier with high energy content per mass, has great potential to lead the transition to clean energy. To harness hydrogen's potential, accurate knowledge of its thermophysical and thermodynamic properties is needed, in order to optimally design and operate its production, storage and transport processes. The objective of this work is to develop a simple model based on the widely used Peng-Robinson equation of state to accurately describe pure hydrogen's and hydrogen-containing-mixtures properties.

The accuracy in the description of pure hydrogen's properties such as vapor pressure, saturated liquid and vapor phase density as well as density, isobaric heat capacity, speed of sound and Joule-Thomson coefficient at supercritical temperatures, was examined with various alpha functions proposed in literature and regression of experimental data of vapor pressure and supercritical isobaric heat capacity was conducted to determine optimal parameters for the equation of state. It was concluded that Soave's alpha function with the NIST proposed acentric factor's value of -0.219 is optimal, achieving high accuracy with a low level of complexity. A comparison of the performance of the model was made with the SAFT-VRQ-Mie equation of state which incorporates quantum corrections addressing hydrogen's quantum nature. It was concluded that Peng-Robinson yields better results in the vapor pressure, saturated vapor phase density and supercritical isobaric heat capacity calculations.

The vapor-liquid equilibrium of several binary mixtures of hydrogen with compounds relevant to the hydrogen technology, such as light hydrocarbons and aromatic compounds was investigated. Experimental data was regressed to determine an optimal temperature-independent binary interaction coefficient, an optimal temperature-dependent one and a correlation was derived between the coefficient and temperature, based on the values of the optimal temperature-dependent coefficient. The introduction of a temperature dependency on the binary interaction coefficient leads to significant improvement in the accuracy of the model's bubble point pressure and vapor phase composition calculations. Furthermore, a correlation between the carbon number of normal hydrocarbons and the binary interaction coefficient was concluded, suggesting the potential development of an equation that can provide the optimal binary interaction coefficient at a given temperature and carbon number in future work. To assess the performance of the correlations derived in this work, a comparison was made with another model based on the Peng-Robinson equation of state, UMR-PRU. This involved reproducing the vapor-liquid equilibrium calculations for the binary mixtures examined and performing calculations in multicomponent systems. The analysis demonstrated that the two models yield comparable results, validating the efficiency of the derived correlations.

Key words: hydrogen, binary mixtures of hydrogen, vapor-liquid equilibrium, thermophysical properties of hydrogen, Peng-Robinson, SAFT-VRQ-Mie, UMR-PRU

Contents

List of Tables

List of Figures

Nomenclature

Latin characters

Symbol	Description
T	Temperature
P	Pressure
T_c	Critical Temperature
P_c	Critical Pressure
P^s	Vapor Pressure
d	Molar density
v	Molar volume
C_p	Molar isobaric heat capacity
w	Speed of sound
k_{ij}	Binary interaction cofficient
x_i	Liquid phase molar fraction of component i
y_i	Vapor phase molar fraction of component i
R	Universal gas constant
z	Compressibility factor

Greek characters

Symbol	Description
μ_{JT}	Joule-Thomson coefficient
ω	Acentric factor
φ	Fugacity coefficient

Abbreviations

Symbol	Description
PR	Peng-Robinson
EoS	Equation of State
cEoS	Cubic Equation of State
SRK	Soave, Redlich and Kwong
SAFT	Statistical Associating Fluid Theory
VRQ	Variable Range corrected for Quantum effects
NG	Natural Gas
C_1	Methane
C_2	Ethane
C_3	Propane
nC_4	Normal Butane
nC_5	Normal Pentane
nC_6	Normal Hexane
nC_8	Normal Octane
nC_{10}	Normal Decane
CO_2	Carbon Dioxide

cyC_6	Cyclohexane
VLE	Vapor Liquid Equilibrium
AAD	Average Absolute Deviation
NP	Number of experimental Points

Subscripts

Symbol	Description
r	Reduced
c	Critical
l	Liquid
v	Vapor
res	Residual part
id	Ideal part
tot	Total
i	Component i
ij	Cross parameter between components i and j
calc	Calculated value
exp	Experimental value

Superscripts

Symbol	Description
s	saturated

1 Introduction

1.1 Hydrogen

Hydrogen is the lightest and most abundant element on Earth. Hydrogen however, does not occur in its pure form in nature, and it is stored in water and organic compounds [1]. Under standard conditions, hydrogen is a gas that consists of two hydrogen atoms making up the hydrogen diatomic molecule H_2.

In recent years, the exacerbation of climate change and the increase in global energy demand, have placed hydrogen at the center of technological interest. Hydrogen is an energy carrier and it possesses a higher energy content per unit of mass than most conventional fossil fuels [2]. For instance, it can contain 33.33 kWh energy per kg whereas petrol and diesel can contain 12 kWh [2]. In addition, it is carbon free and when reacted in a fuel cell it leads to zero emissions, as water steam is the only by-product, making it clean. That is why it holds high potential to lead the transition to clean energy and unlock a decarbonized future.

For the transition to hydrogen's economy, accurate knowledge of the thermodynamic and thermophysical properties of pure hydrogen and hydrogen containing mixtures is required to optimally design and operate processes regarding its production, storage, transport and use.

1.1.1 Regulatory Framework

The intensification of industrialization and digitization has led to excessive greenhouse gases (GHG) emissions in the atmosphere and a growing global energy demand [3]. The use of traditional energy sources, fossil fuels, in power generation induce large amounts of GHG which aggravate global warming and therefore accelerate climate change, posing a serious threat to the planet. This alarming situation coupled with the ever-increasing energy consumption has prompted governments and organizations to take action and make pledges to reduce emissions. The United Nations have signed the Paris Agreement which binds all countries to cut back on their emissions with the ultimate goal of limiting global warming to 1.5 ^{o}C above pre-industrial levels [4]. This means that GHG emissions need to decline by 43% by 2030 and in order to achieve this target, zero-carbon solutions for power generation need to be developed and applied on a large scale [4].

An attractive option for clean energy production is utilizing renewable energy sources (RES), such as solar and wind energy. Despite their potential however, power generation from RES is unstable and highly depends on natural factors which are not within control, meaning that RES are not capable of producing as much energy needed whenever needed. That is why it is crucial to develop large scale energy storage systems. The challenge for energy storage systems is to store energy for as long as required and have the ability to supply it as fast as possible when needed [3]. That is arguably the most interesting aspect of the hydrogen technology, as hydrogen can be used as a clean storage medium for excess or intermittent renewable energy and ultimately replace traditional fossil fuels [3], [5].

Hydrogen, unlike traditional fossil fuels, is not readily available in nature for use. A primary energy source is needed to produce hydrogen and then it is used either as a fuel for direct combustion in an internal combustion engine or in a fuel cell, producing water steam [3]. Currently hydrogen is mostly produced and consumed in refineries where it is used in chemical reactions that desulfurize petroleum. Other industrial applications of hydrogen include treating metals, producing fertilizers and processing foods.

1.1.2 Hydrogen production

For hydrogen to be a true clean energy carrier, it needs to be produced with zero or low carbon footprint. Currently, there are three types of hydrogen produced:

- Gray hydrogen: hydrogen is produced from sources like natural gas, liquified petroleum gas (LPG) or naphtha using processes like steam reforming
- Blue hydrogen: carbon capture and storage technologies are applied to the production of gray hydrogen, turning it into blue hydrogen
- Green hydrogen: hydrogen is produced through electrolysis of water or by steam reforming biomass using renewable energies

The challenge of transitioning to clean energy is producing green hydrogen on a large scale. Green hydrogen production is currently very expensive and therefore investments in research into economically producing hydrogen from low-carbon-emission processes need to be made [2].

The conventional hydrogen producing technologies involve the use of fossil fuels as feedstock, the main ones being hydrocarbon reforming and pyrolysis [2]. Hydrocarbon reforming includes processes like steam reforming, when steam is used, partial oxidation, when oxygen is involved, and autothermal steam reforming, when the aforementioned processes are combined [2], [3]. The most common method applied is steam reforming of natural gas, accounting for nearly half of the production [2]. These processes result in emissions of CO as a byproduct [2]. Hydrocarbon pyrolysis involves the thermal decomposition of the hydrocarbons in the absence of oxygen and at high temperatures (around 1000 ºC), producing hydrogen and pure carbon [2].

For a lower-carbon impact, biomass can be used as feedstock to produce hydrogen. There are two kinds of processes for the treatment of biomass, classified as thermochemical and biological. The first ones are faster and more effective and involve pyrolysis, gasification, combustion and liquefaction [2], [3]. Biological processes are less energy intensive and thus more environmentally friendly as they are carried out in ambient temperature [2]. Some biological processes include bio-photolysis, dark fermentation, photo-fermentation and sequential dark and photo-fermentation [3].

Finally, hydrogen can be produced through water splitting, although currently less than 4% of the total hydrogen comes from this method, due to the high cost associated with it [2]. The main technologies employed are electrolysis, thermolysis and photo-electrolysis [2]. In electrolysis the goal is to use electricity that is derived from renewable sources so that the production of hydrogen is not accompanied by GHG emissions [2]. Water thermolysis involves the decomposition of water in very high temperatures (above 2500

^{o}C) whereas in photo-electrolysis water is split into hydrogen and oxygen due to visible light absorbance with the assistance of a photo-catalyst.

1.1.3 Hydrogen Storage

Even though hydrogen has a very high energy content per unit of mass, it is characterized by very low values of density and therefore large volumes of hydrogen are needed to store sufficient amounts of energy. That is why in order for hydrogen to be widely used and harness its potential, it is crucial to develop efficient hydrogen storage technologies.

Generally, hydrogen can be stored as a compressed gas, cryogenic liquid or solid hybride. [3]. For small-scale applications, the first two methods are usually applied. Storing it as a compressed gas requires high-pressure tanks, up to 70 Mpa, whereas storing it in its liquid form requires cooling at temperatures below 20 K, due to hydrogen's very low boiling point of 20.27 K at atmospheric pressure [2]. The problems associated with cryogenic storage of hydrogen are the high costs related to the energy required for the cooling, as well as the inevitable evaporation that occurs, resulting in high economic and energetic loss. For large-scale applications, hydrogen is stored in underground caverns. In this case, due to possible penetration of water or brine in the cavern and contact with hydrogen, it is important to have knowledge of the solubility of hydrogen in water [2]. Finally, in recent years significant developments have been made in solid-state hydrogen storage as it is safer for transportation. The main categories for solid-state hydrogen storage are based on adsorption and absorption. In the first category, hydrogen is stored in microscopic pores, cracks or tube structures of carbon nanotubes, metal organic framework etc. In the absorption techniques, metal 15ybrids are formed through chemical reactions with alloys where the atoms are absorbed into metal lattice [6].

1.1.4 Hydrogen Mixtures

An intermediate step in the journey to a zero-carbon footprint future is the combined cycle power generation, where pure hydrogen is mixed with natural gas (NG) [7]. If the hydrogen that is mixed with NG is green, the power generated has a lower carbon impact. In addition, blending hydrogen into the NG pipelines facilitates its transport, making it more accessible. The mix can be either used as an alternative fuel or it can be separated before it is used by the end-customer [2].

Another method of transporting hydrogen of great scientific interest is through pipelines by forming chemical intermediates with substances known as hydrogen carriers. Among the most popular hydrogen carriers are cycloalkanes like cyclohexane, that participate in hydrogenation and dehydrogenation reactions for the transport of hydrogen.

1.2 Objective and Scope

In the interest of enabling hydrogen to decarbonize a broad range of sectors and lead to a clean energy economy, accurate knowledge of the thermophysical and thermodynamic properties of pure hydrogen and hydrogen-containing mixtures is essential. The objective

of this work is to determine a simple model based on the widely used Peng-Robinson equation of state that is highly accurate in the calculations of pure hydrogen's properties and in the performance of VLE calculations of hydrogen binary mixtures with components of interest found in the hydrogen economy.

Peng-Robinson was selected as the basis model due to its simplicity and its wide availability on software, making the findings of this work applicable to a range of industries. The temperature range selected for the studying pure hydrogen's properties includes the saturation temperature range of 14-32 K and the supercritical temperature range of 50-1000 K, to cover a wide range of applications, from cryogenic storage that occurs at temperatures as low as 20 K, to production methods like steam reforming of methane that takes place in temperatures higher than 700 °C. In addition, the pressure range examined is extended, from 1 bar to 1500 bar, covering all applications related to hydrogen technology. The properties of interest that are within the scope of this work are presented in *Table* 1 below.

Table 1: Properties of pure hydrogen in the scope of this work

Property
Saturation Pressure
Density
Isobaric Heat Capacity
Speed of Sound
Joule-Thomson coefficient

The compounds of the binary mixtures examined in this work are the basic hydrocarbons found in natural gas, CO_2, another compound of natural gas, as well as substances associated with chemical reactions for storing and transporting hydrogen. The binary mixtures examined in this work are summarized in *Table* 2 below.

Table 2: Binary Mixtures examined in the scope of this work

Binary Mixture
$H_2 - C_1$
$H_2 - C_2$
$H_2 - C_3$
$H_2 - nC_4$
$H_2 - nC_5$
$H_2 - nC_6$
$H_2 - nC_8$
$H_2 - nC_{10}$
$H_2 - CO_2$
$H_2 - benzene$
$H_2 - toluene$
$H_2 - cyclohexane$
$H_2 - methylcyclohexane$
$H_2 - pxylene$
$H_2 - mxylene$

The experimental data of interest for the binary mixtures mentioned in *Table* 2 above regard the vapor-liquid equilibrium. The temperature and pressure range examined was determined by the available experimental data.

2 Background Knowledge

2.1 Equations of State

Equations of State (EoS) are mathematical equations that interrelate the thermodynamic variables pressure P, specific volume v and temperature T. EoS are used to calculate thermodynamic properties of both pure fluids and mixtures when a mixing rule is applied and they contain component specific parameters. In order to enhance the predictive cabilities of the EoS, these parameters are usually fitted to experimental data. An abstract form of an EoS is the following equation:

$$f(P, v, T) = 0 \qquad (Eq.\,1)$$

All equations of state constitute of a summation of Helmholtz free energy terms that account for various phenomena that occur between molecules.

Among the most popular EoS are the cubic EoS which are a cubic function of the molar volume and are widely used due to their simplicity coupled with high accuracy. The van der Waals (vdW) equation is first cubic EoS that was developed to describe the vapor-liquid equilibrium (VLE), taking into account the molecular interactions.

$$P = \frac{RT}{v - b} - \frac{a}{v^2} \qquad (Eq.\,2)$$

Where R is the universal gas constant and a and b are fluid specific parameters, referred to as "energy parameter" and "co-volume" respectively. The first one expresses the attraction between the molecules and the second one the volume of the molecules.

The first term of the equation above is the repulsive term and the second is the attractive term.

Various modifications in the vdW EoS have introduced many different cubic EoS, the general form of which is:

$$P = \frac{RT}{v - b} - \frac{a_c a(T)}{(v + \delta_1 b)(v + \delta_2 b)} \qquad (Eq.\,3)$$

Where δ_1 and δ_2 are constants dependent on the EoS, α_c and b are dependent on the EoS and the critical properties (critical temperature T_c and critical pressure P_c of the fluid) and $\alpha(T)$ is the temperature dependency of the attractive term.

2.2 Peng-Robinson Equation of State

In this work, the Peng-Robinson (PR) cubic EoS is used, the constants of which are presented below in *Table 3*.

Table 3: Peng-Robinson EoS constants

δ_1	$1 + \sqrt{2}$
δ_2	$1 - \sqrt{2}$

α_c	$\dfrac{0.45724R^2T_c^2}{P_c}$
b	$\dfrac{0.07780RT_c}{P_c}$
$\alpha(T)$	$\left(1 + m\left(1 - \sqrt{\dfrac{T}{Tc}}\right)\right)^2$
m	$0.37464 - 1.54226\omega - 0.26992\omega^2$

where ω is the acentric factor of the fluid.

Peng-Robinson is the most widely used EoS in the industry. It has been extensively studied and because of its simplicity coupled with good performance on a wide range of components and types of mixtures, it has been established as one of the most popular EoS in industrial applications.

2.3 Alpha functions

In order to improve the performance of the EoS in predicting the thermodynamic properties of fluids, various modifications in the attractive term have been introduced. The alpha functions $\alpha(T)$ proposed in literature can be classified in two categories: component-dependent and generalized [8]. To apply the component-dependent ones, experimental data must be regressed to obtain the parameters, while generalized alpha functions require the acentric factor ω as input to calculate the coefficients [8]. Generalized alpha functions can thus be applied to any component regardless of availability of experimental data but are generally less accurate than component-dependent ones.

In this work, the alpha functions proposed by Soave [9], Mathias and Copeman [10] and Twu et al. [11] were examined. The alpha function of Soave is the one that PR was originally introduced with by Peng and Robinson. *Table* 4 below summarizes the different alpha functions used in this work and their relationship with the acentric factor.

Table 4: Alpha functions examined in this work

PR	$\alpha = \left[1 + m\left(1 - \sqrt{T_r}\right)\right]^2$
	$m = 0.37464 + 1.54226\omega - 0.26992\omega^2$
PRMC	$\alpha = \left[1 + c_1\left(1 - \sqrt{T_r}\right) + c_2\left(1 - \sqrt{T_r}\right)^2 + c_3\left(1 - \sqrt{T_r}\right)^3\right]^2, T_r \leq 1$
	$\alpha = \left[1 + c_1\left(1 - \sqrt{T_r}\right)\right]^2, T_r \geq 1$
	$c_1 = 0.1316\omega^2 + 1.4031\omega + 0.3906$
	$c_2 = -1.3127\omega^2 + 0.3015\omega - 0.1213$
	$c_3 = 0.7661\omega + 0.3041$
PRTwu	$\alpha = T_r^{N(M-1)}\exp\left[L(1 - T_r^{NM})\right]$

Where T_r is the reduced temperature (T/T_c).

Soave's expression was obtained by fitting vapor pressure and extrapolating in the supercritical region [12].

Mathias and Copeman alpha function is inspired from Soave's expression and belongs to the so-called "polynomial" alpha functions as they are a polynomial function of the square root of the reduced temperature.

For the exponential type alpha function of Twu, the parameters *L*, *M*, *N* are component specific and in the original work of Twu et al. the values of them had been determined by regressing pure component vapor pressures, but no values were proposed for pure hydrogen [11].

2.3.1 Consistency of alpha functions

Most of the alpha functions proposed in literature have been developed by regressing data in the subcritical region and supercritical evaluations are performed by extrapolation. In order to improve accuracy in the supercritical domain, some authors have used different parameters for the subcritical and the supercritical regions, leading to discontinuities of the alpha function and its derivatives near the critical point [8]. These inconsistencies result in discontinuities in residual enthalpies and heat capacities calculations at the critical temperature [8]. In the work of Le Guennec et al. some criteria have been developed to ensure the consistency of the alpha functions. These consistency criteria are presented in *Table* 5 below.

Table 5: Consistency Criteria for alpha functions

$\alpha(T) \geq 0$	When the attraction between the molecules increases, the pressure of the system decreases, thus the attractive term of the EoS must be negative.
α continuous	The alpha function should be continuous
$\lim\limits_{T \to \infty} a(T) \neq \infty$	The alpha function should be constant at the infinite temperature limit
$d\alpha/dT \leq 0$	The first derivative must exist and be continuous for any temperature value. As temperature decreases, the molecules have lower kinetic energy so the energy parameter is lower.
$d^2\alpha/dT^2 \geq 0$	The second derivative must exist, be continuous and the alpha function must be convex for any temperature value to avoid discontinuities in calculated properties.
$d^3\alpha/dT^3 \leq 0$	This condition must be met for any temperature value

2.4 Volume Translation

Cubic EoS are known to not accurately estimate liquid densities. In order to improve the efficiency of such Equations, Peneloux et al. proposed the introduction of a correction on the results of the EoS, known as volume translation. It was found that in temperatures away from the critical point, the deviation between the experimental value of the volume and the calculated value is fairly constant, and therefore it is a common practice to subtract a constant, temperature-independent, value from the calculations to match the experimental data more accurately [13]. It has been concluded that the introduction of a volume translation leads to significant improvements in reduced temperatures less than 0.8 [13]. The volume translation does not interfere with the phase equilibrium. *Equation 4* below demonstrates the use of a volume translation.

$$v_{translated} = v_{EoS} - c \qquad (Eq.4)$$

where c is the volume translation value.

2.5 Mixing Rules

To extend equations to mixtures, mixing rules are used to calculate the mixture's parameters. The most commonly used are the Van der Waals one-fluid which are described through *Equations 5-8*:

$$a = \sum_i \sum_j x_i x_j \alpha_{ij} \qquad (Eq.5)$$

$$b = \sum_i \sum_j x_i x_j b_{ij} \qquad (Eq.6)$$

$$a_{ij} = (1 - k_{ij})\sqrt{a_i a_j} \qquad (Eq.7)$$

$$b_{ij} = \frac{b_i + b_j}{2} \qquad (Eq.8)$$

Where x_i, x_j are the molar fractions of components i and j respectively, a_i and b_i are the pure component EoS parameters and k_{ij} is the binary interaction coefficient. The binary interaction coefficient is usually fitted to experimental VLE data, as is the case in this work.

2.6 UMR-PRU

The UMR-PRU model was developed by Voutsas et al. [14] by coupling the Peng-Robinson EoS with the UNIFAC activity coefficient model [15] via the Universal Mixing Rules. This model is classified as a group contribution model. UMR-PRU is formulated by *Equations 9* and *10*.

$$\frac{a}{bRT} = \frac{1}{A}\left(\frac{G^E_{comb-SG} + G^E_{residual}}{RT}\right) + \sum_i x_i \frac{a_i}{b_i RT} \qquad (Eq.9)$$

$$b = \sum_i \sum_j x_i x_j \left(\frac{b_i^{0.5} + b_j^{0.5}}{2}\right)^2 \qquad (Eq.10)$$

where $G^E_{comb-SG}$ and $G^E_{residual}$ are the Staverman-Guggenheim term of the combinatorial, and the residual part of the UNIFAC activity coefficient model, respectively and A is a parameter equal to -0.53 for the PR EoS. For the determination of the residual excess Gibbs energy the temperature-dependent UNIFAC binary interaction parameter Ψ_{mn} between groups m and n is calculated.

$$\Psi_{mn} = \exp\left[-\frac{A_{mn} + B_{mn}(T - 298.15) + C_{mn}(T - 298.15)^2}{T}\right] \qquad (Eq.11)$$

where A_{mn}, B_{mn}, C_{mn} are adjustable parameters obtained by fitting binary phase equilibrium data [16].

For the application of UMR-PRU to hydrogen containing systems, hydrogen H_2 is considered a separate UNIFAC group. The parameters between H_2 and other groups were determined by regression of VLE data of binary mixtures [16].

2.7 SAFT-VRQ-Mie

The other very popular family of equations other than the cubic one, is the Statistical Associating Fluid Theory (SAFT) one. SAFT models utilize statistical thermodynamics to describe fluids with non-spherical molecules. In this work the model SAFT-VRQ-Mie (Statistical Associating Fluid Theory for Mie potentials of Variable Range corrected for Quantum effects) developed by Aasen et al. [17] was selected for performing calculations due to the incorporation of quantum corrections. This model was originally developed for cryogenic fluids such as hydrogen and it is a combination of the third-order-Barker-Henderson expansion of the Helmholtz energy with Mie potentials including first and second order (Mie-FH1 and Mie-FH2) Feynman-Hibbs quantum corrections [17]. The equation takes into account the contribution of segment, dispersion, chain and association Helmholtz energy.

$$a^r = a^{seg} + a^{disp} + a^{chain} + a^{assoc} \qquad (Eq.12)$$

where a^r, a^{seg}, a^{disp}, a^{chain}, a^{assoc} are the residual, segment, dispersion, chain and association reduced Helmholtz energy

The model has been extended for application in mixtures [18].

2.8 Phase Equilibrium

A system is in thermodynamic equilibrium when its Gibbs energy has the minimum value at a given temperature and pressure [19].

$$[dG]_{T,P} = 0 \qquad (Eq.13)$$

The Gibbs function is defined in *Equation 14*.

$$G = H - TS = U + PV - TS \qquad (Eq.14)$$

Where H is the enthalpy, S the entropy, U the internal energy and V the volume.

In a system consisting of two phases of a pure substance equilibrium is achieved when the Gibbs functions of the phases are equal [19].

2.8.1 Phase Equilibrium for mixtures

Phase equilibrium between a vapor and a liquid phase (VLE) is expressed through *Equation 15*:

$$\widehat{f_i^v} = \widehat{f_i^l}$$

$$y_i \widehat{\varphi_i^v} P = x_i \widehat{\varphi_i^l} P \qquad (Eq.15)$$

where $\widehat{f_i^v}$ and $\widehat{f_i^l}$ are the fugacities of component I in the vapor and liquid phase respectively, $\widehat{\varphi_i}$ is the fugacity coefficient of component i, y_i is the vapor phase fraction of component i and x_i is the liquid phase fraction of component i.

The fugacity coefficient is calculated with Peng-Robinson EoS through *Equation 16*.

$$ln\varphi_i = \frac{b_i}{b}(z - 1) - \ln(z - b) - \frac{a}{2b\sqrt{2}}\left(\frac{2\sum x_j a_{ij}}{a} - \frac{b_i}{b}\right)\ln\left(\frac{z + 2.414b}{z - 0.414b}\right) \qquad (Eq.\,16)$$

where z is the compressibility factor of a substance

2.8.2 Vapor Pressure

The vapor pressure P^s, is defined as the maximum pressure exerted by the vapor molecules in a vapor-liquid equilibrium (VLE) in a given temperature in a closed container. It expresses the tendency of a material to convert into the gaseous or vapor state and it increases with temperature, as the molecules' internal energy increases and they move faster and more of them have sufficient energy to go in the vapor phase [20].

In order to determine the vapor pressure of a pure substance using the Peng-Robinson EoS, the fugacity coefficient has to be calculated and then the vapor pressure is calculated through *Equation 17*.

$$P^S = \varphi P \qquad (Eq.\,17)$$

2.9 Properties

The properties examined in this work are the molar density, the isobaric heat capacity, the speed of sound and the Joule-Thomson coefficient.

2.9.1 Molar density

The molar density of a pure substance can be calculated through *Equation 18*.

$$\rho = \frac{1}{v} = \frac{P}{zRT} \qquad (Eq.\,18)$$

Where z is the fluid's compressibility factor at a certain temperature T and pressure P.

Accurate knowledge of the molar density of hydrogen is highly important for the optimal design of storage and transportation processes as it allows proper determination of the required volume of storage systems. Knowing the density, the required volume of storage systems can be determined. In addition, it is important for the optimization of certain power generation processes as the density affects the rate of diffusion to the electrode of a fuel cell as well as the air-fuel ratio in hydrogen-fueled engines. Finally, accurate knowledge of the density allows the calculation of the frictional pressure loss inside a pipe.

2.9.2 Isobaric heat capacity

The isobaric heat capacity is the first derivative of enthalpy H with respect to temperature for a substance undergoing an isobaric process (a process with constant pressure) [19].

It expresses the amount of thermal energy required to shift the temperature of a substance at current pressure.

$$C_p = \left(\frac{\partial H}{\partial T}\right)_P \qquad (Eq.\,19)$$

The isobaric heat capacity is dependent on temperature and in general it increases as temperature increases. In gases this is explained due to the increased activity in higher temperatures in translational, vibrational and rotational motions in the molecules, meaning greater internal energy.

There are many equations proposed to calculate the isobaric heat capacity for an ideal gas, most of them are polynomial and in the form of power series with respect to temperature. A general form is presented in *Equation 20*.

$$C_{p,id} = a + bT + cT^2 + dT^3 + \cdots \qquad (Eq.\,20)$$

The parameters a, b, c, d, etc are component dependent and each set of equation with parameters proposed is only applicable to a certain temperature range.

To calculate the isobaric heat capacity for a real, non-ideal gas, a contribution for the non-ideal part must be added. This contribution accounts for the deviation from ideal conditions, and it is known as the residual property which is calculated from the EoS.

$$C_p = C_{p,id} + C_{p,res} \qquad (Eq.\,21)$$

Efficient calculations of the isobaric heat capacity of hydrogen are very important for the optimal design of heat transfer processes performed in fuel cells and combustion engines. Detailed knowledge of this property allows proper sizing of heat exchangers, determination of energy requirements and safe operation of relevant processes.

2.9.3 Speed of sound

The speed of sound w is defined as the distance traveled by sound waves as they propagate through a material per unit of time. It is a thermodynamic property relevant to the isentropic compressibility of a fluid and it is calculated from *Equation 22* [19].

$$w = \left[\left(\frac{\partial d}{\partial P}\right)_s\right]^{-\frac{1}{2}} \qquad (Eq.\,23)$$

Equation 23 assumes small pressure changes and negligible viscosity effect.

Knowledge of the speed of sound is very important to determine whether the flow of a fluid is compressible or incompressible, so that the appropriate fluid dynamics equations can be applied. The type of flow is determined through calculation of the Mach number M, as shown in *Equation 24.* The flow is defined as incompressible for Mach number values less than or equal to 3, and compressible for greater values.

$$M = \frac{u}{w} \qquad (Eq.\,24)$$

where u is the fluid's speed velocity.

In addition, knowledge of the speed of sound of hydrogen is crucial for safety in hydrogen related processes. Hydrogen is a highly flammable gas and possible leaks need to be identified as soon as possible. Measurements of the speed of sound in hydrogen-containing pipelines can indicate such leaks if deviations from the normal values are observed. Deviations can also signify the presence of hydrates and other physical obstacles in pipelines. Finally, the speed of sound is very important for monitoring the gas flow in pipelines, as it allows knowledge for their maximum velocity. For high velocity gas flows, the fluid can be compressible, meaning that the density is no longer constant. Compressibility affects the stability of flow and can lead to pressure fluctuations. Furthermore, very high gas velocities can cause damage to the equipment used.

2.9.4 Joule-Thomson coefficient

The Joule-Thomson coefficient expresses the effect of pressure on temperature change during a throttling process [19]. Its mathematical formula is given in *Equation 25*.

$$\mu_{JT} = \left(\frac{\partial T}{\partial P} \right)_h \qquad (Eq.\,25)$$

The Joule-Thomson coefficient is zero for ideal gases and for real ones it can be positive or negative. All real gases have an inversion point at which the value of the coefficient changes sign.

At room temperature, all gases except hydrogen, helium and neon cool upon isenthalpic expansion, meaning that hydrogen has a negative Joule-Thomson coefficient at such temperatures.

As the triple point of hydrogen is extremely low, at 13.95K, liquefaction for storage occurs at very low temperatures and estimation of temperature changes associated with the expansion or throttling of the gas is critical. That is why the knowledge of the Joule-Thomson coefficient is crucial for the efficiency of cryogenic processes. Moreover, it is important for hydrogen-natural gas blends processing, as different temperature changes occur in the components of the mixture when it undergoes a throttling process which can lead to partial condensation or separation of the compounds.

2.10 Hydrogen's quantum nature

Hydrogen has two spin isomers, para-hydrogen and ortho-hydrogen. The difference between the two allotropes is the relative orientation of the nuclear spin of the individual atoms forming the molecule. In the parahydrogen molecule the spin of the two atoms is in opposite directions (anti-parallel) whereas in the orthohydrogen molecule it is in the same direction (parallel). The spin orientation relative to the individual nuclei of the molecule affects the rotational state of the molecule and thus the energy level. Para-hydrogen has lower energy levels and is predominant at lower temperatures and ortho-hydrogen's higher energy levels make it predominant in higher temperatures [21].

Hydrogen may therefore be regarded as a binary mixture of two different molecules with different properties [21]. The property differences in the two forms are greater in caloric properties, such as isobaric heat capacity. This is due to the difference in their rotational energies as mentioned above. The equilibrium composition of the mixture is temperature-dependent. In room temperatures hydrogen consists of approximately 75%

orthohydrogen and 25% parahydrogen. When hydrogen is made up of this ratio it is referred to as "normal". As mentioned above, parahydrogen is predominant in lower temperatures due its lower energy level. At 0 K hydrogen is pure parahydrogen and as temperature increases the mixture's composition is shifting slowly to contain more orthohydrogen until the mixture reaches the 3:1 ratio [21], [22].

2.11 Literature Review

The thermophysical and thermodynamic properties of pure hydrogen and hydrogen-containing mixtures have been discussed extensively in literature. Collection of experimental data began as early as the 1930s and since then a lot of Equations of State have been developed to accurately describe hydrogen's behavior.

Among the most important EoS in literature is the one developed by Younglove in 1982 for parahydrogen [23]. The modeling was derived from experimental data obtained by the van der Waals Laboratory in 1941 and 1959 and it is based on the modified Benedict-Webb-Rubin (mBWR) form, an early EoS for the description of real fluids. The application range for the Younglove EoS is 14-400 K for temperature and up to 121 MPa for pressure.

The Younglove EoS used to be the reference equation of state for hydrogen, used in NIST's standard properties package REFPROP [2] but it has been replaced with the EoS proposed by Leachman et al. in 2009 [22]. Leachman et al. developed three EoS, for ortho-, para- and normal hydrogen, expressed in terms of Helmholtz free energy. These equations are valid from the triple point (13.957 K) up to 1000 K and for pressures up to 2000 MPa.

As described in Section 2.10 above, the quantum nature of hydrogen prompts the need for implementing quantum corrections in the models used to describe its behavior. In 2019 Aasen et al. [17] introduced the SAFT-VRQ-Mie model which was focused on cryogenic gases, helium, hydrogen, neon and deuterium. In their work they have made comparisons between SAFT-VRQ-Mie, the Leachman EoS and a volume-shifted Soave-Redlich-Kwong (SRK) EoS. This comparison demonstrates the improvement from the volume-shifted SRK and the high accuracy of the model in relation to the reference EoS of Leachman, especially in saturated densities and pressures as well as in supercritical densities, isobaric heat capacities and speeds of sound. The only property that exhibits a larger deviation is the saturated liquid isobaric heat capacity. Aasen et al. later in 2020 extended SAFT-VRQ-Mie to be applicable to cryogenic mixtures [18].

Aasen et al. [24] have also introduced quantum corrections to the classic EoS of PR and SRK to accurately predict the thermodynamic properties of hydrogen, helium, neon, deutereium and their mixtures. In their work they point out hydrogen's non classical alpha function behavior and the need for an introduction of a temperature dependency of the covolume to account for quantum swelling [24]. They therefore derived temperature-dependent quantum corrections for the covolume parameter based on the quantum swelling of the Feynman-Hibbs-corrected Mie and employed Twu's alpha function and a volume translation to produce EoS with high accuracy in subcritical and supercritical properties.

Regarding mixtures of hydrogen with natural gas components, the reference EoS, used for a variety of technical applications, is the multicomponent GERG equation. The original GERG-2004 equation was developed by Kunz et al. for natural gases and other mixtures and it was published in 2007. As stated in their work, the model uses fundamental EoS for each pure component and they have developed formulations for the application to binary mixtures, taking into account the residual mixture behavior [25]. Specifically for hydrogen, a new EoS was developed by conducting fittings on a variety of properties and employing optimisation methods explained in their work. It is important to note that due to a lack of experimental data for low temperatures, below 100 K, some of the data used in the development of the model have been produced from previously developed EoS [25]. The derived EoS for hydrogen is valid for pressures up to 300 MPa and it yields similar or improved results in the description of thermodynamic properties compared to mBWR models. In their work they point out the weakness of Younglove's equation to produce physically correct results in the liquid phase and in the liquid-like supercritical region at very high densities [25].

In 2012, Kunz et al. [26] published an extension of the GERG-2004 model, the GERG-2008 which included three new components, bringing the total number of compounds the model can be applied to, to 21. The suggested valid temperature range is 90-450 K depending on the compounds examined, and the pressure range is up to 35 MPa. An extension to 60-700 K and up to 70 MPa is also claimed to lead to accurate results. The GERG-2008 EoS can be used both for pure hydrogen and hydrogen mixtures.

UMR-PRU, which was developed by Voutsas et al. in 2004 [14], has been extensively used for calculations regarding natural gas mixtures. In 2019 Koulocheris et al. [16] extended UMR-PRU to hydrogen containing systems and was used to describe VLE in binary and multicomponent mixtures. A comparison was also made with another group contribution model, PPR78 developed by Qian et al. [27] in 2012. PPR78 is based on the Peng-Robinson EoS and it determines temperature-dependent binary interaction coefficients through a group-contribution method [27]. In the work of Koulocheris et al. they conclude that both models are efficient in VLE descriptions although UMR-PRU yields lower deviations from experimental data.

Due to the fact that hydrogen mixtures with hydrocarbons and other heavier compounds are highly asymmetric, classic EoS fall short in the accurate prediction of the mixtures' phase equilibrium.

El-Twaty and Prasunitz [28] have found been found that using the covolume as it has been originally proposed in *Equation 6* above, for mixtures of hydrogen with heavy hydrocarbons, the k_{ij} values obtained from fitting experimental data are unrealistically large, and can be even greater than 1, rendering the energy parameter with no physical meaning as it becomes negative. They also found in their work that asymmetric systems are highly influenced by the covolume parameter value, more than by the energy parameter and thus proposed the introduction of a binary parameter E_{Hj} in the covolume parameter which was fitted to binary VLE data [28].

Other researchers have also suggested more complex mixing rules (Wang and Zhong, 1989 [28], Huang et al., 1994 [29], Ioannidis and Knox, 1999 [30]) or modifications in the

energy parameter of popular cubic EoS (Twu et al.,1996 [31], Mohammed et al., 2018 [32]).

There are several papers published in literature that have conducted a review of available thermodynamic models. A very recent one is by Lozano-Martín et al. published in 2022 [2], where both experimental data for hydrogen mixtures and models are reviewed. In their work they have compiled experimental data on VLE for the binary mixtures of hydrogen with CH_4, N_2, CO_2, C_2, C_3, nC_4, iC_4, nC_5, nC_6, CO, H_2O, H_2S, He, Ar, Ne and NH_3, density and compressibility factors data for the mixtures with CH_4, C_2, C_3, nC_4, nC_5, nC_6, N_2, CO_2, CO and Ar and finally speed of sound and other caloric properties for the mixtures with CH_4, N_2, O2, CO_2, He and Ar.

In the work of Sakoda et al. [20] several EoS developed for hydrogen are presented and the uncertainties of the most notable ones, namely McCarty and Weber, Younglove and Leachman, are examined in regards of deviations from experimental data. They conclude that the EoS of Leachman exhibits the smallest uncertainty although all three EoS perform very well. More specifically, they exhibit no more than 1% uncertainty in densities and varying uncertainties in the other properties such as heat capacities, speed of sound etc. McCarty and Weber exhibits a maximum deviation of 10% for such properties in extrapolated areas below 100 K, whereas the property with the largest uncertainty for the Younglove and Leachman EoS is the heat capacity, with maximum values of 3.0% and 0.5% respectively. In their work Sakoda et al. also evaluate the EoS of Leachman, Younglove and Kunz in their performance making calculations on PVT, VLE, isobaric heat capacity and speed of sound by making comparisons with experimental data. The high accuracy of the EoS of Leachman are deduced from this analysis.

3 Pure hydrogen

The great potential hydrogen has to lead the clean energy transition makes the accurate prediction of its behavior a necessity in order to design, optimize and operate its processes. Due to its quantum nature, the prediction of pure hydrogen's properties in low temperatures is especially challenging and thus modifications in current thermodynamic models are needed. In this work, the classic cubic EoS Peng-Robinson is used to predict pure hydrogen's properties and certain reparameterizations are conducted to increase the model's accuracy. Peng-Robinson, however, is an equation that does not take into account the quantum nature of hydrogen and for comparison reasons, the model SAFT-VR-Q-Mie, which has been developed with quantum corrections, is also applied. The models examined and the software used are demonstrated in *Table 6* below.

Table 6: Thermodynamic models examined and software used

Thermodynamic Model	Software
Peng-Robinson	ThermoCalc-MSVS
SAFT-VRQ-Mie	Python

In this work, the performance of the thermodynamic models is evaluated against the experimental data provided by the NIST database. The triple point and the critical conditions were also retrieved from the same database, for fare comparison reasons. The triple point temperature and the critical conditions are presented in *Table 7*.

Table 7: Triple point and critical conditions of H_2

Triple Point Temperature T_{triple}	13.95	K
Critical Temperature T_c	33.145	K
Critical Pressure P_c	12.694	bar

3.1 Soave alpha function: Acentric factor comparison

The first objective of this work was to compare the two acentric factor values proposed by NIST and Aspen HYSYS. The two values are given in *Table 8* below.

Table 8: Acentric factors of pure H_2 proposed by NIST and Aspen HYSYS

Source	Value
NIST	-0.219
Aspen HYSYS	-0.120

It is important to note here that Aspen HYSYS performs calculations for hydrogen and helium by modifying their critical temperature. This means that the subcritical and supercritical regions are constantly changing and that makes comparison of calculations complicated. The purpose of this work is to develop a very simple model that has high accuracy in both the subcritical and supercritical regions, so it is important to obtain a single acentric factor.

3.1.1 Subcritical region

The calculations for the subcritical region were performed in the temperature range of 14-32 K. Calculations were made for both acentric factors in *Table 8* above and in the software ThermoCalc-MSVS for the saturated pressure, the saturated liquid volume and the saturated vapor volume. The experimental points shown in the graphs are retrieved from the NIST database. The comparison between the calculations is presented in *Table 9* below. The average deviation (%AAD) is calculated through the formula in *Equation* 26.

$$\%AAD = 100\% \frac{\sum_1^{NP} \frac{\left|X_{exp} - X_{calc}\right|}{X_{exp}}}{NP} \qquad (Eq.\,26)$$

Where X_{exp} is the experimental value of property X, X_{calc} is the calculated value of the property and NP is the total number of points calculated.

Table 9: %AAD for saturation properties of pure hydrogen using acentric factor proposed by NIST and by Aspen HYSYS

ω	%AADP^s	%AADd$_l$	%AADd$_v$
-0.219 (NIST)	4.0	19.7	6.0
-0.12 (Aspen HYSYS)	24.3	25.1	25.6

Saturation Pressure

The saturated pressure calculations P^s and their comparison to the experimental values are visualized below in *Figure 1*.

It can be easily observed that the calculations using the acentric factor proposed by Aspen HYSYS underestimate the value of the saturated pressure for the entire temperature range. In contrast, the calculations with the ω proposed by HYSYS underestimate the P^s initially, up to 19 K and then they overestimate it.
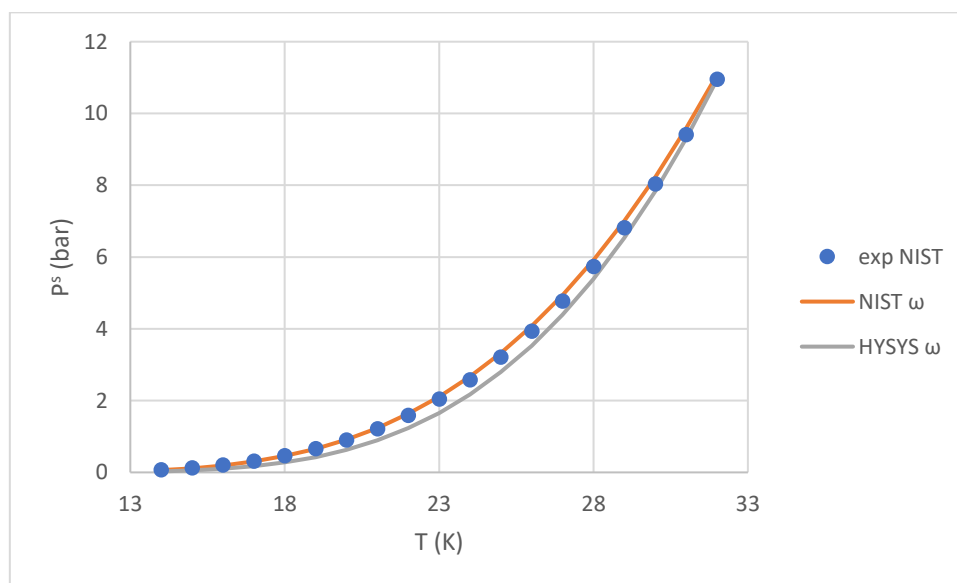
Figure 1: Saturation pressure calculations for pure hydrogen using acentric factor proposed by NIST and by Aspen HYSYS

Figure 2 below illustrates the %AAD in the vapor pressure as a function of temperature. It is very clear that the deviations are very high at low temperatures below 18 K. The calculations made with the Aspen HYSYS ω show decreasing deviations as temperature increases. The calculations made with the ω proposed by NIST show a similar behavior up until 20 K where an inversion in the trend of the prediction is observed, from underestimating to overestimating. After 20 K the deviation increases with temperature but remains under 4%.
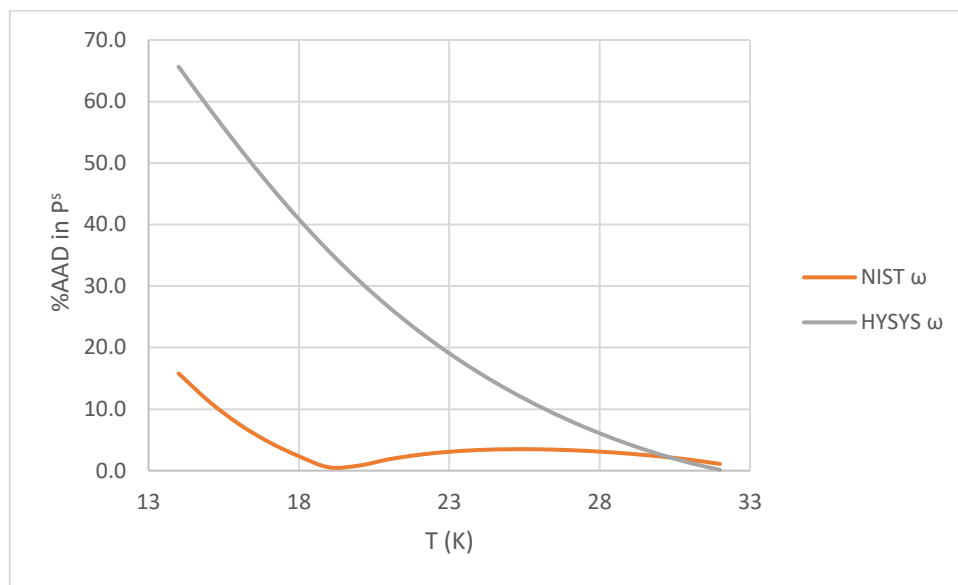
Figure 2: %AAD in saturated pressure as a function of temperature for pure hydrogen

Saturated Liquid Density

Similarly to the vapor pressure, the saturated liquid density d_l is calculated more accurately when the ω proposed by NIST is used. The saturated liquid volume calculations and comparison to the experimental values are visualized below in *Figure* 3.
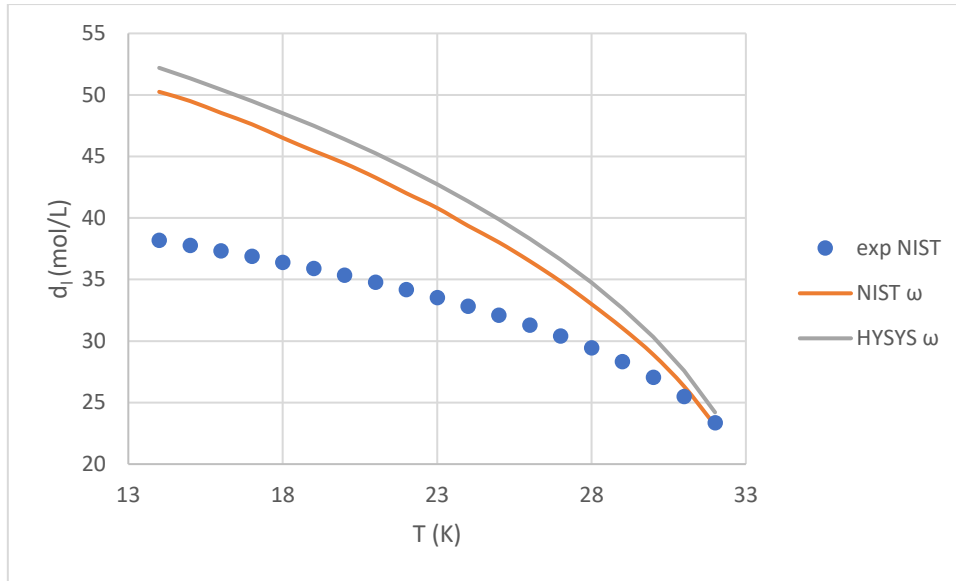
Figure 3: Saturation liquid density calculations for pure hydrogen using acentric factor proposed by NIST and by Aspen HYSYS

For both sets of calculations performed with the different ω values, an overestimation of the saturated liquid density is observed for the entire temperature range. This deviation is very prominent at the lower temperatures and progressively decreases as temperature increases to reach the critical point. The large deviations in the calculated values suggest the need for a volume translation.

The observations above are visualized in *Figure* 4 below where it can be confirmed that the deviations are significantly reduced near the critical point.
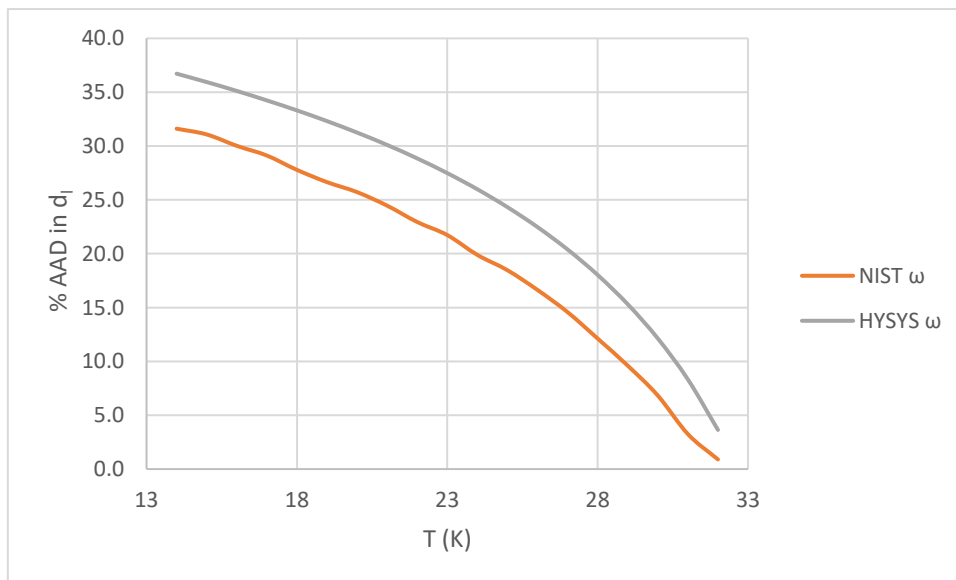
Figure 4: %AAD in saturated liquid density as a function of temperature for pure hydrogen

Saturated Vapor Density

Finally, the calculations in the saturated vapor density d_v made with the NIST proposed ω are superior to the ones made with the Aspen HYSYS proposed one.

The saturated vapor density calculations and their comparison to the experimental values are visualized below in *Figure* 5.
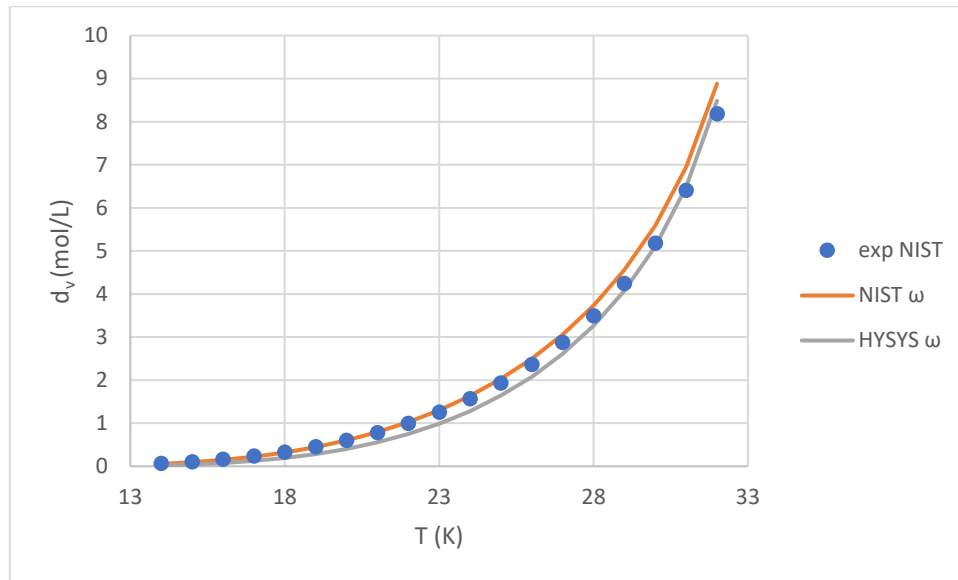
Figure 5: Saturated vapor density calculations for pure hydrogen using acentric factor proposed by NIST and by Aspen HYSYS

As expected, the calculations for the saturated vapor density are much more accurate than for the liquid phase.

As far as the NIST ω calculations are concerned, in lower temperatures the d_v is underestimated and in higher ones, it is overestimated. The change in this trend occurs around 20-21 K and this is the point of the lowest AAD. In contrast, the Aspen HYSYS ω calculations underestimate the d_v value for a larger temperature range, and there is an overestimation only near the critical point.

To better examine the accuracy of the models the AAD as a function of temperature is plotted in *Figure* 6 below.
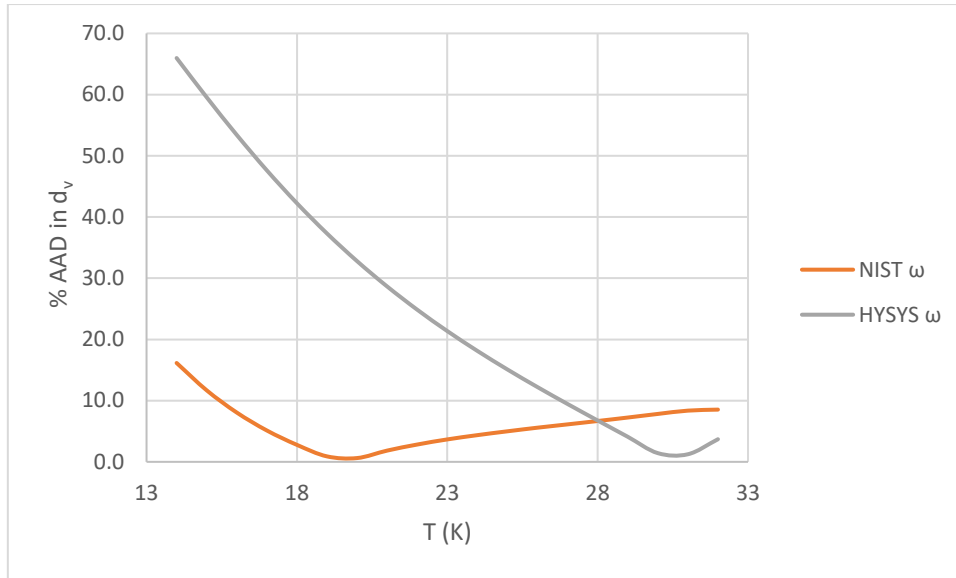
Figure 6: %AAD in saturated vapor density as a function of temperature for pure hydrogen

From *Figure 6* it can be observed that the deviations are higher at the lower temperatures, but do not reach a minimum near the critical point, in contrast to the saturated pressure and the saturated liquid density. Regarding the NIST ω calculations, the deviation is initially high in the low temperatures, reaches a minimum around 20 K and then the deviation increases with temperature but remains under 10%. Regarding the Aspen HYSYS ω calculations demonstrate a decreasing deviation as temperature increases and it is minimized around 31 K, very near the critical point.

It is important to note that at temperatures above 28 K the prediction with the Aspen HYSYS ω is actually better compared to the NIST one.

The analysis above regards the direct comparison between the two values for the acentric factor. Due to the modified T_c of hydrogen in the Aspen HYSYS software when performing calculations, the results obtained from the software are different, although not highly accurate. The relative deviations in percentages are presented in *Table* 10 below.

Table 10: %AAD in saturated pressure, saturated liquid density and saturated vapor density in calculations for pure hydrogen obtained from Aspen HYSYS

Property	%AAD
P_s	27.6
d_l	7.4
d_v	33.4

3.1.2 Supercritical Region

The properties calculated for pure hydrogen in the supercritical area are the density d, the isobaric heat capacity Cp, the speed of sound w and the Joule-Thomson coefficient μ_{JT}. The calculations were performed for a temperature range of 50-300 K in a 50 K step and for 400-1000 K in a 100 K step. The pressure range is 1-1500 bar. A smaller step in the

temperature intervals was chosen due to higher deviations from the experimental values of the calculated properties in the lower temperatures.

Supercritical Molar Density

Table 11 below lists the average deviation (%AAD) in the calculated density in each of the isothermal curves examined, for both sets of calculations with the different acentric factors.

Table 11: %AAD in supercritical density calculations for pure hydrogen using acentric factor proposed by NIST and by Aspen HYSYS

T (K)	%AAD in d (NIST ω)	%AAD in d (Aspen HYSYS ω)
50	8.0	6.2
100	6.2	2.8
150	5.4	2.0
200	4.7	1.5
250	4.0	1.2
300	3.4	0.9
400	2.5	0.6
500	1.9	0.4
600	1.4	0.3
700	1.0	0.2
800	0.7	0.3
900	0.5	0.4
1000	0.4	0.4
Overall	**3.0**	**1.3**

According to *Table* 11, it is clear that as the temperature increases, the average deviation in the calculations is lower, and thus Peng-Robinson can predict pure hydrogen's supercritical density with higher accuracy in the high temperatures. Up to the temperature of 800 K, the use of the acentric factor value proposed by Aspen HYSYS leads to better results in the prediction of the density. In the lower temperature range of 100-600 K especially, the prediction using the ω proposed by Aspen HYSYS leads to more than half the average deviation compared to using the NIST ω. In very high temperatures however, above 900 K, the use of the ω proposed by NIST is optimal. Overall though, at temperatures of 700 K and up, the deviation with both models is very small, no more than 1%.

For a more detailed analysis, *Figure* 7 is presented where calculations for some isothermal curves have been plotted as a function of pressure.
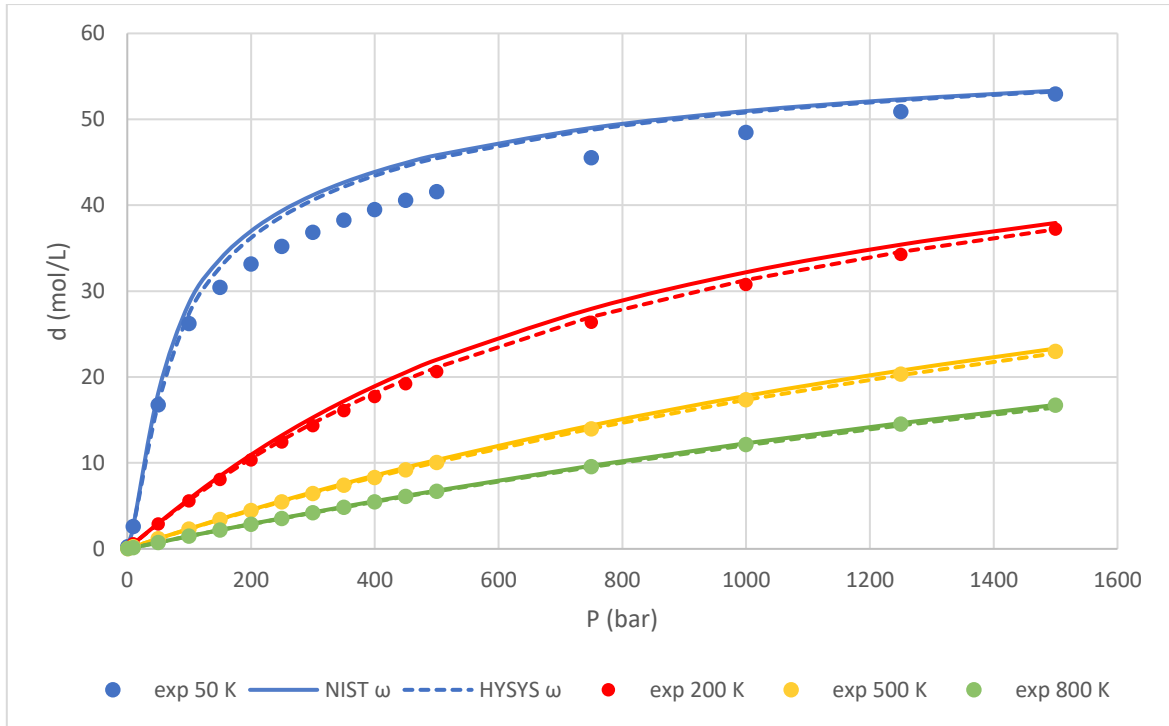
Figure 7: Supercritical molar density calculations for pure hydrogen in isothermal curves of 50, 200, 500 and 800 K as a function of pressure

From the *Figure* 7 above it is shown that the prediction is significantly improved as the temperature increases. In general, it is noted that most of the calculations with both datasets overestimate density.

In *Figure* 8 the %AAD in relation to the pressure, is plotted for some isothermal curves.
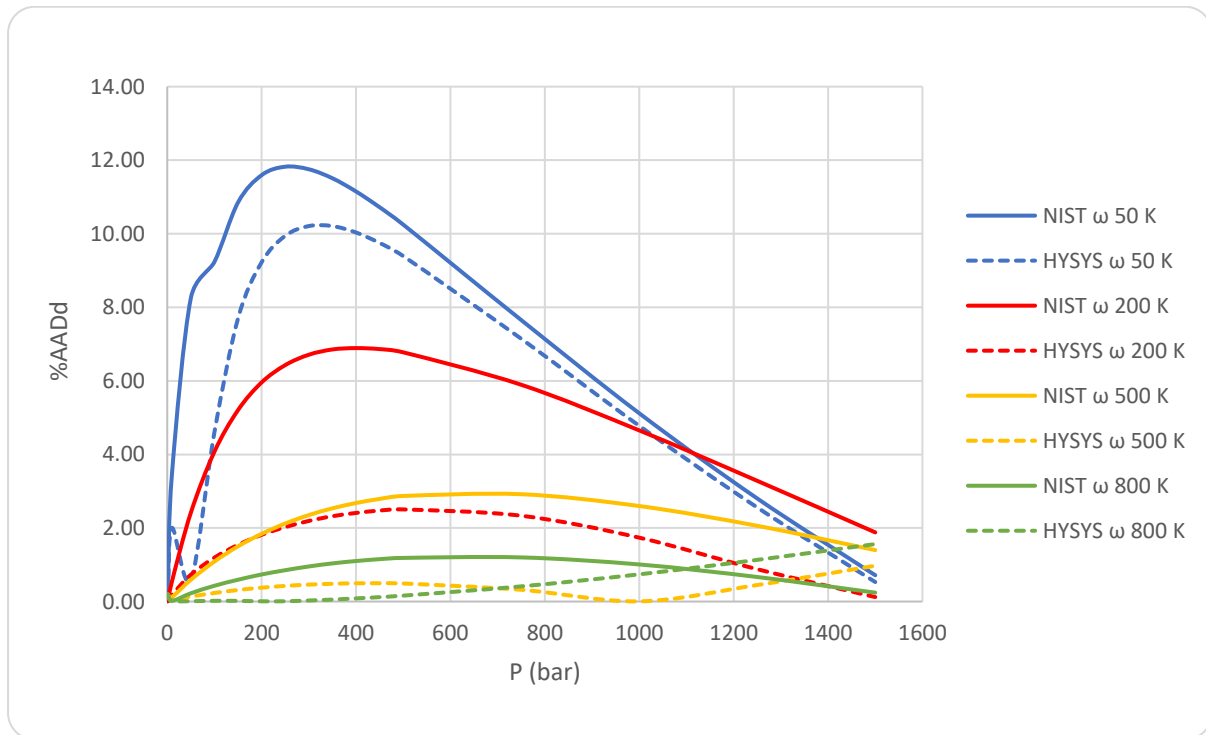
Figure 8: %AAD in supercritical molar density calculations of pure hydrogen in relation to pressure

From *Figure* 8 above it can be concluded that the deviations are not analogous to the pressure, but they are very small in the low and very high pressures.

It is interesting to note that the trend of the deviations in regard to pressure is significantly dependent on temperature as well as on the acentric factor. More specifically, when using the NIST proposed ω, for all isothermal curves, the deviations reach a maximum in a pressure range of 200-600 bar, depending on the temperature. In general, the maximum is shifted to higher pressures as the temperature increases. By comparison, the same trend is observed when using the Aspen HYSYS proposed ω up until 400 K and in the higher temperatures, the deviation reaches a minimum in a interstitial pressure and then as pressure increases the deviation increases as well.

In conclusion, the calculations of the supercritical molar density favor the use of the Aspen HYSYS proposed acentric factor, as the deviations are smaller, except for the very high temperatures above 900 K. In this temperature range however, both sets of calculations have high accuracy. The deviations suggest that a volume translation should be introduced, to further increase the accuracy of the model.

Supercritical Molar Isobaric Heat Capacity

As mentioned in Section 2.9.2 above, by using Peng-Robinson the residual part for the isobaric heat capacity is calculated and this value is added to the ideal contribution. Thus, in order to compare the calculations with the two different acentric factors, the total C_p value must be compared to the total experimental values retrieved from the NIST database.

Ideal-gas C_p calculation

There are many sources providing equations and corresponding parameters for the calculation of the ideal Cp, each with varying results. In this work three different sources were examined, namely NIST, DIPPR and the book "The Properties of Gases and Liquids" by Poling et al. [33]

DIPPR

DIPPR proposes two sets of parameters for the calculation of the C_p ideal value. The first set consists of values that have been determined experimentally and apply to a 50-250 K range. This set has an average error of <3%. The second set's values have been obtained by extrapolation, apply to a 250-1500 K and have an average error of <1%. The parameters proposed are presented in the Appendix 1.

Equations 27 and *28* are proposed for the calculations.

$$C_{p,id} = A + BT + CT^2 + DT^3 + ET^4, \qquad 50 \leq T \leq 250 \ K \qquad\qquad (Eq.\,27)$$

$$C_{p,id} = A + B\left(\frac{\frac{C}{T}}{\sinh\left(\frac{C}{T}\right)}\right)^2 + D\left(\frac{\frac{E}{T}}{\cosh\left(\frac{E}{T}\right)}\right)^2, \quad T \geq 250K \qquad\qquad (Eq.\,28)$$

NIST

NIST proposes three sets of parameters for the calculation of the C_p ideal value. In contrast to DIPPR, it does not have a proposition for temperatures below 298.15 K, thus excluding an important range of special interest for applications. The three ranges proposed are 298-1000 K, 1000-2500 K and 2500-6000 K. There is no estimation for the average error in the calculations. The parameters proposed are presented in Appendix 1.

For the temperature range studied in this work, *Equation 29* is proposed for the calculations.

$$C_{p,id} = A + BT + CT^2 + DT^3 + \frac{E}{T^2} \; , \quad 298 \leq T \leq 1000 \; K \qquad (Eq.\,29)$$

"The properties of gases and liquids"

The book "The Properties of Gases and Liquids" by Poling et al. proposes a set of parameters for the 50-1000 K range, shown in Appendix 1.

Equation 30 is proposed for the calculations.

$$C_{p,id} = (a_0 + a_1 T + a_2 T^2 + a_3 T^3 + a_4 T^4)R \qquad (Eq.\,30)$$

Initially, the ideal C_p values were calculated using the DIPPR and NIST data for the common range 298-1500 K and it was obvious that there was no significant difference in the prediction of the value, as the relative deviation from experimental data was lower than 0.2%. An extrapolation for the NIST data was carried out for the lower temperature range of 50-250 K. It was found that the prediction was poor in low temperatures and acceptable in the 180-250 K with a maximum %AAD of 2.0% for 180 K.

From the above observations, the NIST data for the range 180-1500 K is considered in essence equivalent to DIPPR data so we proceed with the rest of the calculations using the DIPPR database.

The calculations using the data from the book "The Properties of Gases and Liquids" were performed and by comparing them to DIPPR, two temperature ranges of interest were distinguished. For temperatures above 200 K the AAD is small, under 2% and more specifically no more than 0.1% above 250 K. However, there is a significant difference in the trend of the values for the lower temperatures, as well as in the actual values. While with the DIPPR data we calculate high values in low temperatures that decrease with temperature increase and then start to increase again, the calculations from the book follow a strictly increasing trend with increasing temperature. This creates a big difference in the values calculated and results in a contradiction.

The calculations for the ideal C_p value in relation to Temperature are shown below in *Figure* 9.
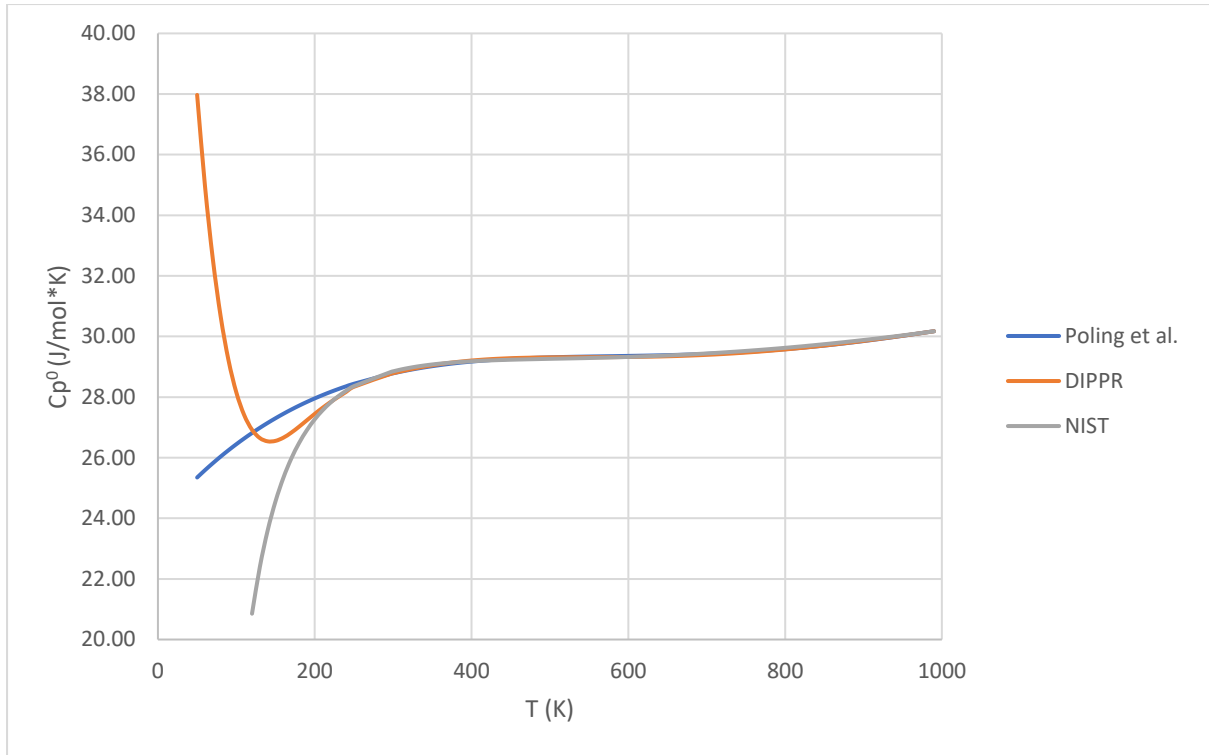
Figure 9: Ideal Cp calculations for pure hydrogen

Deviation of sources in ideal-gas C_p - Hydrogen's behavior

The reason for this contradiction can be linked to hydrogen's quality of having two spin isomers, para-hydrogen and ortho-hydrogen, as mentioned in Section 2.10 previously.

This is the reason the prediction of the isobaric heat capacity of pure hydrogen is difficult to predict in low temperatures. In most available data the equilibrium composition is not stated and due to the slow conversion between the forms, it is uncertain [21]. This makes comparisons and thus calculations more complicated as it is difficult to define the reference states.

To demonstrate the differences that occur in the ideal isobaric heat capacities, *Figure 10* is presented below. It is obvious in this graph that parahydrogen exhibits a much higher ideal-gas C_p value in temperatures below 400 K.
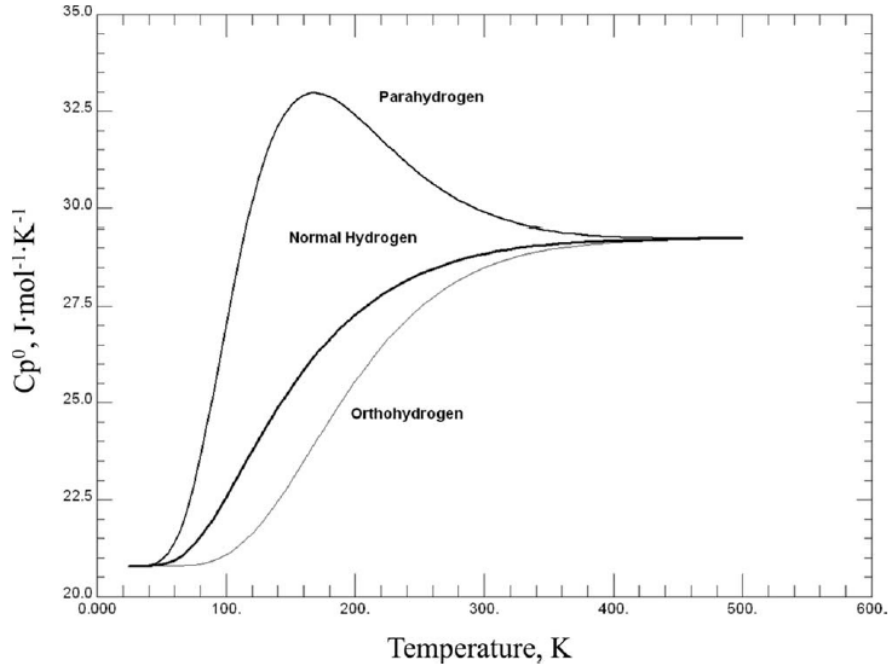
Figure 10: Ideal-gas isobaric heat capacities for para-hydrogen, ortho-hydrogen and normal hydrogen [22]

In higher temperatures where hydrogen is normal, the deviation between the two sources for the value of the ideal C_p is very small. More specifically, for temperatures above 250 K the AAD is less than 0.5% and thus they will not be examined separately for this temperature range.

Total isobaric heat capacity calculations

The calculations for the total C_p value of pure hydrogen were performed in 4 cases, as shown in *Table 12* below.

Table 12: Calculations for total C_p for pure hydrogen

Case	C_p ideal	C_p residual
1	DIPPR	NIST ω
2	Poling et al. [33]	NIST ω
3	DIPPR	HYSYS ω
4	Poling et al. [33]	HYSYS ω

As predicted, in all cases the model has a better predicting efficiency in higher temperatures. This is evident in *Figure 11* below, where it is clear that at temperatures higher than 200 K the %AAD is very low. It can also be seen clearly that Cases 1 and 3 that use the DIPPR ideal part exhibit very high values of %AAD and therefore the data from Poling et al. (Cases 2 and 4) are deemed more trustworthy.
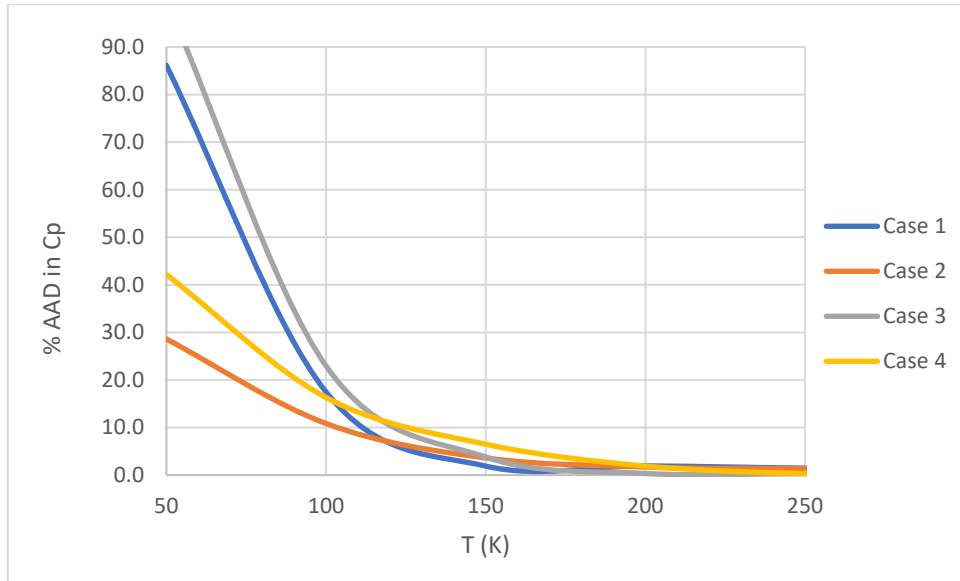
Figure 11: %AAD in C_p for pure hydrogen for Cases 1-4 in 50-250 K

In a more detailed analysis at the lower temperatures, as shown in the graph above in *Figure 11*, it can be seen that at the lower temperatures (below 250 K) the prediction is better when using the NIST suggested acentric factor.

In almost all calculations in the range of 50-200 K with both acentric factors, the total isobaric heat capacity value is overestimated. The only exceptions occur when using the NIST ω at the 200 K isothermal in pressure above 450 K and the calculation at 50 K and 50 bar. Overall, overestimation is greater when using the HYSYS based omega.

It is noted that the prediction gets significantly better when temperature rises. No clear trend of the effect of the pressure can be concluded in this temperature range.

At temperatures higher than 250 K, the variation between the two models is negligible and both sets of calculations are considered highly accurate.

Table 13 below summarizes the results of the case study in regards to the deviation from the experimental values of the total isobaric heat capacity.

Table 13: Average deviations in the calculations of C_p

| T (K) | Average %AAD | | | |
	Case 1	Case 2	Case 3	Case 4
50	86.2	28.6	99.8	42.2
100	17.5	10.8	23.0	16.3
150	1.9	3.6	3.8	6.5
200	1.9	1.7	0.3	1.9
250	1.5	1.3	0.3	0.3
300	1.1	1.1	0.4	0.4
400	0.5	0.5	0.1	0.1
500	0.4	0.4	0.3	0.3
600	0.2	0.3	0.2	0.3
700	0.1	0.2	0.1	0.1

800	0.1	0.2	0.2	0.2
900	0.2	0.2	0.2	0.2
1000	0.3	0.4	0.2	0.2
Overall	**7.6**	**3.3**	**8.8**	**4.6**

It is clear that there is a difficulty in predicting pure hydrogen's isobaric heat capacities in lower temperatures, as it was explained above, due to hydrogen's molecules' nature.

From the comparison of the results with the NIST and the HYSYS acentric factors it can be concluded that the NIST one is more suitable for lower temperatures whereas the HYSYS one is better for higher temperatures. In the higher temperatures however, above 250 K, both predictions are considered sufficient.

Figures 12 and *13* below illustrate the comparison between the calculations and the experimental data for various isothermal curves in the examined temperature range.
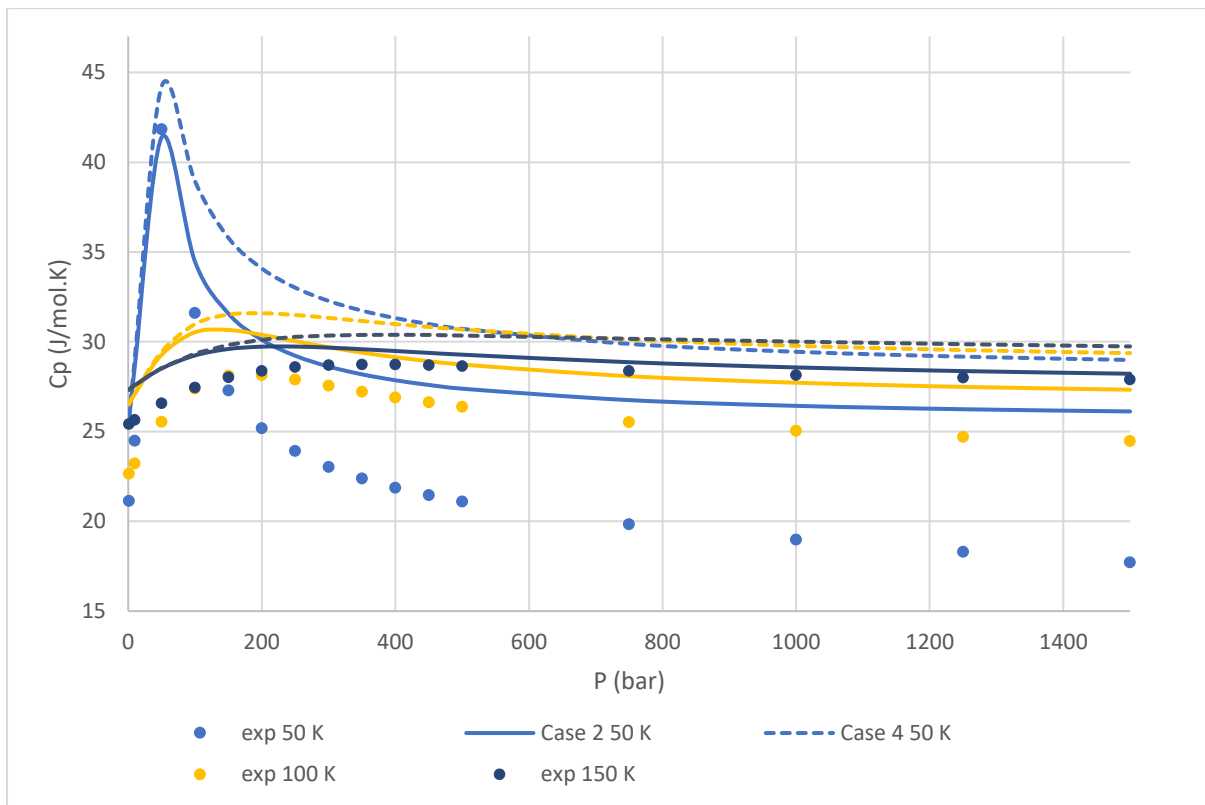
Figure 12: C_p calculations for pure hydrogen in temperature range 50-150 K
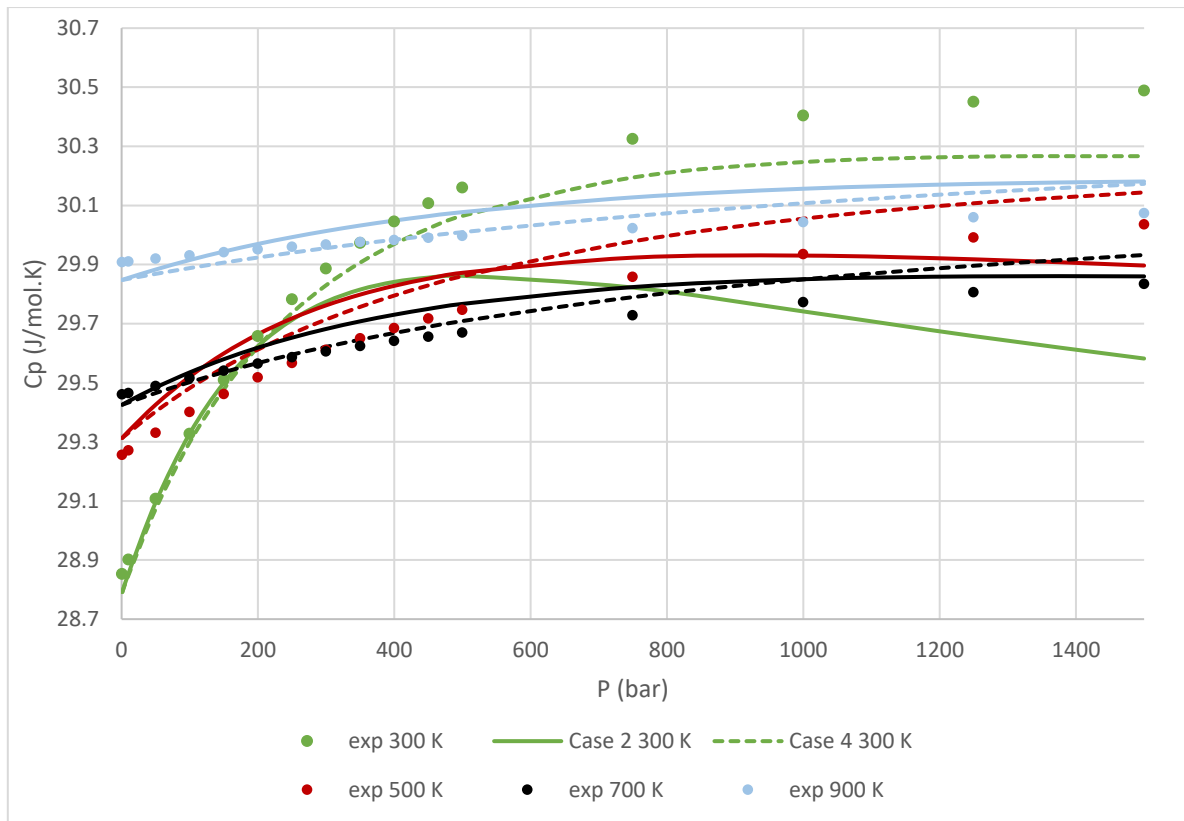
Figure 13: C_p calculations for pure hydrogen in temperature range 300-900 K

3.2 Mathias – Copeman alpha function

From the analysis conducted for pure hydrogen using Soave's alpha function and comparing the two acentric factors, it can be concluded that, especially at lower temperatures and at saturation, the use of the NIST proposed ω is optimal, while the Aspen HYSYS proposed ω yields better results for some properties, such as supercritical density. Due to this discrepancy regarding the optimal acentric factor in subcritical and supercritical calculations, another alpha function is examined.

Since the Mathias-Copeman expression for the alpha function utilizes three parameters, c_1, c_2, c_3, compared to Soave's expression that only utilizes one parameter (acentric factor), it is deemed as more appropriate for fitting those parameters to experimental data in order to increase the model's accuracy. Although the original Mathias-Copeman function as presented in *Table 4* is a piecewise equation, in this work only the first segment will be used for the entire temperature range, because it contains three parameters and it is therefore more suitable for the regression.

The chosen properties that are fitted in order to find the optimal c_1, c_2, c_3 values are the saturated pressure (Ps) for the subcritical region and the total isobaric heat capacity C_p for the supercritical region. *Table 14* below summarizes the fitting criteria.

Table 14: Fitting of c_1, c_2, c_3 criteria for optimization of Mathias Copeman alpha function

	Subcritical region	**Supercritical Region**
Property	Saturated pressure P^s	Total isobaric heat capacity C_p
Temperature Range (K)	14-32	50-1000
Pressure Range (bar)	-	1-1500
Number of experimental points	19	144

More experimental points at the lower temperatures, below 300 K were taken into consideration for the fitting of the isobaric heat capacity because the prediction at the elevated temperatures was accurate with Soave's alpha function. That is because at high temperatures the isobaric heat capacity the ideal contribution is much more significant. It is important however to check the model's ability to yield accurate results in the high temperatures as well and that is why some experimental data at higher temperatures was included.

The average deviation in the prediction of the supercritical molar isobaric heat capacity is calculated from all experimental points mentioned in Section 3.1.2 above.

The regression results as well as the results of the calculations are presented in *Table 15*.

Table 15: Results of Mathias-Copeman parameters fitting of P^s and supercritical C_p

Regression	Regressed property	c_1	c_2	c_3	%AADP^s	%AADC$_p$
1	C_p	-0.190601	-0.155184	-0.021580	69.92	2.23
2	P^s	0.079785	-0.18264	-0.17527	0.68	>100
3	70% P^s - 30% Cp	0.057506	-0.156502	-0.015787	1.71	4.69
4	80% P^s - 30% Cp	0.060930	-0.166264	-0.019331	1.55	4.79

The results of the single-property regressions make it clear that it is easier to predict the saturated pressure in a much higher accuracy than the isobaric heat capacity. This led to performing regression in which the AAD in the objective function was weighted for each property. It is obvious however, that by performing a regression on a single property leads to inaccurate calculations in the other property as the deviations from the experimental data are very high and therefore the obtained parameters cannot be used for calculations in both the subcritical and the supercritical temperature range.

While processing the results of the fittings it was concluded that the saturated pressure is much more sensitive to the alteration of the c_1, c_2, c_3 parameters than the isobaric heat capacity, as slight changes led to very different results in the saturated pressure value and the average %AAD was ranging significantly, whereas the isobaric heat c capacity calculations were less sensitive. That is why, the weights chosen in the objective function of the regression were larger for the vapor pressure. It can be observed in *Table* 15 in regressions 3 and 4, that by increasing the weight in vapor pressure, from 70% to 30%, the accuracy increases in the vapor pressure prediction but decreases in the isobaric heat capacity, and that is why the weights are adjusted according to the property of interest.

The results of the fittings have a significant improvement in the prediction of the saturated pressure, as the deviation is brought down from 4.0% to 1.6-1.7%, when comparing the results from Soave's alpha function.

By plotting however, the alpha function using the parameters obtained from the simultaneous P^s and C_p regression, it can be observed that it does not satisfy the criteria described in Section 2.3.1 above. The function reaches a minimum at a reduced temperature of around 14 which is much lower than the temperatures of interest. In addition, the function is not monotonically decreasing. Therefore, new fittings of the parameters were carried out, implementing a penalty if the consistency criteria were not met, for a temperature range up to 1000 K. Depending on the criterion not met, a value was added to the objective function employed in the regression.
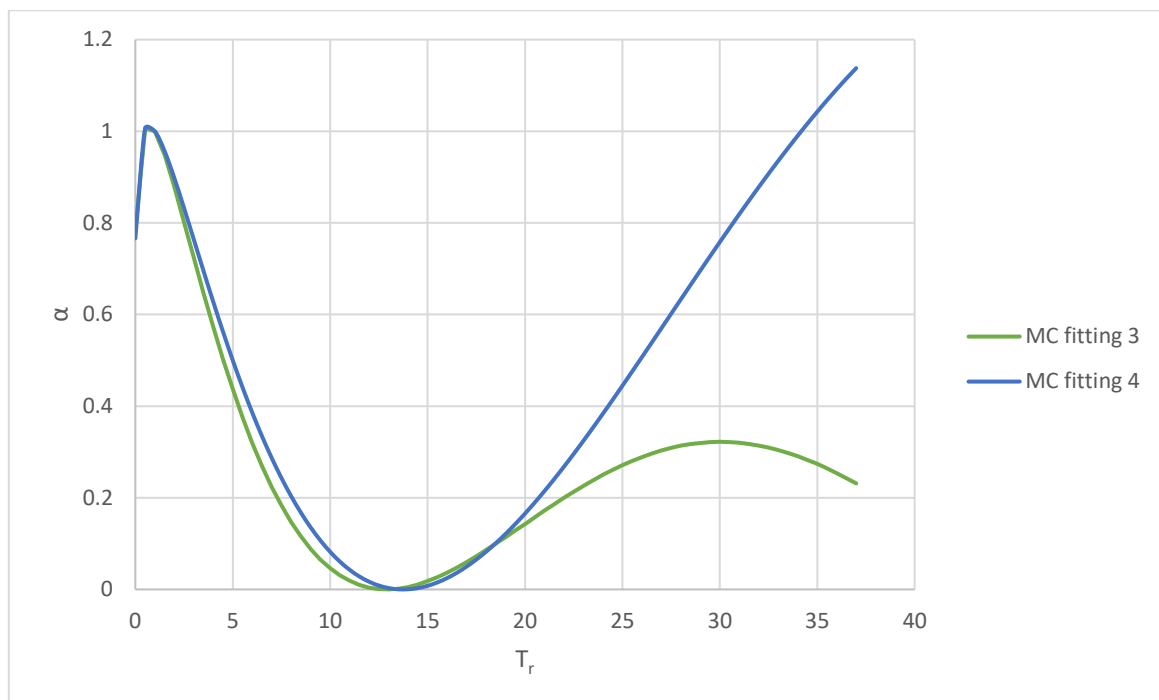
Figure 14: MC alpha function with parameters obtained from fitting saturated pressure and supercritical isobaric heat capacity

In the attempt to constrain the alpha function according to the criteria in Section 2.3.1 above, the following results from the fittings shown in *Table 16* below were obtained.

Table 16: Results of Mathias-Copeman parameters constrained fitting of P^s and supercritical C_p

Regression	c_1	c_2	c_3	%AADP^s	%AADC$_p$
5	0.027326	-0.030195	0.001348	3.47	3.63
6	0.026219	-0.034078	0.001182	3.39	3.64

The corresponding plots of the alpha functions using the parameters shown in *Table 16* are demonstrated in *Figure 15* below.
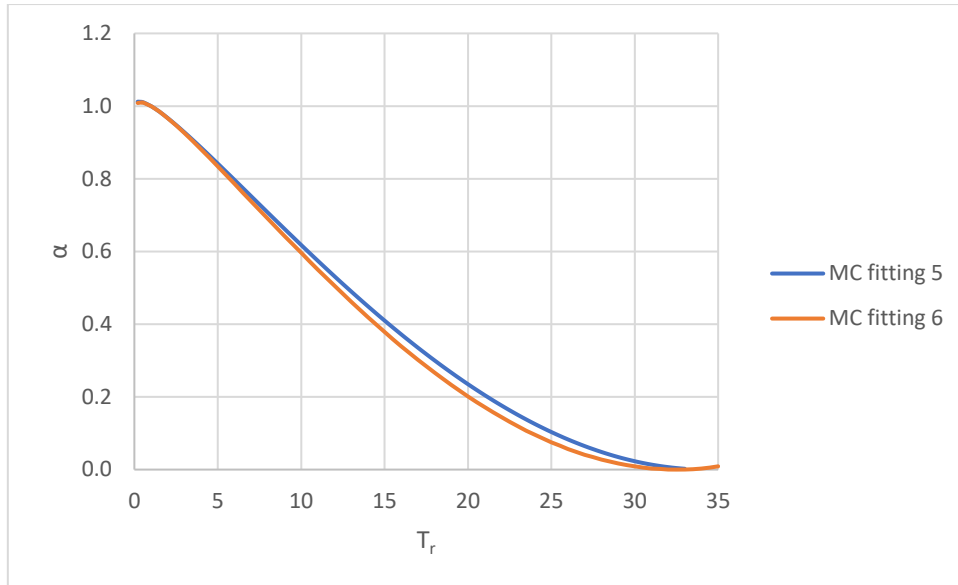
Figure 15: MC alpha function with parameters obtained from fitting saturated pressure and supercritical isobaric heat capacity implementing consistency criteria

By a direct comparison between *Figure 14* and *Figure 15* it is obvious that the alpha functions obtained when implementing consistency criteria lead to monotonically decreasing functions. It can be noted however, that they fail to fulfil the convexity criterion at low values of reduced temperature, around 0.3-0.5, although they provide a little better results in accuracy, around 0.5% less. This becomes clearer in *Figure 16* below.
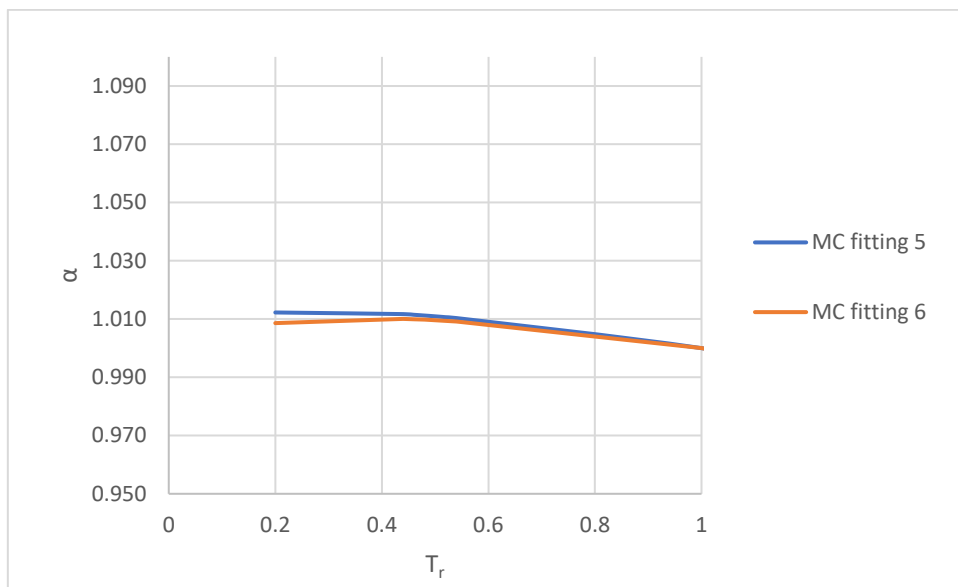
Figure 16: Incosistency of alpha function of "MC fitting 3" and "MC fitting 4" in very low reduced temperatures

The small improvement in the results obtained from fitting the Mathias-Copeman alpha function parameters does not justify its complexity. For this reason, regression of only parameter c_1, was conducted. The results obtained are presented in *Table 17* below where the Soave calculation results are also showcased for comparison.

Table 17: Results of c_1 Mathias Copeman parameter constrained fitting of P^s and supercritical C_p

Regression	c_1	c_2	c_3	%AADP^s	%AADC$_p$
NIST ω	m= 0.02389	0	0	3.96	3.49
Fitting 7	0.01025	0	0	3.91	3.39

From the one-parameter-fitting results, no significant improvement from the results of using the NIST proposed acentric factor is achieved.

3.3 Twu alpha function

As it was concluded from the previous section, improved prediction of the saturated pressure could be achieved when the alpha function does not satisfy the consistency criteria presented in Section 2.3.1. Therefore, another alpha function is examined, and specifically Twu's alpha function as it is an exponential function and by default satisfies the criteria about the first and the second derivative. In the work of Twu [11] there are no proposed values for Peng-Robinson for the parameters L, M, N for hydrogen. Calculations were performed using the Aspen HYSYS proposed parameters as well as the ones proposed in the work by Aasen et al. [24]. Regression of the L, M, N parameters was also carried out with the implementation of consistency criteria, the optimal results of which are presented in *Table 18* below together with the results of the calculations.

Table 18: Twu alpha function parameters

Source	L	M	N	%AADP^s	%AADC$_p$
Aspen HYSYS	0.4409	1.4878	0.5200	0.81	4.47
Aasen et al. [24]	1.5147	-3.7959	-0.1377	2.73	5.20
This work (0.9 P^s - 0.1 C_p)	0.5244	1.7380	0.0538	3.96	3.38

The plot of the alpha functions using the parameters shown in *Table 18* above is illustrated in *Figure 17*.
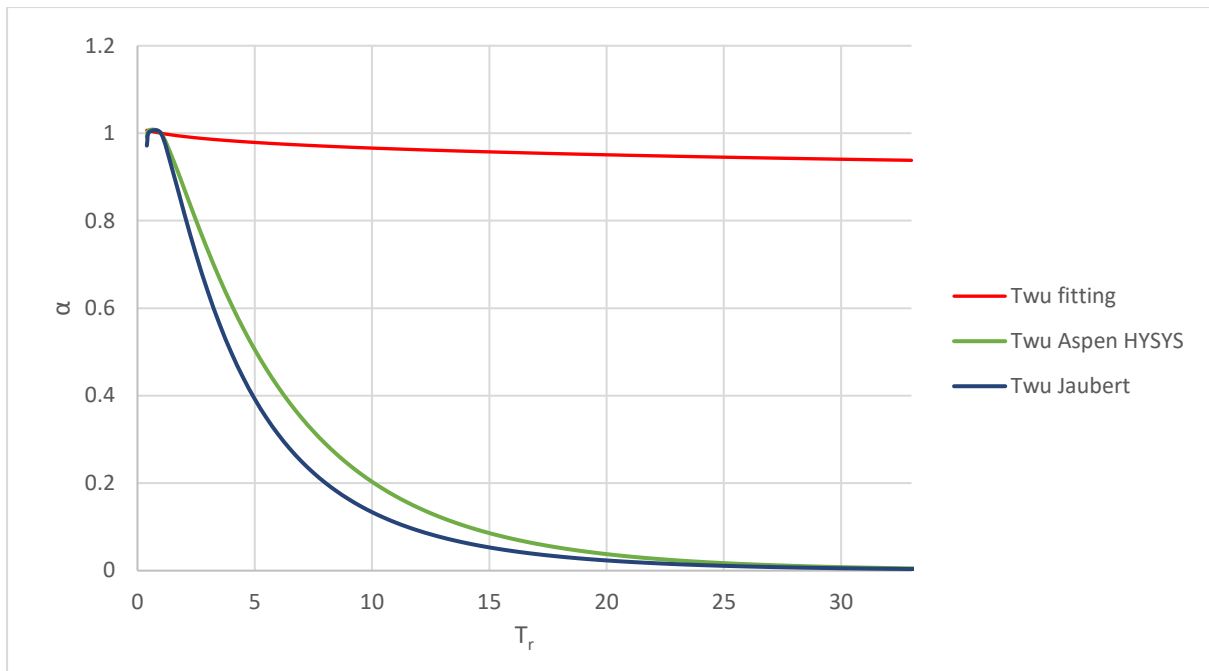
Figure 17: Twu alpha function plots

From *Figure 17* above it is obvious that the criterion regarding the monotonically decreasing alpha function is not met when using the parameters proposed by Aspen HYSYS and in the work of Jaubert et al. However, the accuracy of the model when using Twu's alpha function and the fitted parameters in predicting the saturated pressure is equivalent to using Soave's alpha function with the NIST proposed acentric factor. These results do not justify the complexity of Twu's alpha function.

A comparative plot of the different types of alpha functions examined is presented in *Figure 18* below.

48
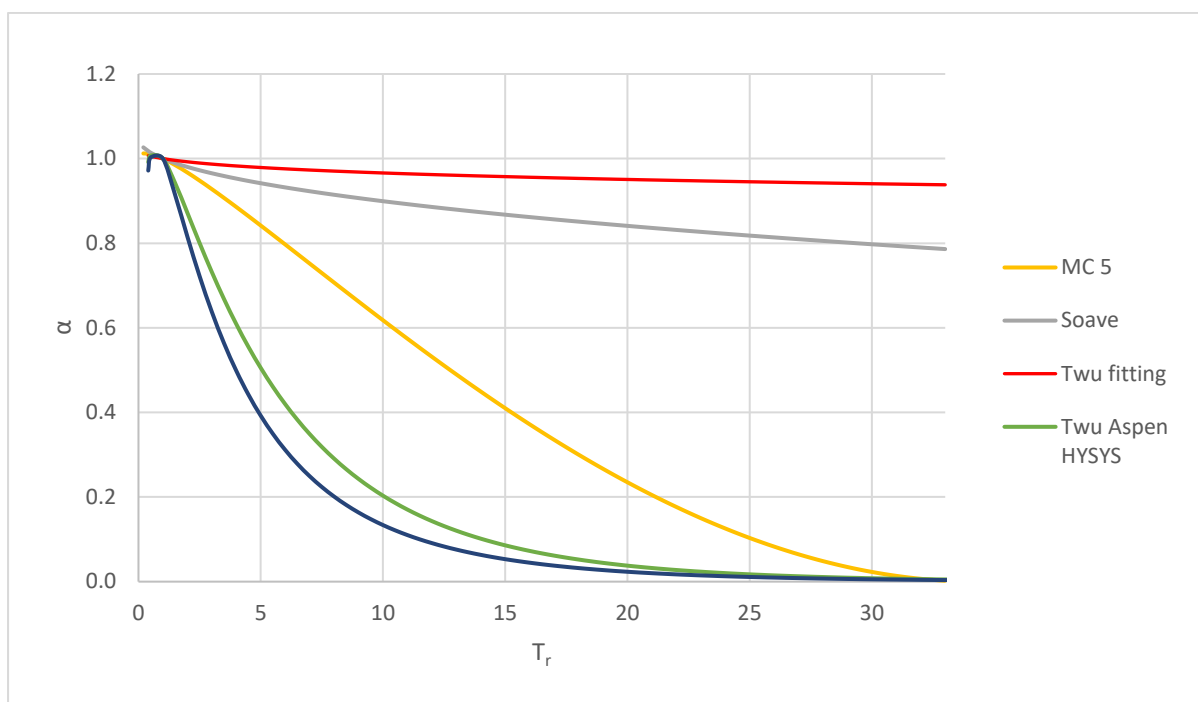
Figure 18: Different types of alpha functions examined in this work

In conclusion, to achieve accurate results, the consistency of the alpha function has to be compromised. Equivalent results to Soave's alpha function can be obtained when the consistency criteria are satisfied, but the higher complexity of the other alpha functions favors the use of Soave's alpha function using the acentric factor proposed by NIST.

3.4 Volume Translation

Having concluded in the use of Soave's alpha function with the NIST proposed ω and as mentioned above, to improve the prediction of the saturated liquid volume and the supercritical volume, a translation must be introduced. To make the model as simple as possible, a temperature-and-pressure-independent volume translation value was obtained for each domain, subcritical and supercritical. These values were obtained by minimizing the average deviation of the calculations made in Sections 3.1.1 and 3.1.2 above and solving the objective function for the optimal volume translation value. The introduction of the saturated liquid volume translation equal to -0.00456 L/mol reduces the average deviation from 15.9% to 3.8%. The use of the supercritical volume translation equal to -0.00228 L/mol reduces the average deviation from 2.9% to 1.6% *Table 19* below summarizes the introduction of volume translation.

Table 19: Volume translation in pure hydrogen

	Volume translation (L/mol)	%AADv untranslated	%AADv translated
Subcritical*	-0.00456	15.9	3.8
Supercritical	-0.00228	2.9	1.6

*The volume translation in the subcritical region regards the saturated liquid volume.

The comparison between the calculations without the implementation of volume translation of the EoS and with it are presented in *Figure 19* and *20* for the saturated liquid volume and the supercritical density, respectively.
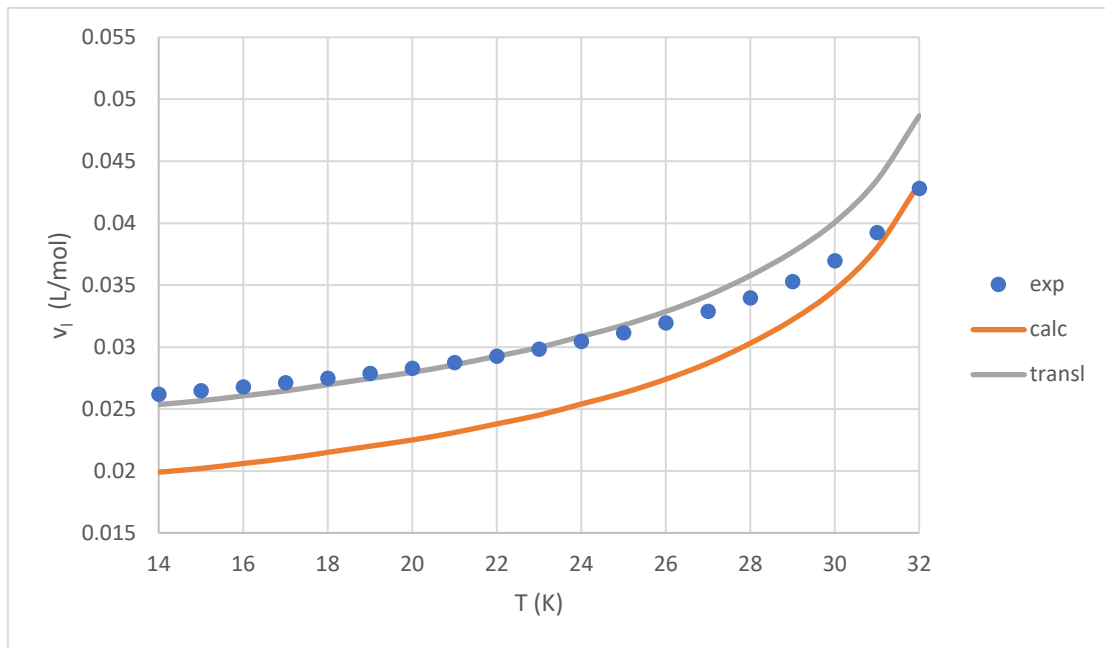
Figure 19: Improvement of the prediction of the saturated liquid volume by introducing volume translation

In *Figure 19* it can be observed that the volume translation is not necessary at temperatures higher than 0.8 times the reduced temperature.
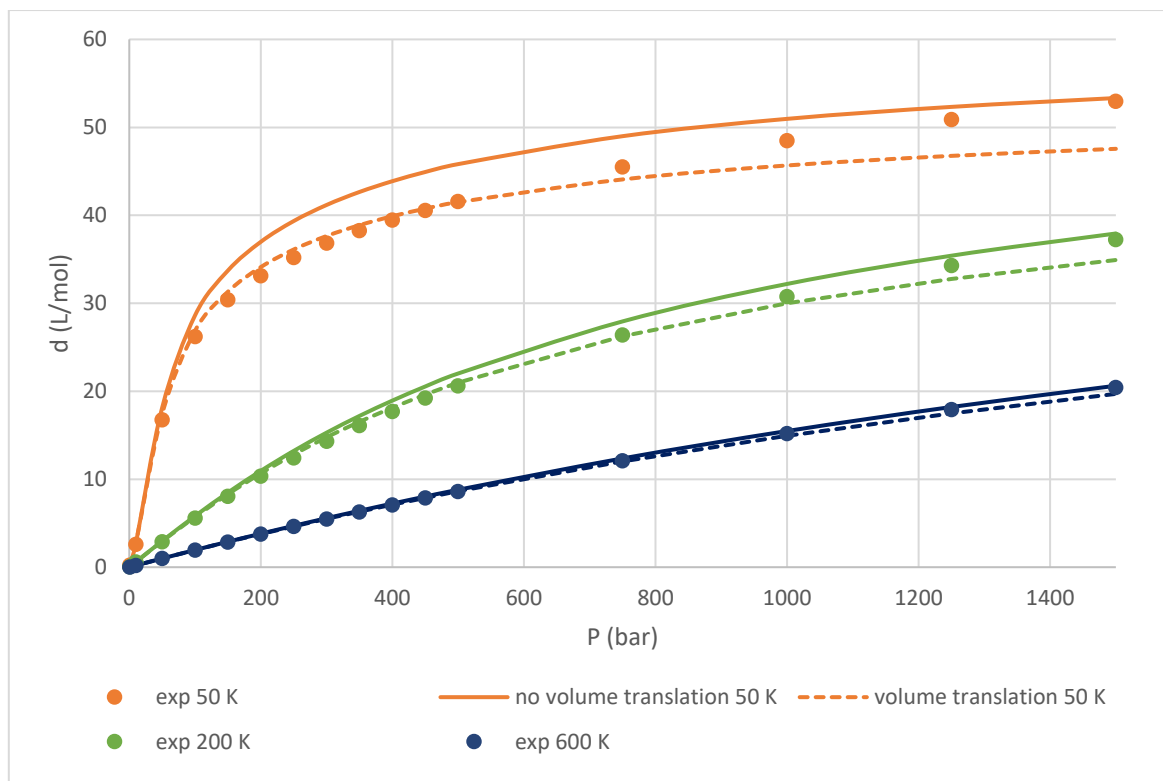
Figure 20: Improvement of the prediction of the supercritical density by introducing volume translation

As expected, the effect in the improvement of the supercritical density prediction by introducing volume translation is more pronounced at the lower temperatures. It can also be noted from *Figure 20* that the volume translation is not necessary at high pressures above 1000 bar.

3.5 Supercritical speed of sound and Joule-Thomson coefficient calculations

The rest of the properties of interest for pure hydrogen, namely the speed of sound and the Joule Thomson coefficient were calculated with Peng-Robinson with Soave's alpha function and the NIST proposed ω.

3.5.1 Speed of sound

In *Table 20* below, the average deviation for the calculations of the supercritical speed of sound for each isothermal curve is presented with and without volume translation.

Table 20: Average %AAD in the prediction of speed of sound of pure hydrogen

T (K)	%AADw PR untranslated	%AADw PR translated
50	17.3	22.8
100	9.2	10.4
150	5.7	6.8
200	3.9	5.0
250	2.9	4.0
300	2.3	3.3
400	1.6	2.5
500	1.2	2.1
600	0.9	2.0
700	0.7	1.9
800	0.6	1.8
900	0.6	1.8
1000	0.6	1.7
overall	**3.7**	**5.1**

From the results in *Table 20* above it is apparent that similarly to the isobaric heat capacity, the accurate prediction of the supercritical speed of sound is more difficult at low temperatures. The prediction improves significantly as the temperature increases in the temperature range of 50-250 K and above 600 K the prediction is highly accurate and the deviations are relatively low, regardless of temperature.

It is interesting to note that using a volume translation, which is incorporated in the calculation of the speed of sound, leads to less accurate results overall for each isothermal curve. In a more detailed analysis of this observation, *Figures 21 – 22* are presented below. The volume translation leads to an improvement in the prediction of the speed of sound at the lower pressure range of 1-400 bar approximately at temperatures lower than 800 K. In general, in each isothermal curve, the model underestimates the value of the speed of sound is overestimated at high pressures above 750 bar.

From Figures *21* and *22* it can be concluded that the prediction of speed of sound is inaccurate at high pressures and low temperatures.
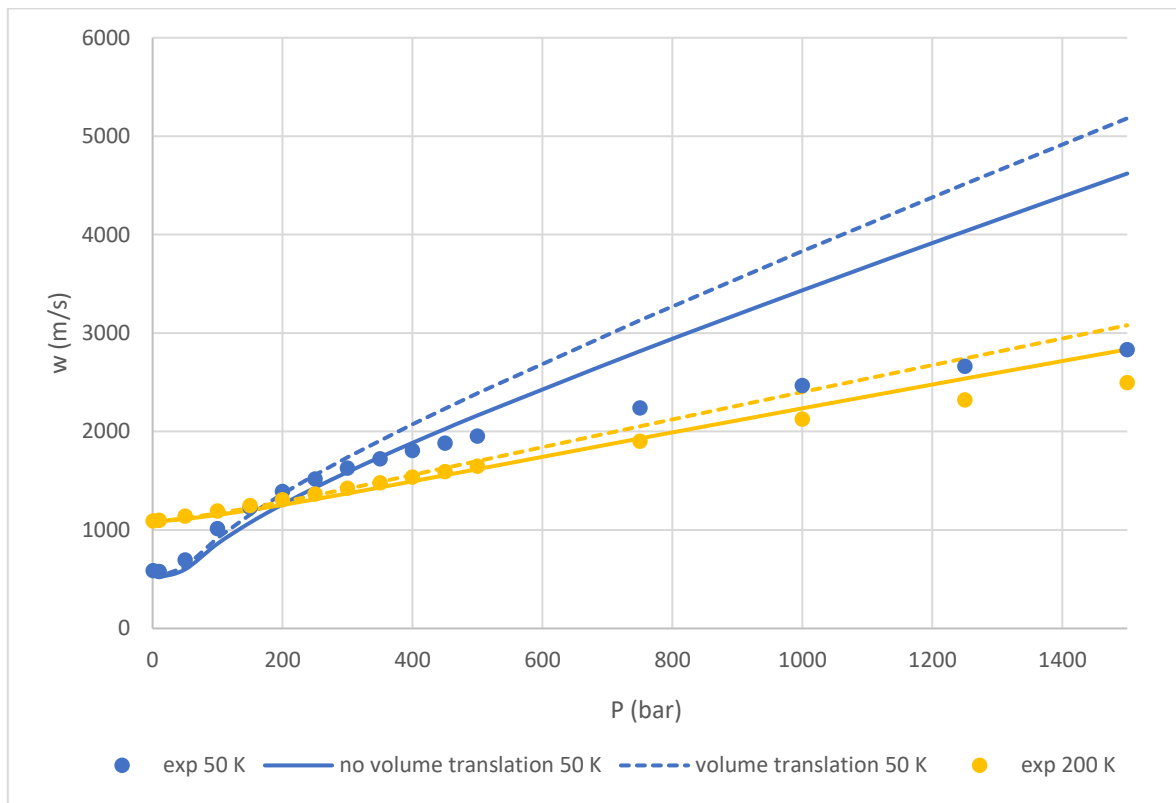
Figure 21: Speed of sound calculations for pure hydrogen in 50, 200 K
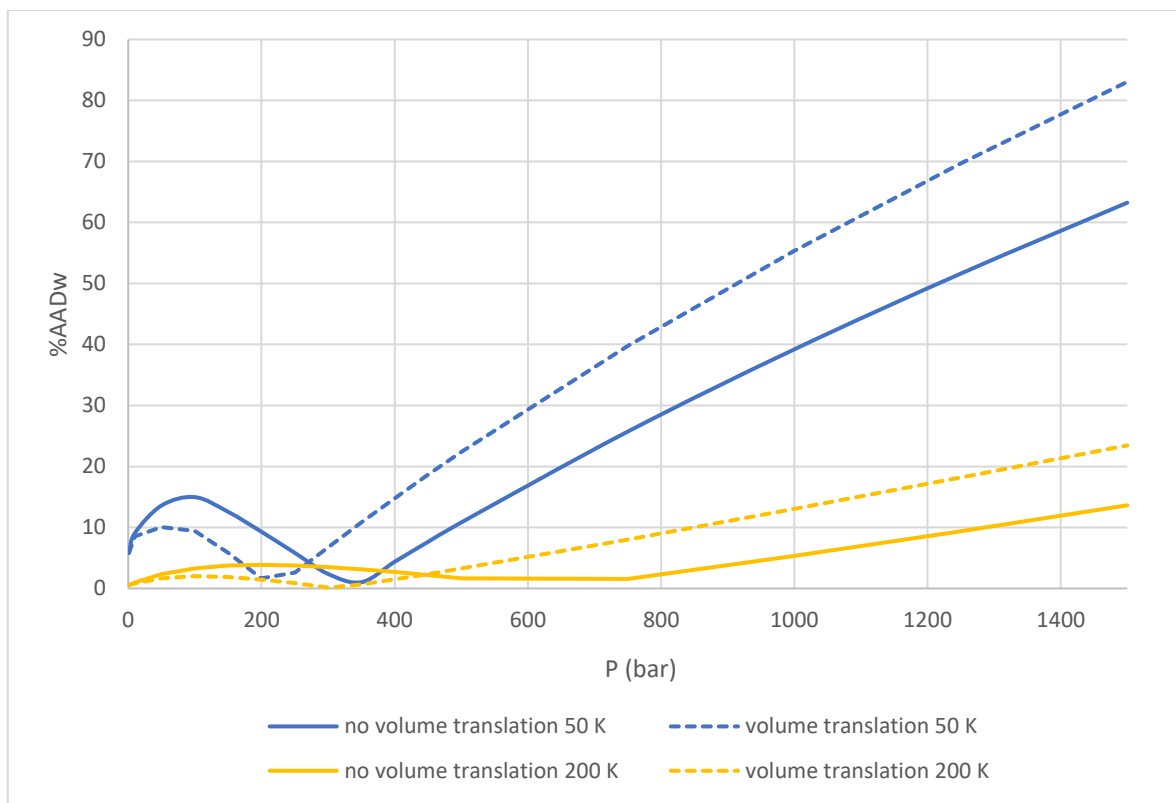
Figure 22: Speed of sound calculation deviations in 50, 200 K

More figures like *Figures* 21 and 22 are presented in the Appendix 2.

3.5.2 Joule-Thomson coefficient

In *Table 21* below, the average absolute deviation for the calculations of the supercritical Joule-Thomson coefficient in each isothermal curve examined is presented with and without volume translation.

Table 21: Average deviation in the prediction of Joule-Thomson coefficient of pure hydrogen

T(K)	AADμ_{JT} PR untranslated	AADμ_{JT} PR translated
50	0.026	0.021
100	0.012	0.006
150	0.016	0.011
200	0.017	0.013
250	0.018	0.013
300	0.019	0.013
400	0.019	0.013
500	0.019	0.013
600	0.019	0.012
700	0.018	0.011
800	0.017	0.010
900	0.017	0.009
1000	0.016	0.008
	0.018	**0.012**

Unlike the prediction of the speed of sound, the prediction of the Joule-Thomson coefficient is improved when volume translation is implemented in the calculations. The prediction is also more accurate as both the temperature and the pressure increase. These observations are illustrated in *Figure 23* below, where the calculated values of the coefficient are plotted in comparison to the experimental data.
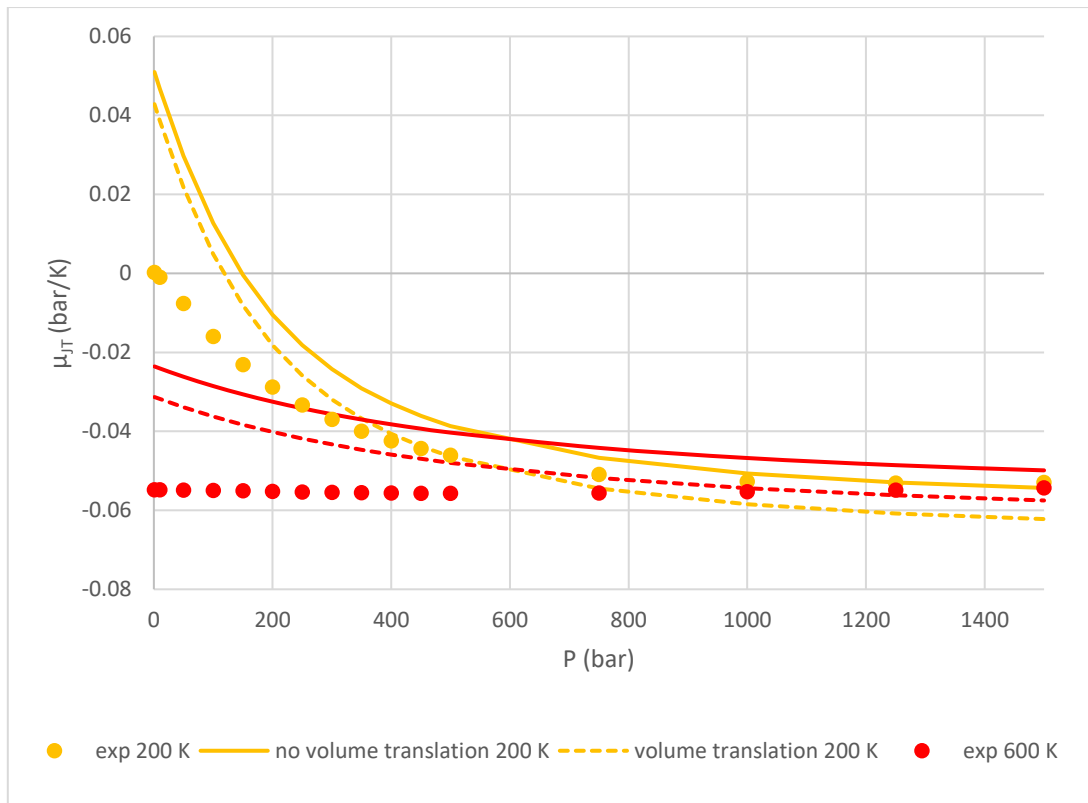
Figure 23: Joule-Thomson coefficient calculations for pure hydrogen

Furthermore, the absolute deviation of the calculations in the same isothermal curves of *Figure 24* is plotted in relation to pressure.
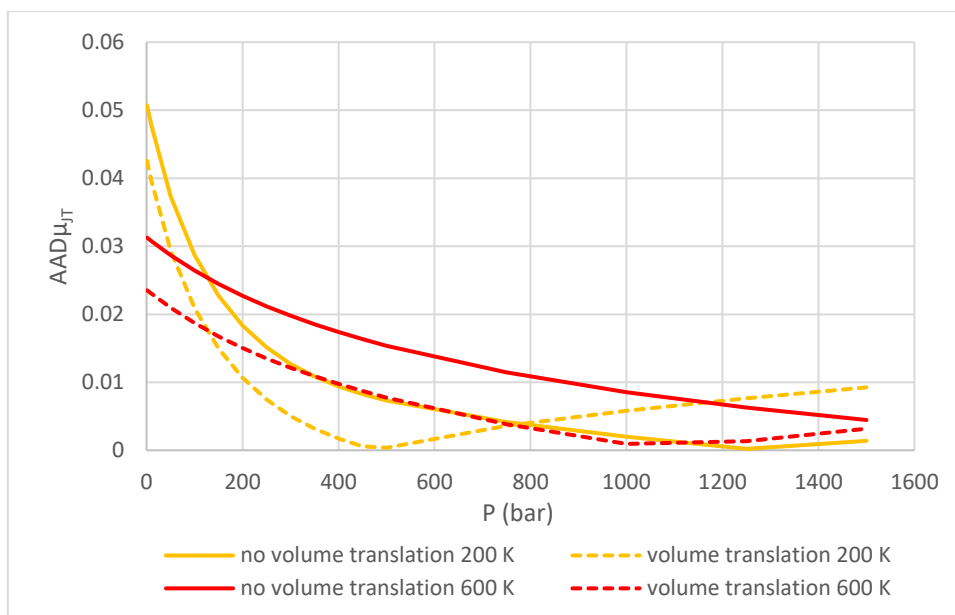
Figure 24: Absolute deviation in the calculations of Joule-Thomson coefficient in pure hydrogen

3.6 SAFT-VRQ-Mie

Due to hydrogen's quantum nature, as described earlier in Section 2.10, it is important to incorporate quantum corrections in the model used to predict hydrogen's properties. That is why SAFT-VRQ-Mie was chosen to make some comparisons.

3.6.1 Subcritical Region

Calculations for the saturated pressure, saturated vapor density and saturated liquid density were performed. The results in terms of deviation from the experimental data are presented in *Table 22* below.

Table 22: %AAD in saturated pressure, saturated vapor density and saturated liquid density of calculations using SAFT-VRQ-Mie model

Property	%AAD
P^s	6.4
d_v	6.2
d_l	1.1

From the results in *Table 22* above it can be observed that the SAFT-VRQ-Mie model is very accurate in the prediction of the saturated liquid density and it should also be noted that this high accuracy of 1.1 %AAD is achieved without a translation volume.

Below the plots of the properties calculated in comparison to experimental data are presented in *Figures 25-27*.
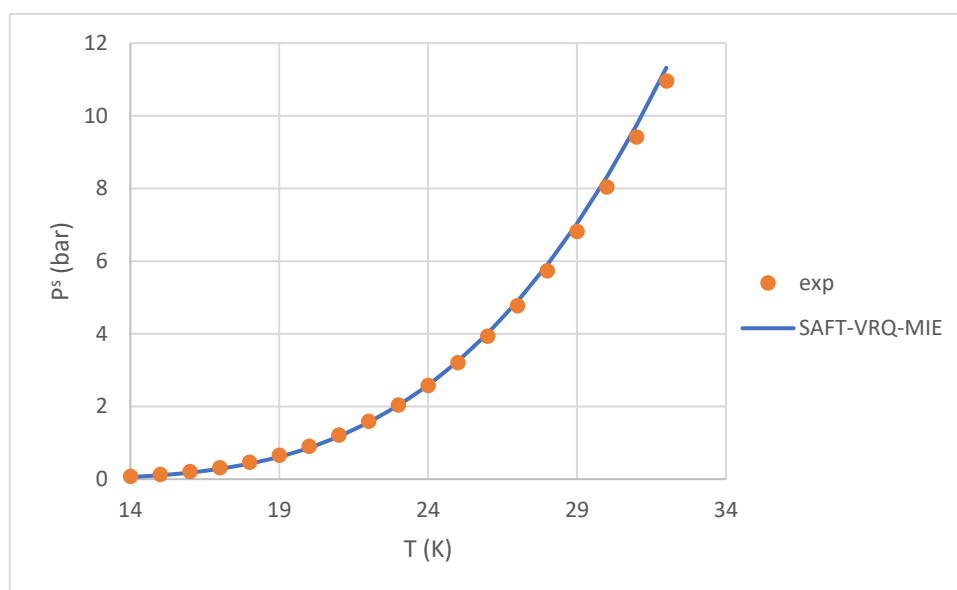
Figure 25: SAFT-VRQ-Mie prediction of saturated pressure of pure hydrogen

The highest relative deviations from the experimental data occur at the lowest temperatures of 14-17 K where the %AAD is greater than 10%. However, the actual value of the saturated pressure at these temperatures is very small and so the absolute deviation is low, in the 10^{-2} order of magnitude. The relative deviation reaches a minimum around 24 K as it can be observed from *Figure 25*, and afterward the deviation increases as the temperature increases.
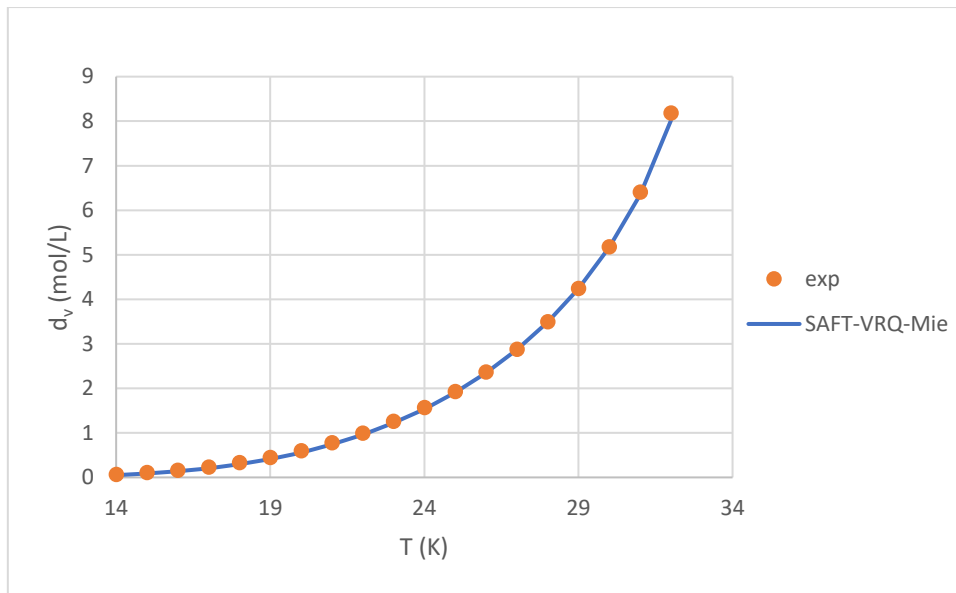
Figure 26: SAFT-VRQ-Mie prediction of saturated vapor density of pure hydrogen

Similarly to the prediction of the saturated pressure, the largest relative deviations in the calculation of the saturated vapor density occur in the lowest temperature range of 14-18 K where the relative deviation is higher than 10%. The actual experimental values however are low and thus the absolute deviation is also low in the 10^{-2} order of magnitude. The relative deviation reaches a minimum around 29 K.
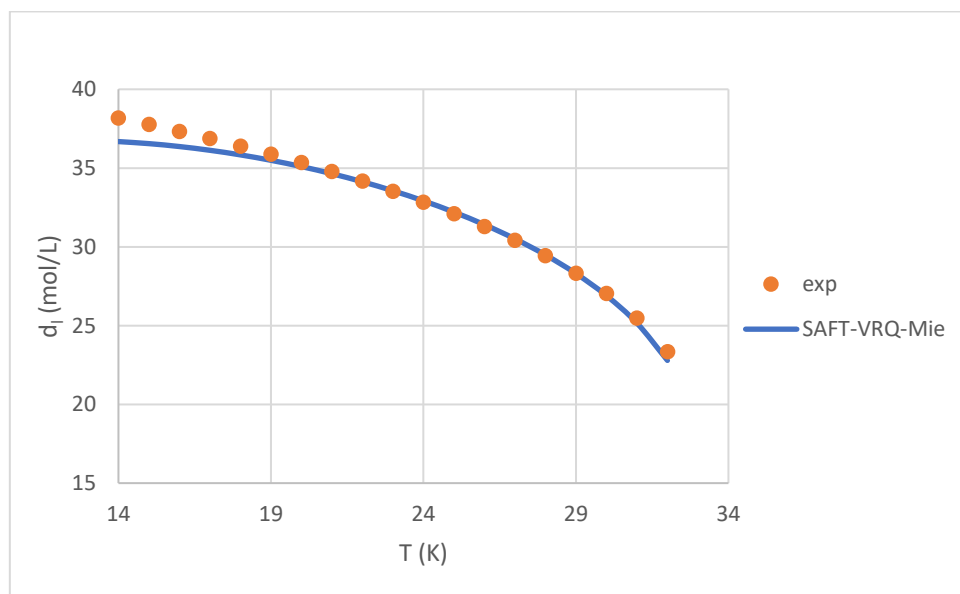
Figure 27: SAFT-VRQ-Mie prediction of saturated liquid density of pure hydrogen

Similarly to the other properties, the largest deviation from the experimental data in the calculation of the saturated liquid density occurs in the lowest temperatures, as it can be clearly shown in *Figure 27* above. The relative deviation is minimized around 23 K.

3.6.2 Supercritical Region

The properties calculated in the supercritical domain for pure hydrogen with Peng-Robinson were also calculated with SAFT-VRQ-Mie. *Table 23* below summarizes the relative deviations (with the exception of the Joule-Thomson coefficient which is expressed in terms of absolute deviation) occurred for each isothermal curve in the properties examined.

Table 23: Volume, isobaric heat capacity, speed of sound and Joule-Thomson coefficient relative deviations calculated with SAFT-VRQ-Mie for pure hydrogen

T (K)	%AADv	%AADC$_p$	%AADw	AADμ$_{JT}$
50	0.8	28.6	6.8	0.030
100	0.2	19.5	5.6	0.010
150	0.6	9.5	3.0	0.002
200	0.7	3.8	1.5	0.001
250	0.7	1.1	0.9	0.001
300	0.7	0.3	0.6	0.002
400	0.7	0.4	0.5	0.002
500	0.6	0.2	0.4	0.003
600	0.5	0.1	0.4	0.003
700	0.5	0.1	0.3	0.003
800	0.4	0.2	0.3	0.003
900	0.4	0.2	0.2	0.003
1000	0.3	0.2	0.2	0.003
Overall	**0.5**	**4.9**	**1.6**	**0.005**

It is important to note that the ideal-gas C_p value incorporated in the calculations of the total isobaric heat capacity is different than the one used in the calculations with Peng-Robinson.

The properties studied were plotted in selected isothermal curves in comparison to experimental data below in *Figures 28-31*.
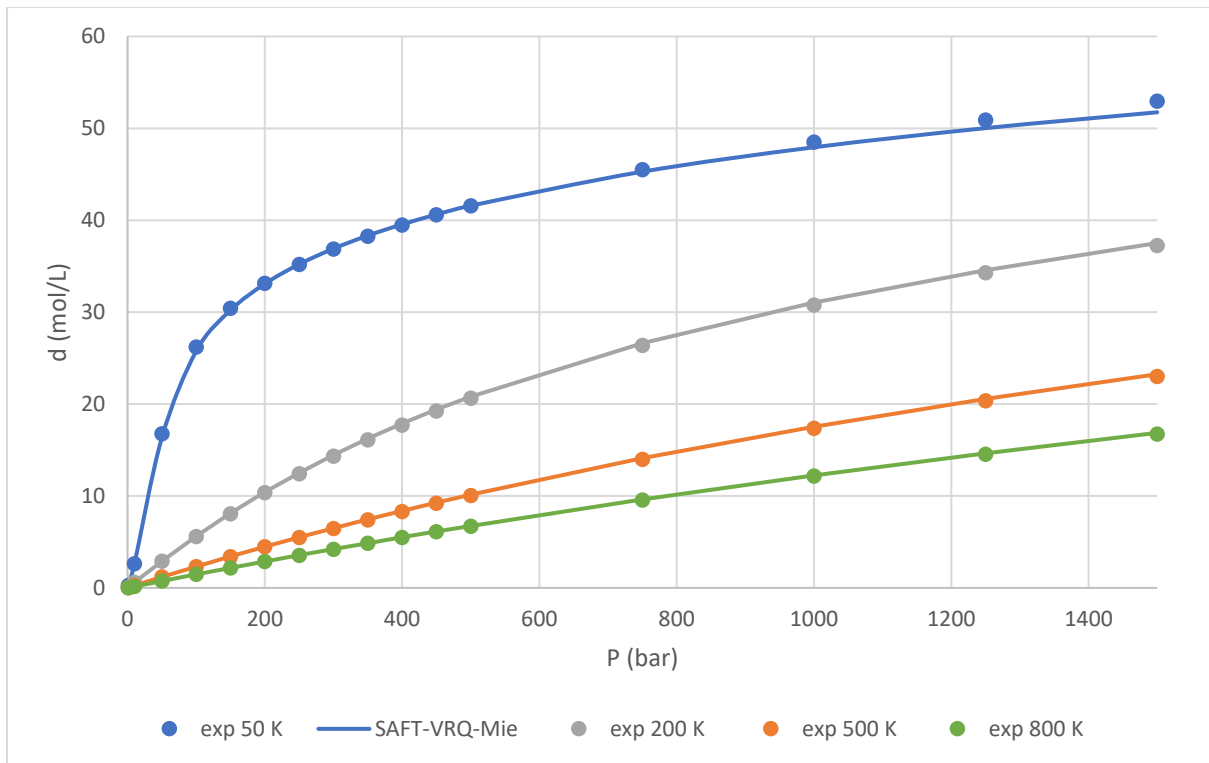
Figure 28: SAFT-VRQ-Mie prediction of density of pure hydrogen

From the results in *Table 23* and *Figure 28* above, it can be concluded that the density of pure hydrogen in supercritical conditions is predicted with high accuracy with SAFT-VRQ-Mie. Overall, the prediction is improved as the temperature increases and as pressure decreases.
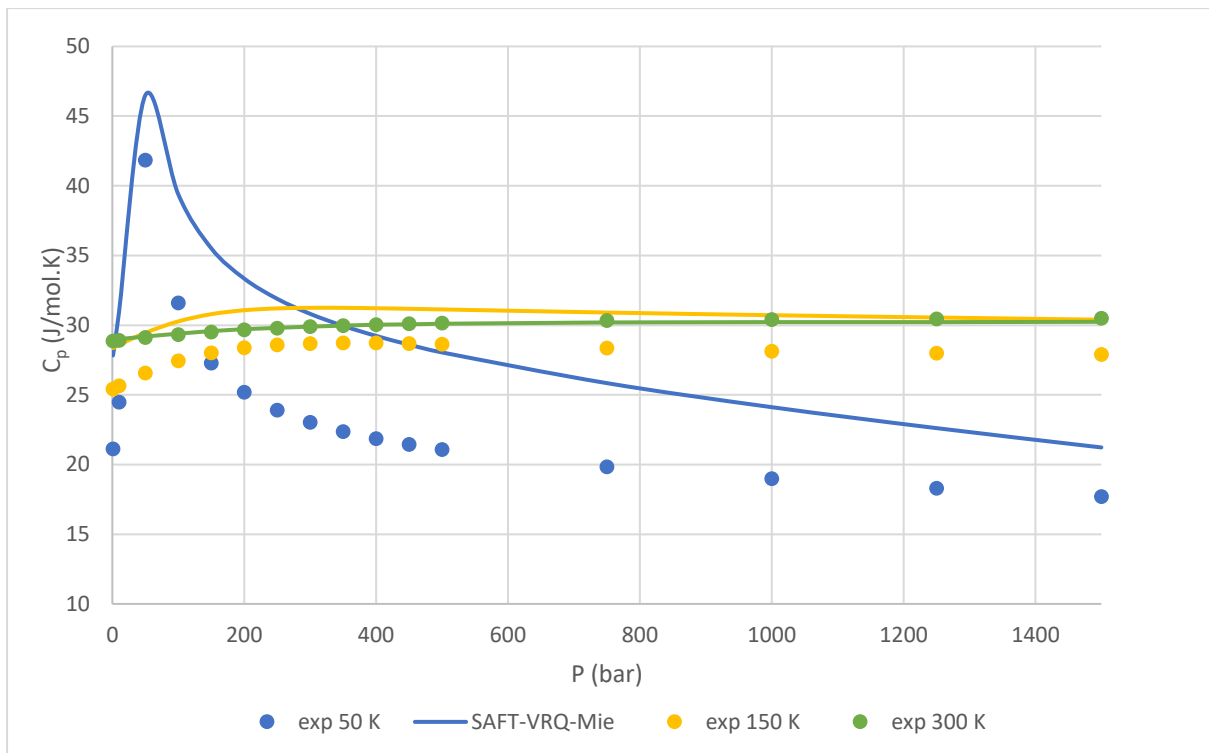
Figure 29: SAFT-VRQ-Mie prediction of isobaric heat capacity of pure hydrogen

Similarly to the calculations performed with Peng-Robinson, as shown in *Table 23* and *Figure 29* above, the prediction of the supercritical isobaric heat capacity is improved vastly as the temperature increases. In the lowest temperature range examined of 50-100 K the prediction is not highly accurate as the average deviation is greater than 19%. Regarding the effect of pressure in the calculations, up to 250 K the deviation decreases as the pressure increases but the opposite is true for temperatures higher than that.
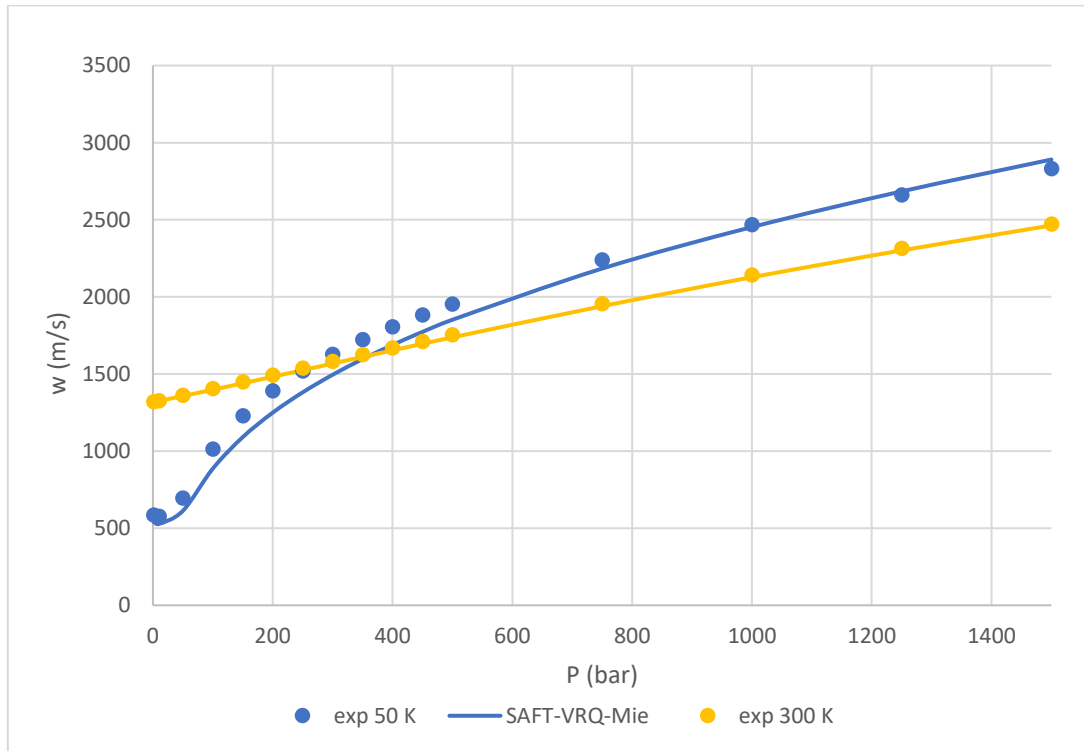
Figure 30: SAFT-VRQ-Mie prediction of speed of sound of pure hydrogen

The speed of sound prediction for pure hydrogen using SAFT-VRQ-Mie is improved as the temperature increases as it can be seen in *Table 23* and *Figure 30* above. The calculations are also improved as the pressure increases. In general, in the higher temperatures, above 200 K, the speed of sound is almost a linear function of the pressure and this linearity can be adequately reproduced by the model. In the lower temperatures however, the function displays a curvitude that cannot be accurately replicated by the model. This observation is evident in *Figure 30* above.
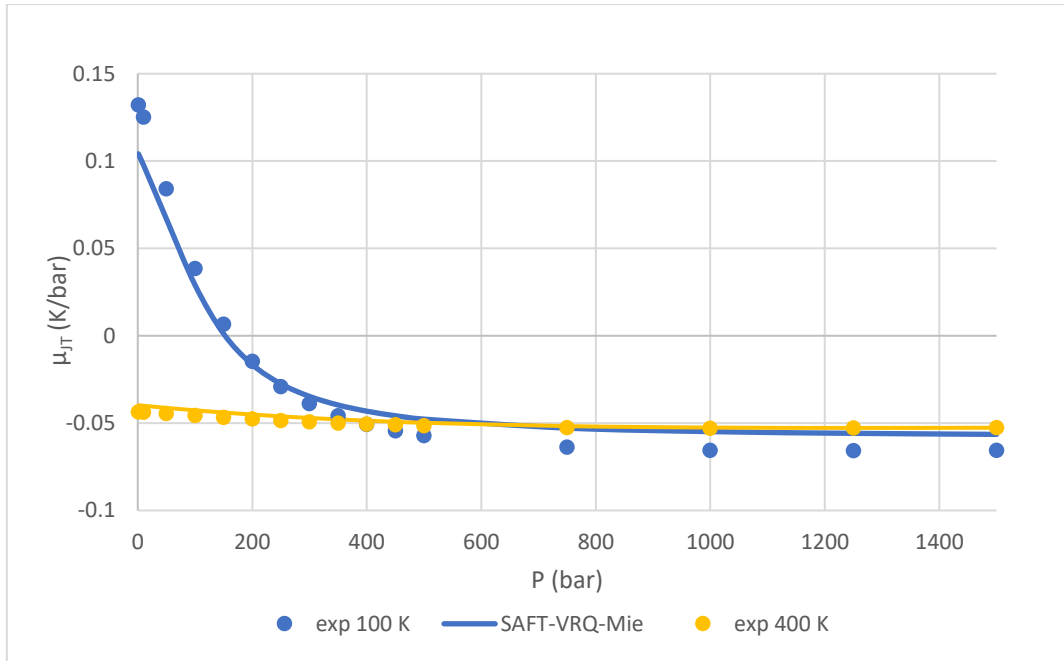
Figure 31: SAFT-VRQ-Mie prediction of Joule-Thomson coefficient of pure hydrogen

The prediction of the Joule-Thomson coefficient is poorer in the lowest temperatures, below 150 K, as it can be seen in *Table 23* and *Figure 31* above. Similarly to the speed of sound, the function of the Joule-Thomson coefficient in relation to pressure is approximately linear in temperatures above 100 K and thus the prediction is highly accurate. The deviation from the experimental data is minimized in the temperature range of 200-250 K but in general it is kept really low in higher temperatures than that, approximately 0.003 in absolute terms.

3.7 Summary of calculations

The summary of all calculations made in this work for pure hydrogen, is presented in terms of relative deviation (with the exception of the Joule-Thomson coefficient which is expressed in terms of absolute deviation) are presented in *Tables 24* and *25* below, for the subcritical and supercritical domain respectively.

Table 24: Summary of calculations of pure hydrogen in subcritical conditions

%AAD	PR	SAFT-VRQ-Mie
P^s	4.0	6.4
v_v	6.0	7.3
v_l	3.8	1.2
v_l*	15.9	

*This deviation regards no introduction of volume translation in the calculations.

Table 25: Summary of calculations of pure hydrogen in supercritical conditions

%AAD

T (K)	v PR untrans	v PR trans	v SAFT-VRQ-Mie	C_p PR	C_p SAFT-VRQ-Mie	w PR untrans	w PR trans	w SAFT-VRQ-Mie	μ_{JT} PR untrans	μ_{JT} PR trans	μ_{JT} SAFT-VRQ-Mie
50	7.2	3.3	0.8	25.5	28.6	17.3	22.8	6.8	0.026	0.021	0.030
100	5.8	3.3	0.2	10.7	19.5	9.2	10.4	5.6	0.012	0.006	0.010
150	5.1	3.0	0.6	3.9	9.5	5.7	6.8	3.0	0.016	0.011	0.002
200	4.4	2.5	0.7	1.5	3.8	3.9	5.0	1.5	0.017	0.013	0.001
250	3.8	2.1	0.7	1.0	1.1	2.9	4.0	0.9	0.018	0.013	0.001
300	3.3	1.7	0.7	0.9	0.3	2.3	3.3	0.6	0.019	0.013	0.002
400	2.4	1.2	0.7	0.3	0.4	1.6	2.5	0.5	0.019	0.013	0.002
500	1.8	0.9	0.6	0.4	0.2	1.2	2.1	0.4	0.019	0.013	0.003
600	1.4	0.8	0.5	0.3	0.1	0.9	2.0	0.4	0.019	0.012	0.003
700	1.0	0.6	0.5	0.2	0.1	0.7	1.9	0.3	0.018	0.011	0.003
800	0.7	0.6	0.4	0.2	0.2	0.6	1.8	0.3	0.017	0.010	0.003
900	0.5	0.7	0.4	0.2	0.2	0.6	1.8	0.2	0.017	0.009	0.003
1000	0.4	0.8	0.3	0.3	0.2	0.6	1.7	0.2	0.016	0.008	0.003
Overall	**2.9**	**1.7**	**0.5**	**3.5**	**4.9**	**3.7**	**5.1**	**1.6**	**0.018**	**0.012**	**0.005**

3.8 Peng-Robinson and SAFT-VRQ-Mie comparison

3.8.1 Subcritical Region

Comparing the Peng-Robinson and SAFT-VRQ-Mie models in their ability to accurately predict pure hydrogen's properties in the subcritical region, Peng-Robinson can better predict the saturated pressure and saturated vapor volume, but SAFT-VRQ-Mie can replicate with outstanding accuracy the saturated liquid volume.

In a more detailed analysis regarding the vapor pressure, it can be observed that the two models yield similar results, with PR having a lower %AAD. More specifically, in the lower temperatures where the relative deviations calculated are high and thus bring up the value of the average deviation, the experimental values of the saturated pressure is low and small absolute deviations are translated in large relative deviations. It is in these low temperatures that Peng-Robinson has the edge, as well as in temperatures approximating the critical point, 30 K and up. In the in between temperature range, the SAFT-VRQ-Mie calculations are optimal. The above observations are visualized in *Figure 32* below.
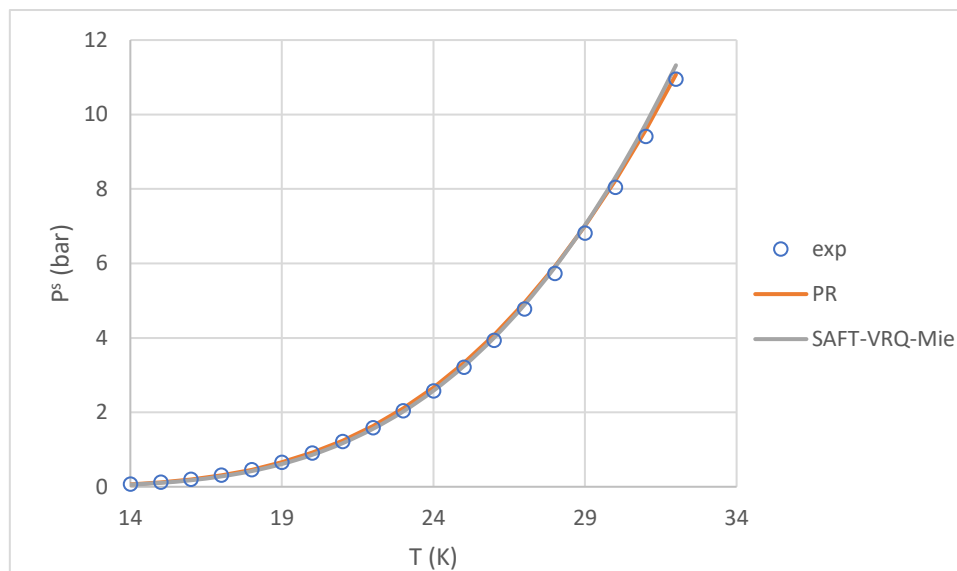
Figure 32: Saturated pressure calculations comparison between Peng-Robinson and SAFT-VRQ-Mie

Comparing the saturated vapor volume calculations, both models yield large deviations at lower temperatures, PR in the range of 14-17 K and SAFT-VRQ-Mie in the range 14-21 K, as they overestimate the values. Up until 22 K the prediction with PR is superior but in higher temperatures the prediction with SAFT-VRQ-Mie yields substantially smaller relative deviations. These observations are visualized in *Figure 33* below.
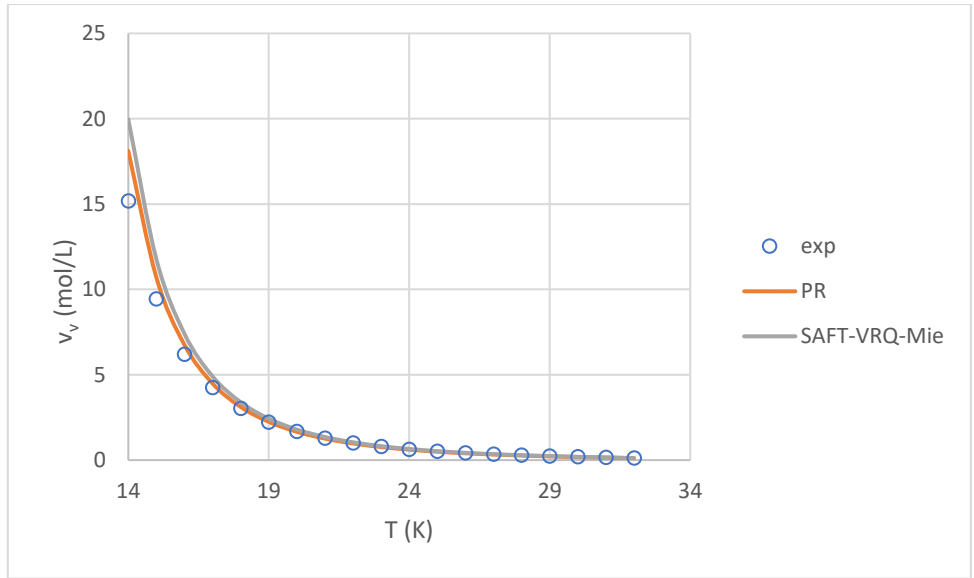
Figure 33: Saturated vapor volume calculations comparison between Peng-Robinson and SAFT-VRQ-Mie

Finally, the saturated liquid volume is reproduced by SAFT-VRQ-Mie with high accuracy, outperforming Peng-Robinson with volume translation.

3.8.2 Supercritical Region

Comparing the supercritical volume prediction, the average deviation at all isothermal curves examined is smaller in the SAFT-VRQ-Mie calculations, and it is less than 1%. The difference between the models is more evident as the temperature decreases. *Figure 34* below compares the calculations with the two models at selected isothermal curves.
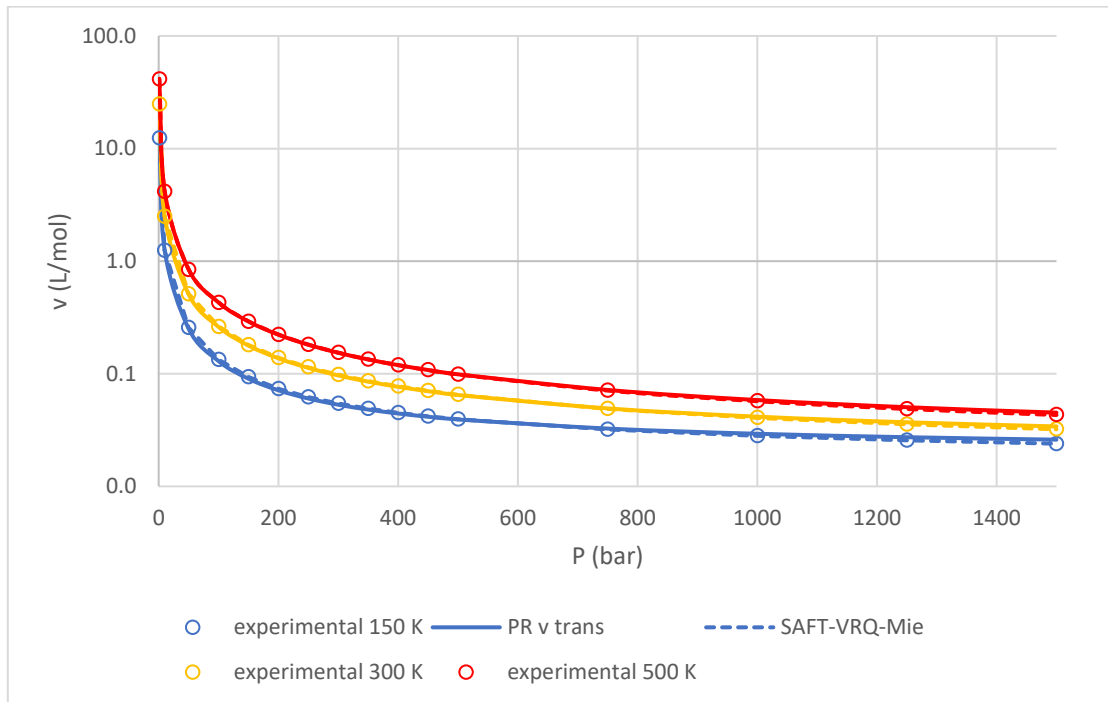
Figure 34: Supercritical volume calculations comparison between Peng-Robinson and SAFT-VRQ-Mie

As far as the isobaric heat capacity is concerned, it is significant to highlight that a different ideal gas contribution is employed in each model. Comparing the direct results of the models, Peng-Robinson is overall more accurate, although at temperatures higher than 500 K, SAFT-VRQ-Mie replicates the experimental data with slightly higher precision. Above 400 K both models reproduce the isobaric heat capacity with high accuracy. No specific effect of the pressure can be observed in the comparison of the models. *Figure 35* below compares the calculations with the two models at selected isothermal curves.
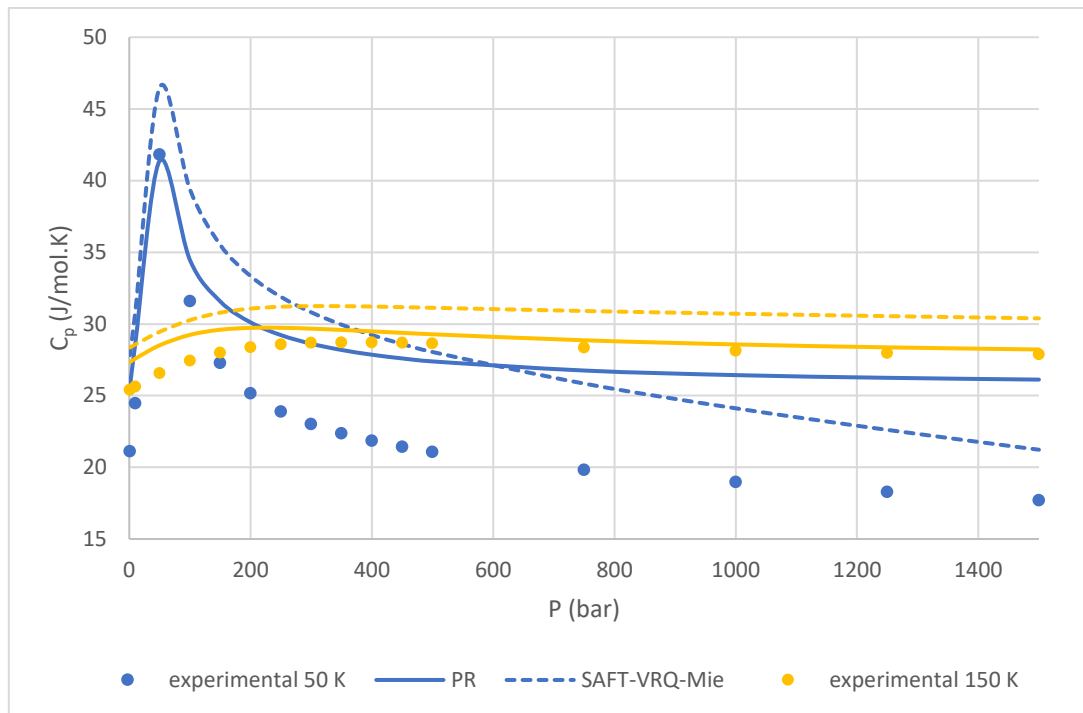
Figure 35: Isobaric heat capacity calculations comparison between Peng-Robinson and SAFT-VRQ-Mie

Comparing the speed of sound calculations, SAFT-VRQ-Mie yields more accurate results, especially at temperatures lower than 400 K. Peng-Robinson yields larger deviations as the pressure increases whereas the opposite is true for the SAFT-VRQ-Mie calculations. It is therefore in the higher pressure range, above 500 bar, that the discrepancy between the models is more substantial. *Figure 36* below is a visualization of the comparison of the two models in the prediction of the speed of sound, where the translated Peng-Robinson is plotted.
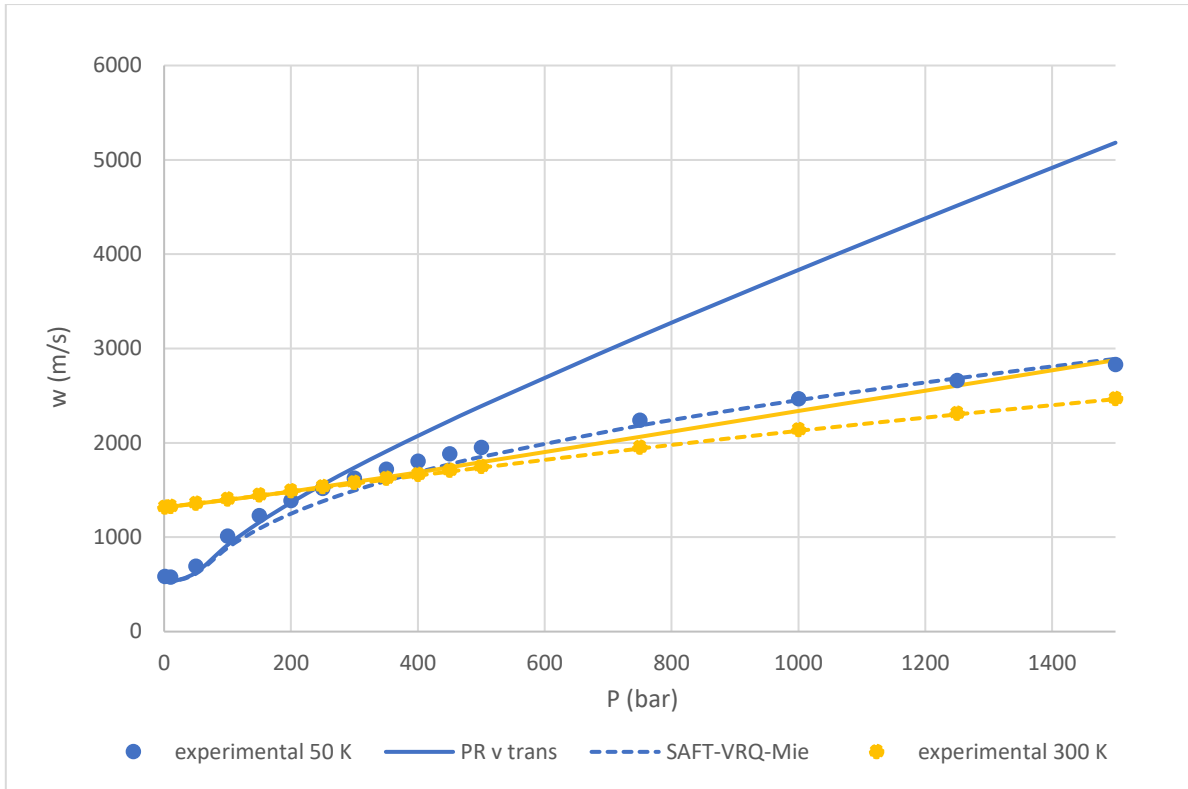
Figure 36: Speed of sound calculations comparison between Peng-Robinson and SAFT-VRQ-Mie

Finally, comparing the Joule-Thomson coefficient calculations made with the volume-translated Peng-Robinson and SAFT-VRQ-Mie, the latter has the edge. At temperatures higher than 100 K and up to 800 K, the deviation from the experimental data with SAFT-VRQ-Mie is smaller by a magnitude of 10. The largest discrepancies between the models are observed in the lower pressure range, below 500 bar. These remarks are visualized in *Figure 37* below.
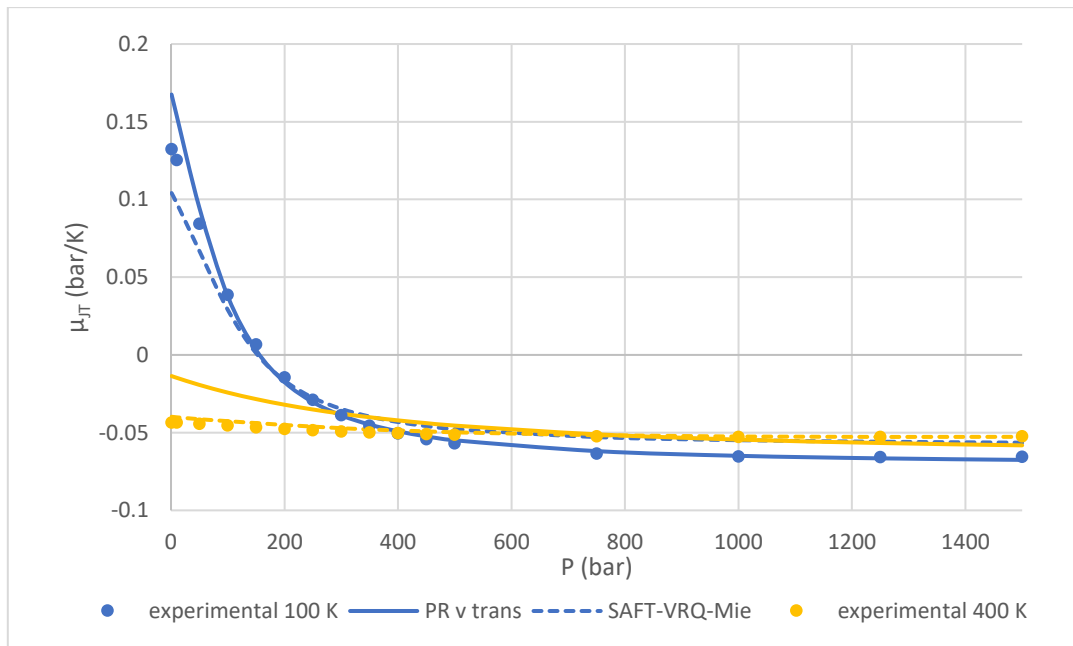
Figure 37: Joule-Thomson coefficient calculations comparison between Peng-Robinson and SAFT-VRQ-Mie

65

3.8.3 Conclusion

Overall, the SAFT-VRQ-Mie model is able to better predict the properties of pure hydrogen, especially in the supercritical region. The only property out of the ones examined in this work that is better reproduced overall with Peng-Robinson is the isobaric heat capacity, but the difference in the ideal gas contribution should be taken into consideration. In the subcritical region, Peng-Robinson is better at predicting the vapor pressure and the saturated vapor volume, although the vapor pressure calculations are very comparable with SAFT-VRQ-Mie.

4 Binary Mixtures

Hydrogen is very commonly found in mixtures in various industrial applications. One of the most important mixtures is the mixture of hydrogen with natural gas (NG). Natural gas is comprised of a variety of components, mainly hydrocarbons and light gases. That is why the mixtures of hydrogen with hydrocarbons are of high interest and will be examined. Other mixtures of special interest are the mixtures of hydrogen with aromatic compounds, known as hydrogen carriers that are used in storage and transport processes.

In order to properly design the various applications relative to hydrogen-NG fluids, it is of outmost importance to accurately describe the Vapor-Liquid Equilibrium (VLE) behaviour of such systems. For this purpose, the PR EoS is extended to hydrogen-NG constituents' mixtures in the framewok of a quite extended VLE database of the studied binary mixtures. The aforementioned database is presented in *Table 26* along with temperature, pressure and composition ranges.

Table 26: Binary Mixtures examined in this work

Binary Mixture	T range (K)	P range (bar)	H_2 liquid composition range	H_2 vapor composition range	Experimental points (NDP)
$H_2 - C_1$	90.70 – 183.15	2.2 – 690.7	0.0018 – 0.6103	0.0338 – 0.9924	374
$H_2 - C_2$	92.50 – 283.15	16.7 – 691.5	0.0022 – 0.5358	0.0847 – 0.9996	163
$H_2 - C_3$	172.05 – 360.93	13.79 – 551.58	0.0061 – 0.4007	0.1420 – 0.9990	98
$H_2 - nC_4$	144.26 – 394.25	20.68 – 541.24	0.0080 – 0.3410	0.2130 – 0.9999	110
$H_2 - nC_5$	273.15 – 443.15	3.47 – 275.90	0.0016 – 0.2590	0.3730 – 0.9964	101
$H_2 - nC_6$	298.15 – 410.9	12.4 – 151.1	0.0105 – 0.1430	-	58
$H_2 - nC_8$	295.00 – 523.15	10.1 – 173.3	0.0054 – 0.2258	0.1635 – 0.9999	54
$H_2 - nC_{10}$	293.15 – 573.15	14.8 – 173.9	0.0158 – 0.1507	-	110
$H_2 - CO_2$	218.16 – 293.15	5.58 – 203.16	0.0000 - 0.1790	0.0000 – 0.9999	149
H_2 – benzene	288.15 – 533.15	5.25 – 689.27	0.0017 – 0.2430	0.0998 – 0.9956	112
H_2 – toluene	295.00 – 542.15	8.74 – 323.00	0.0027 – 0.3270	0.2100 – 0.9999	66
H_2 – cyclohexane	293.15 – 493.15	5.67 – 690.37	0.0029 – 0.2919	0.8582 – 0.9999	196
H_2 – methylcyclohexane	295.00 – 498.85	24.50 – 686.50	0.0170 – 0.5430	0.4640 – 0.9999	29

H$_2$ – pxylene	353.15 – 573.15	26.66 – 148.75	0.0281 – 0.1550	-	107
H$_2$ – mxylene	295.00 – 583.15	19.86 – 254.40	0.0091 – 0.2494	0.2870 – 0.9999	92

4.1 Experimental Data Collection

The evaluation of the efficiency of the calculations is based on comparison to experimental data found in literature. In general, most of the data is old as it was collected in experiments before the 1990's and there are a lot of datasets dating back to the 1930's. Out of the binary systems examined, the binaries of hydrogen with methane, ethane, carbon dioxide and cyclohexane have the most available experimental data. A lack of data for the vapor phase composition is noticed in many datasets. A lack of data in low temperatures below 100 K is also highlighted. Experimental data for the mixtures containing heavier compounds is available only in elevated temperatures of approximately 300 K and above.

It is important to note that each set of experimental data is subject to experimental uncertainty. That is why not all the datasets found in literature are employed in this work and *Table 26* only consists of the data deemed reliable. An evaluation of the datasets' reliability was performed while regressing the experimental data to determine an optimal binary interaction coefficient, as explained in Section 4.2 below. While examining data in adjacent isothermal curves, abnormally large deviations between bubble point pressure values in mixtures of similar liquid composition suggested unreliable data.

4.2 Modeling

In this work, the correlation and prediction of the vapor-liquid equilibrium of the mixtures stated in *Table 26* above was carried out. For correlating the VLE data the following objective function was minimized (Eq.31) in terms of the bubble point pressure calculation.

$$F = \frac{1}{NDP} \sum \frac{P_{calc} - P_{exp}}{P_{exp}} \qquad (Eq.31)$$

where P_{exp} refers to the experimental bubble point pressure and P_{calc} to the calculated value.

The reason for minimizing the bubble point pressure and not the vapor phase composition is the higher importance of the first property in technical applications and the absence of the vapor phase composition in many experimental works.

Three sets of calculations were performed with a different binary interaction coefficient for each binary mixture. The first value, the optimal temperature-dependent k$_{ij}$ was obtained by individually regressing each isothermal curve of experimental data. Then, these k$_{ij}$ values were plotted with regard to temperature and simple linear or quadratic functions (k$_{ij}$=f(T)) were developed, after removing unreliable data. These functions were

used for the prediction of the studied VLE data. Finally, an optimal temperature-independent k_{ij} value was obtained by a single regression of all reliable experimental data up to 700 bar.

The evaluation of the efficiency of the coefficients obtained was assessed through the deviation of the calculated bubble point pressure and the hydrogen vapor molar fraction. The calculation of the deviation of the bubble point pressure is performed through *Equation 26*. The deviation in the vapor phase composition calculations is expressed in absolute terms, as seen in *Equation 32*, and the final results will be presented multiplied by 100.

$$AADy = \sum_{1}^{NP} |y_{exp} - y_{calc}| \qquad\qquad (Eq.\,32)$$

where y_{exp} and y_{calc} are the experimental and calculated values of the vapor phase molar fraction of hydrogen.

4.3 $H_2 - C_1$

The binary mixture of hydrogen with methane is a mixture of special interest, due to the mixing of hydrogen with natural gas, which is very rich in methane.

The datasets that were used in the development of the model are listed in *Table 27* below.

Table 27: VLE datasets for binary mixture $H_2 - C_1$

NDP	T (K)	P range (bar)	y range	x range	Reference
4	172.0	34.5 - 103.4	0.158 - 0.468	0.017 - 0.162	Benham et al. 1957 [34]
6	123.2	10.2 - 101.8	0.683 - 0.911	0.007 - 0.101	Sagara et al. 1972 [35]
2	172.1	87.5 - 103.6	0.429 - 0.435	0.136 - 0.201	Sagara et al. 1972 [35]
9	173.7	35.7 - 108.3	0.148 - 0.424	0.017 - 0.225	Sagara et al. 1972 [35]
16	183.1	39.2 - 75.4	0.034 - 0.203	0.007 - 0.149	Hong et al. 1981 [36]
13	173.3	30.6 - 114.8	0.088 - 0.426	0.009 - 0.262	Hong et al. 1981 [36]
15	163.2	21.7 - 159.6	0.119 - 0.596	0.006 - 0.380	Hong et al. 1981 [36]
12	133.1	27.5 - 275.8	0.780 - 0.875	0.027 - 0.357	Hong et al. 1981 [36]
8	118.2	41.7 - 206.8	0.918 - 0.941	0.039 - 0.194	Hong et al. 1981 [36]
11	113.1	28.2 - 284.1	0.916 - 0.957	0.024 - 0.234	Hong et al. 1981 [36]
32	92.3	2.2 - 1379.8	0.756 – 0.999	0.002 - 0.588	Tsang et al. 1980 [37]
27	100.0	5.1 - 945.8	0.740 – 0.999	0.004 - 0.610	Tsang et al. 1980 [37]
32	110.0	3.4 - 639.0	0.690 – 0.999	0.002 - 0.607	Tsang et al. 1980 [37]
16	130.0	8.1 - 340.1	0.625 - 0.893	0.005 - 0.452	Tsang et al. 1980 [37]
15	140.0	15.9 - 278.5	0.578 - 1.000	0.012 - 0.475	Tsang et al. 1980 [37]
14	150.0	15.5 - 224.1	0.443 - 0.749	0.009 - 0.471	Tsang et al. 1980 [37]
14	159.2	24.3 - 173.2	0.266 - 0.649	0.015 - 0.363	Tsang et al. 1980 [37]
10	170.0	37.4 - 128.2	0.244 - 0.482	0.027 - 0.293	Tsang et al. 1980 [37]
9	180.0	47.6 - 86.7	0.161 - 0.273	0.033 - 0.181	Tsang et al. 1980 [37]
9	90.7	10.3 - 126.9	0.985 - 0.992	0.008 - 0.075	Kirk et al. 1965 [38]

3	93.2	101.3 - 152.0	0.977 - 0.987	0.046 - 0.080	Yorizane et al. 1980 [39]
5	120.5	4.8 - 17.7	0.529 - 0.880	0.003 - 0.018	Hu et al. 2014 [40]
5	100.1	2.4 - 13.3	0.932 - 0.983	0.002 - 0.013	Hu et al. 2014 [40]

By fitting all datasets that were used in the k_{ij} – T correlation, up to 700 bar, a temperature-independent value for k_{ij} equal to -0.0059 was obtained.

By fitting each individual isothermal curve, a temperature-dependent k_{ij} value was obtained. By plotting these values as a function of temperature, the following chart in *Figure 38* was obtained and by performing a polynomial regression, second degree *Equation 33* was derived to predict the k_{ij} value for a given temperature in Kelvin.

$$k_{ij}(T) = 2.41038 \cdot 10^{-5} T^2 - 4.70912 \cdot 10^{-3} T + 2.43232 \cdot 10^{-1} \qquad (Eq.33)$$
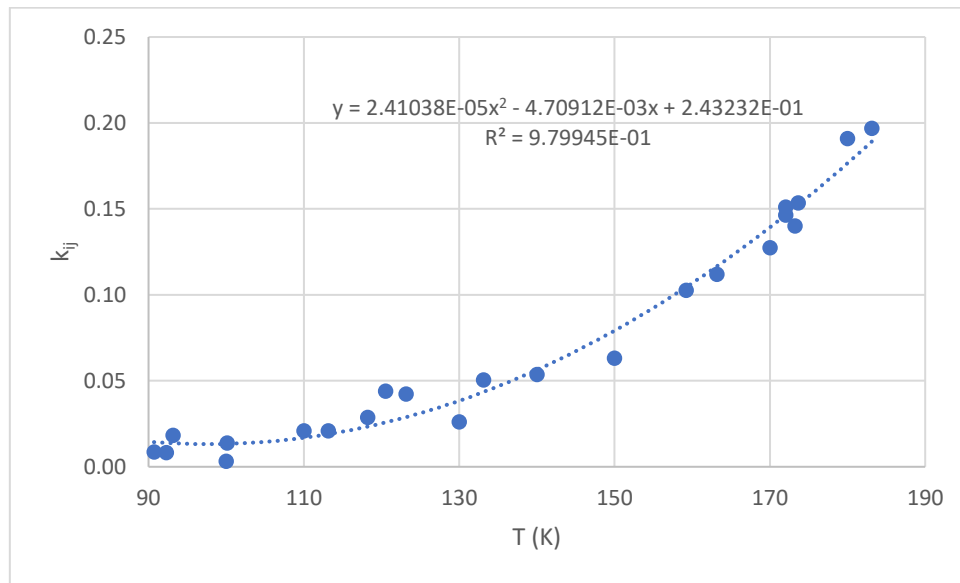
Figure 38: kij – T plot for binary mixture H_2-C_1

All the temperature-dependent k_{ij} values are presented below in *Table 28*. It is noted that due to very poor predictions in high pressures in the isothermal curves of 100 and 110 K, both datasets by Tsang et al. [37], the fitting was performed for a pressure range of up to 300 bar. The presence of these pressure values led to k_{ij} values that were not aligning with the equation derived from the rest of the k_{ij} values obtained from the other datasets.

Using Equation *33*, a k_{ij} value was calculated for each temperature and bubble point calculations were made. The comparison between the calculations in the bubble point pressure and the composition of the vapor phase using the temperature-independent k_{ij}, the temperature-dependent and the calculated k_{ij} values are presented in *Table 28* below.

Table 28: Comparison between different binary interaction coefficient values in the VLE prediction of H_2-C_1

		optimal k_{ij} T independent			optimal k_{ij} T dependent			k_{ij} trendline		
T (K)	P range (bar)	value	%AADP	100AADy	value	%AADP	100AADy	value	%AADP	100AADy
90.7	10.3 - 126.9	-0.0059	6.6	0.13	0.0087	3.5	0.13	0.0144	6.7	0.13

92.3	2.2 - 690.7	-0.0059	12.0	0.58	0.0082	11.5	0.62	0.0139	15.8	0.66
93.2	101.3 - 152.0	-0.0059	22.7	0.37	0.0183	21.7	0.29	0.0137	21.9	0.30
100.0	5.1 - 277.1	-0.0059	8.6	0.28	0.0133	5.5	0.32	0.0133	5.5	0.41
100.1	2.3 - 13.33	-0.0059	10.3	5.99	0.0138	6.6	5.30	0.0133	6.7	5.32
110.0	3.4 - 276.4	-0.0059	12.9	1.36	0.0208	5.4	0.96	0.0168	6.0	1.01
113.1	28. - 284.1	-0.0059	15.1	0.94	0.0208	9.2	0.85	0.0189	9.2	0.86
118.2	41.7 - 206.8	-0.0059	15.2	1.02	0.0288	5.6	0.84	0.0233	5.7	0.87
120.5	4.8 - 17.7	-0.0059	11.6	4.56	0.0440	2.6	2.36	0.0257	4.8	2.90
123.2	10.2 - 101.8	-0.0059	16.7	1.74	0.0422	7.5	1.61	0.0288	9.7	1.49
130.0	8.1 - 340.1	-0.0059	13.6	3.76	0.0261	7.9	3.13	0.0383	8.2	2.87
133.1	27.5 - 275.8	-0.0059	18.4	2.13	0.0504	6.6	1.04	0.0435	7.5	1.18
140.0	15.9 - 278.5	-0.0059	16.7	7.68	0.0536	6.9	6.01	0.0563	6.9	5.93
150.0	15.5 - 224.1	-0.0059	15.6	5.25	0.0631	5.9	3.52	0.0791	6.2	3.20
159.2	24.3 - 173.2	-0.0059	15.5	3.59	0.1026	3.6	1.05	0.1043	3.6	1.02
163.2	21.7 - 159.6	-0.0059	13.3	3.18	0.1120	3.4	1.66	0.1165	3.6	1.63
170.0	37.4 - 128.2	-0.0059	14.7	3.31	0.1273	3.3	1.61	0.1392	3.4	1.65
172.0	34.5 - 103.4	-0.0059	17.3	5.32	0.1510	5.9	1.50	0.1464	6.3	1.63
172.1	87.5 - 103.6	-0.0059	15.1	2.64	0.1464	3.9	1.56	0.1464	3.9	1.56
173.3	30.7 - 114.8	-0.0059	12.4	3.57	0.1401	2.5	2.26	0.1508	3.1	2.26
173.7	35.7 - 108.3	-0.0059	13.7	4.64	0.1535	3.6	1.81	0.1522	3.6	1.81
180.0	47.6 - 86.7	-0.0059	12.0	1.85	0.1908	2.0	1.60	0.1764	5.4	2.52
183.1	39.2 - 75.4	-0.0059	7.2	2.90	0.1968	6.0	1.81	0.1890	6.8	1.86
			13.3	**2.73**		**6.0**	**1.79**		**6.9**	**1.83**

Some typical examples of comparisons of plots of the VLE envelope with the calculations are shown in *Figures 39* and *40* below.
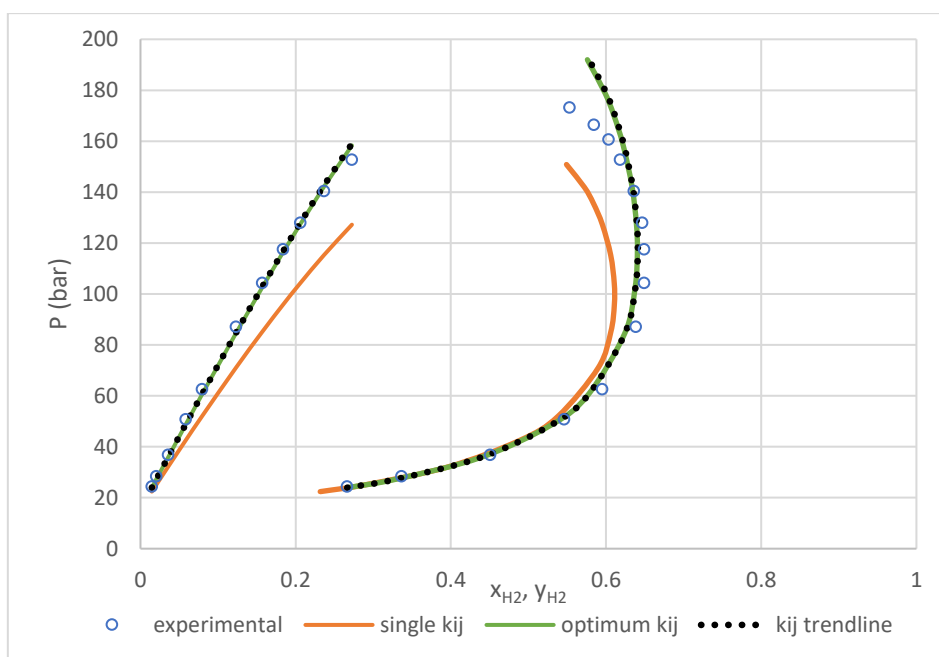
Figure 39: VLE envelope for H_2 – C_1 at T=159.2K
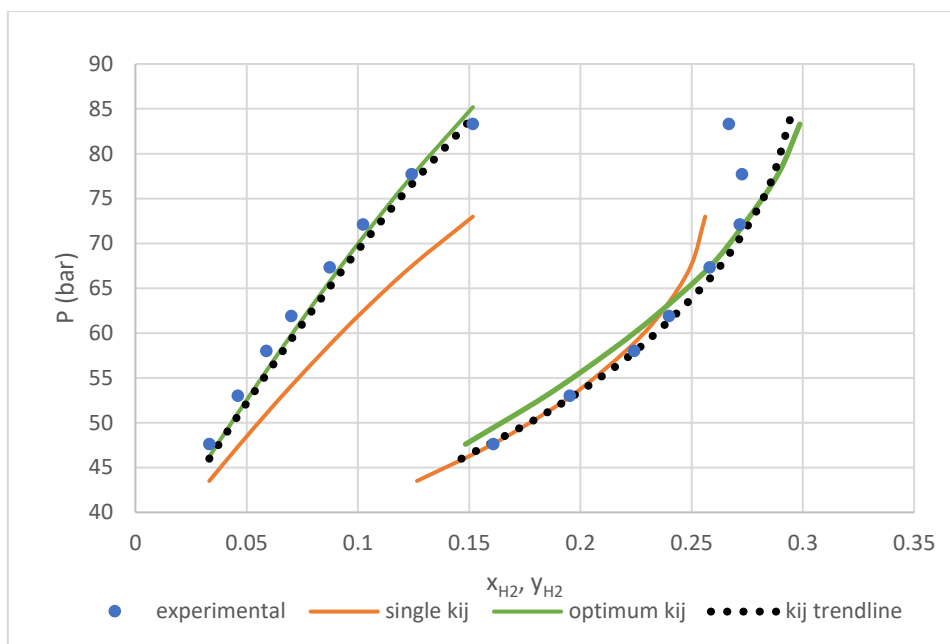
Figure 40: VLE envelope for $H_2 - C_1$ in T=180.0K

From the results of *Table 28* above, it is obvious that introducing a temperature-dependent k_{ij} value, the correlation of the bubble point pressure of the binary mixture of $H_2 - C_1$ improves significantly, as the average deviation is brought down to less than half. More specifically, by using a temperature-independent k_{ij} the average deviation is 13.3% whereas with the optimal k_{ij} values obtained by the isothermal curves fitting, it is 6.0%. The prediction using the model derived from the trendline, is satisfactory with an average deviation up to 6.9%.

The prediction of the vapor phase composition is in general easier to predict accurately than the bubble point pressure. This becomes apparent by comparing the average deviations occurred with the three different k_{ij} values. Using the temperature-independent k_{ij} the average deviation multiplied by 100 is 2.73, and with the optimal k_{ij} values it is equal to 1.79. The results from the model developed yield an average deviation of 1.83. The vapor phase composition is therefore more accurately predicted, even with the temperature-independent k_{ij} that results in more significant deviations in the bubble point pressure even if the deviation in the calculation of the bubble point pressure is significant.

It is also important to note as well that in some isothermal curves, the vapor phase predictions using the k_{ij} value derived from the model leads to a lower deviation from the experimental data than when using the temperature-independent optimal k_{ij} (e.g. at 180 K). That is because the objective function used in the regression, minimizes the error of the calculation of the bubble point pressure. Nonetheless, overall, the optimal temperature-dependent interaction parameters and the trendline as well, lead to better results in vapor phase predictions.

By examining *Figures 39* and *40*, it can be observed that the bubble point pressure is underestimated when using the temperature-independent k_{ij} coefficient. The discrepancy between the calculated value and the experimental one grows significantly as the

pressure increases. The same observation applies to the calculation of the vapor phase composition, as the molar fraction of hydrogen is underestimated.

Overall, as expected due to the difficulty of the EoS to accurately reproduce the phase envelope in the high pressures, the deviations in the calculation of the bubble point pressure is higher at high pressures.

4.4 $H_2 - C_2$

The datasets that were used in the development of the model are listed in *Table 29* below.

Table 29: VLE datasets for binary mixture $H_2 - C_2$

NDP	T (K)	P range (bar)	y range	x range	Reference
2	149.6	120.5 - 148.6	0.997 - 0.997	0.041 - 0.051	Hiza et al. 1967 [41]
5	169.4	24.6 - 149.9	0.978 - 0.989	0.012 - 0.065	Hiza et al. 1967 [41]
4	189.6	41.4 - 145.4	0.954 - 0.974	0.024 - 0.078	Hiza et al. 1967 [41]
6	144.3	16.7 - 533.5	0.992 - 0.998	0.006 - 0.133	Williams et al. 1954 [42]
6	172.1	16.7 - 533.5	0.958 - 0.988	0.008 - 0.201	Williams et al. 1954 [42]
6	199.9	16.7 - 533.5	0.850 - 0.961	0.008 - 0.280	Williams et al. 1954 [42]
6	227.6	16.7 - 533.5	0.581 - 0.907	0.008 - 0.400	Williams et al. 1954 [42]
5	255.4	16.7 - 266.7	0.107 - 0.787	0.002 - 0.279	Williams et al. 1954 [42]
4	283.2	33.3 - 166.7	0.085 - 0.526	0.007 - 0.245	Williams et al. 1954 [42]
4	198.2	20.3 - -81.1	0.881 - 0.951	0.011 - 0.045	Sagara et al. 1972 [35]
4	92.5	75.8 - 233.7	-	0.007 - 0.021	Heintz et al. 1982 [43]
7	95.2	129.6 - 462.0	-	0.014 - 0.035	Heintz et al. 1982 [43]
10	100.2	114.4 - 939.1	0.999 - 1.000	0.015 - 0.070	Heintz et al. 1982 [43]
12	107.9	81.7 - 1827.8	0.993 - 1.000	0.012 - 0.147	Heintz et al. 1982 [43]
9	113.9	590.6 - 2557.9	0.990 - 1.000	0.073 - 0.215	Heintz et al. 1982 [43]
12	120.2	477.5 - 3516.3	0.986 - 1.000	0.073 - 0.304	Heintz et al. 1982 [43]
23	129.8	75.0 - 5146.0	0.964 - 1.000	0.017 - 0.528	Heintz et al. 1982 [43]
36	149.5	51.4 - 4809.7	0.847 - 1.000	0.015 - 0.752	Heintz et al. 1982 [43]
15	161.2	539.4 - 3354.3	0.851 - 0.986	0.171 - 0.701	Heintz et al. 1982 [43]
28	189.6	57.5 - 1616.1	0.816 - 0.975	0.033 - 0.678	Heintz et al. 1982 [43]
11	212.2	39.4 - 963.3	0.799 - 0.943	0.026 - 0.601	Heintz et al. 1982 [43]
10	228.2	31.8 - 675.7	0.739 - 0.906	0.022 - 0.536	Heintz et al. 1982 [43]
11	240.2	47.9 - 531.8	0.725 - 0.865	0.034 - 0.515	Heintz et al. 1982 [43]
10	255.4	38.0 - 395.9	0.504 - 0.779	0.026 - 0.473	Heintz et al. 1982 [43]
8	268.2	39.0 - 293.8	0.344 - 0.696	0.023 - 0.414	Heintz et al. 1982 [43]
7	280.2	40.9 - 208.6	0.200 - 0.548	0.019 - 0.339	Heintz et al. 1982 [43]

All the temperature-dependent k_{ij} values that were obtained through regression, are presented below in *Table 30*. The correlation between the optimal temperature-dependent binary interaction coefficient and the temperature is given in *Equation 34.*

The optimal temperature-independent coefficient was determined to be equal to 0.0191.

The comparison between the calculations in the bubble point pressure and the composition of the vapor phase using the optimal temperature-independent k_{ij}, the optimal temperature-dependent and the calculated k_{ij} values from the correlation, are presented in *Table 30* below.

$$k_{ij}(T) = 3.96431 \cdot 10^{-6}T^2 - 2.48610 \cdot 10^{-4}T - 8.64596 \cdot 10^{-3} \qquad (Eq.\,34)$$
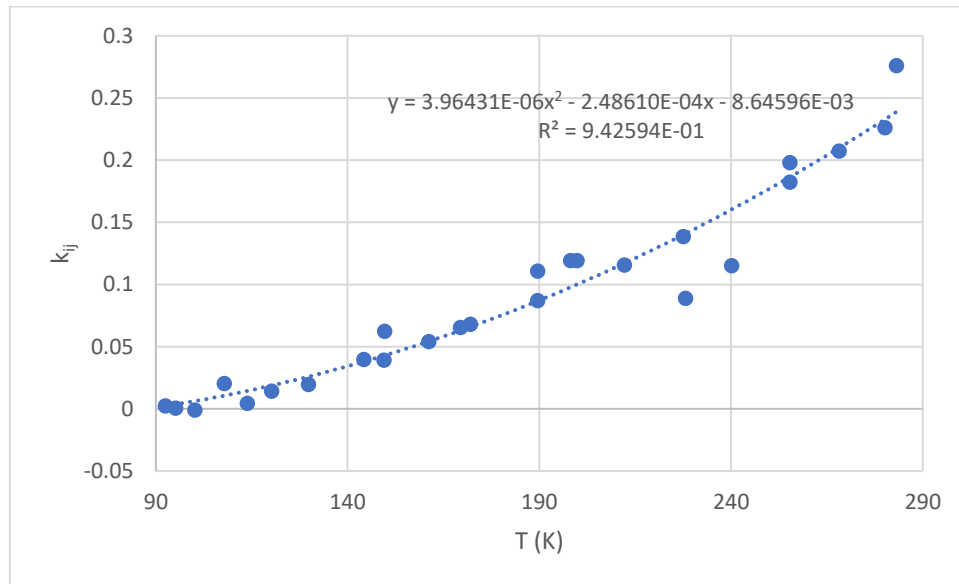
Figure 41: kij – T plot for binary mixture H_2-C_2

Table 30: Comparison between different binary interaction coefficient values in the VLE prediction of H_2-C_2

T (K)	P range (bar)	k_{ij} T independent value	%AADP	100AADy	optimal k_{ij} T dependent value	%AADP	100AADy	k_{ij} trendline value	%AADP	100AADy
92.5	75.8 - 233.7	0.0191	18.3	-	0.0022	10.3	-	0.0022	10.3	-
95.2	129.6 - 462.0	0.0191	19.3	-	0.0005	7.8	-	0.0036	8.4	-
100.2	114.4 - 651.5	0.0191	22.5	0.02	-0.0012	8.9	0.02	0.0062	11.5	0.02
107.9	81.7 - 655.2	0.0191	16.5	0.04	0.0203	16.4	0.04	0.0106	17.5	0.04
129.8	75.0 - 691.5	0.0191	12.2	0.06	0.0195	12.2	0.06	0.0258	13.1	0.05
144.3	16.7 - 533.5	0.0191	11.6	0.09	0.0397	7.9	0.10	0.0379	8.3	0.10
149.5	51.4 - 678.5	0.0191	15.8	0.22	0.0391	13.7	0.21	0.0427	14.3	0.21
149.6	120.5 - 148.6	0.0191	15.8	0.09	0.0622	1.7	0.08	0.0428	7.6	0.08
169.4	24.6 - 600.8	0.0191	17.1	0.32	0.0654	7.9	0.21	0.0629	8.0	0.22
172.1	16.7 - 533.5	0.0191	18.4	0.32	0.0680	8.8	0.27	0.0658	9.0	0.27
189.6	57.5 - 665.1	0.0191	19.4	0.67	0.0869	9.1	0.31	0.0865	9.1	0.31
189.6	41.4 - 145.4	0.0191	20.0	0.75	0.1108	0.7	0.16	0.0865	5.8	0.31
198.2	20.3 - 81.1	0.0191	29.2	2.18	0.1193	13.2	0.72	0.0976	17.0	1.02
199.9	16.7 - 533.5	0.0191	23.6	2.10	0.1193	10.8	0.78	0.0998	10.9	1.03
212.2	39.4 - 650.1	0.0191	21.2	1.78	0.1155	11.4	0.54	0.1168	11.6	0.53
227.6	16.7 - 533.5	0.0191	22.5	5.65	0.1385	10.7	2.92	0.1398	10.7	2.90
228.2	31.8 - 675.7	0.0191	20.1	2.39	0.0888	9.4	1.23	0.1408	16.1	1.25
240.2	47.9 - 531.8	0.0191	21.9	3.54	0.1151	9.9	2.05	0.1600	13.1	1.98

255.4	16.7 - 266.7	0.0191	16.4	6.52	0.1980	5.1	2.56	0.1861	5.2	2.70
255.4	38.0 - 395.9	0.0191	21.6	4.86	0.1823	8.5	2.35	0.1861	8.6	2.35
268.2	39.0 - 293.8	0.0191	20.5	5.60	0.2073	7.6	2.87	0.2094	7.6	2.87
280.2	40.9 - 208.6	0.0191	17.8	4.51	0.2261	5.7	3.51	0.2325	5.7	3.56
283.2	33.3 - 166.7	0.0191	14.6	6.53	0.2760	4.0	2.45	0.2384	4.2	2.60
			19.0	**2.28**		**8.9**	**1.15**		**10.1**	**1.18**

A visualized comparison between the calculations is shown in *Figures 42* and *43* below for the isothermal curves of 144.25 K and 240.15 K respectively.
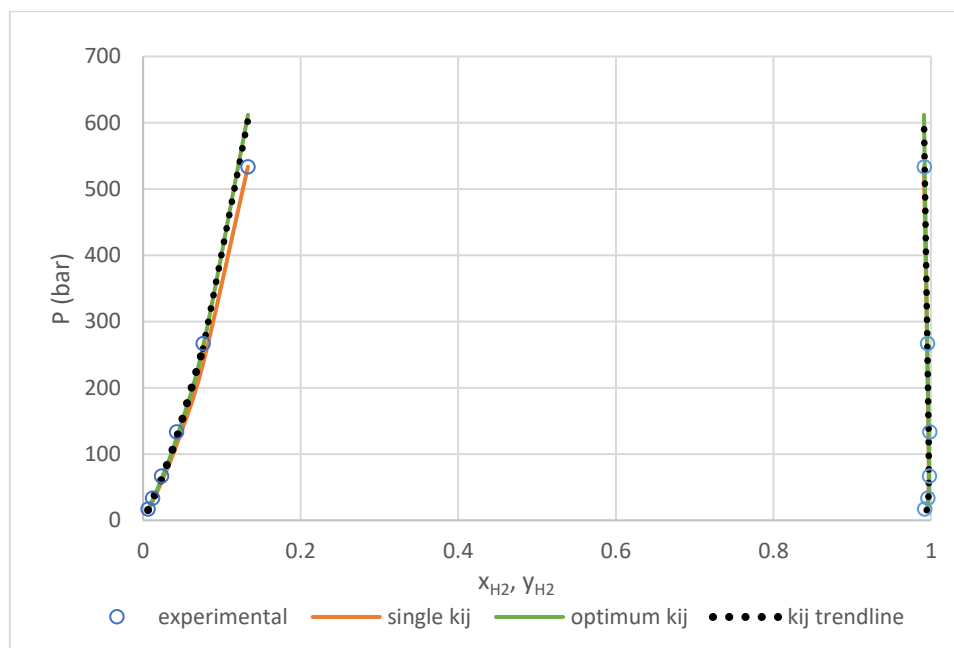
Figure 42: VLE envelope for H_2 – C_2 in T=144.25K
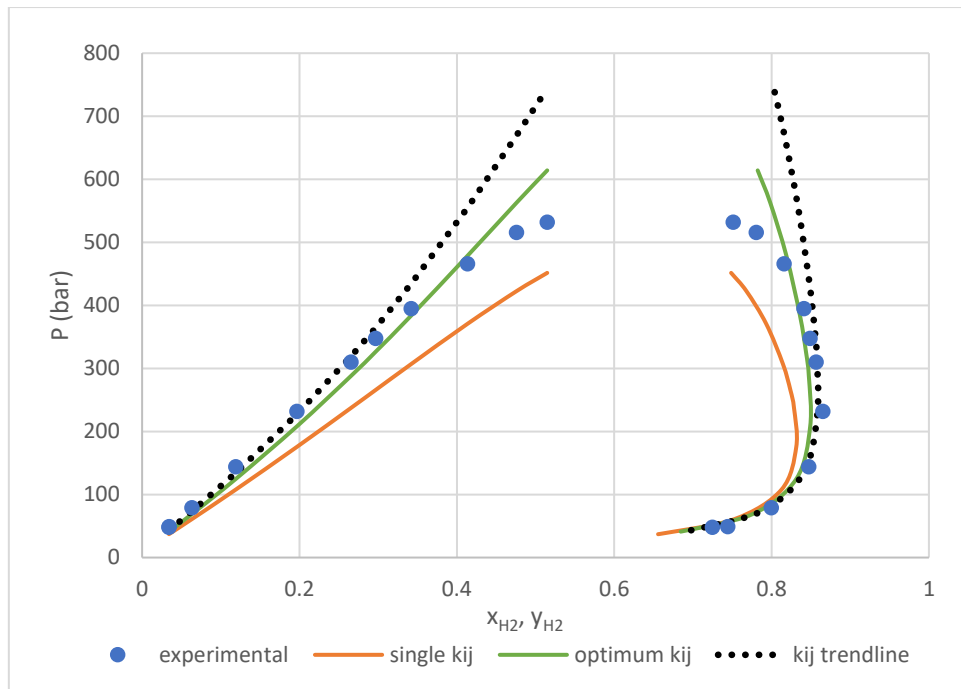
Figure 43: VLE envelope for H_2 – C_2 in T=240.15K

Comparing the results in *Table 30*, it is obvious that the introduction of the temperature dependency in the determination of the k_{ij} coefficient leads to very significant improvement in the prediction of the bubble point pressure of the mixture. The average deviation when using the temperature-independent k_{ij} is 19.0%, whereas the use of the optimal k_{ij} values brings down the average deviation to 8.9%. The developed trendline yields an average deviation of 10.1%. In general, the discrepancy between the calculations with the model and the optimal k_{ij} values occurs at the temperatures that the optimal k_{ij} value does not align closely with the trendline derived. The deviation from the trendline is linked to the experimental uncertainty among different experimental works as well as the different pressure range. This becomes more apparent when examining datasets in a very approximate temperature that yield a considerably different optimal k_{ij} value. Examples of this analysis, are the isothermal curves of 149.5 and 149.61 K and 255.35 and 255.37 K.

The prediction of the vapor phase composition is improved by 50% when introducing a temperature-dependency on the binary interaction coefficient, as the average absolute deviation multiplied by 100 is 2.28 for the temperature-independent k_{ij}, 1.15 for the optimal k_{ij} and 1.18 for the model derived one. As it was noted before, in the binary mixture of H_2 – C_1, the prediction of the vapor composition can be more precise with the k_{ij} calculated from the developed model.

Overall, the prediction of the bubble point pressure of the binary mixture of H_2 – C_2 is less successful compared to the binary mixture of H_2 – C_1 as most datasets contain data in a large pressure range, including many points in high pressures, above 300 bar.

As mentioned in the H_2-C_2 mixture, the bubble point pressure is underestimated using the temperature-independent k_{ij} and the prediction is less reliable in the higher pressures.

The exact pressure range that the calculations are deemed not trustworthy depends on each particular dataset, but as a generalization, the prediction deteriorates above 300 bar.

As far as the vapor phase composition is concerned, the molar fraction of H_2 is underestimated with the temperature-independent k_{ij} and the prediction with the temperature-dependent ones is worse at higher pressures.

4.5 H_2 - C_3
The datasets that were used in the development of the model are listed in *Table 31* below.

Table 31: VLE datasets for binary mixture H_2 – C_3

NDP	T (K)	P range (bar)	y range	x range	Reference
13	277.6	34.5 - 551.6	0.810 - 0.936	0.025 - 0.399	Burris et al. 1953 [44]
6	344.3	34.5 - 206.8	0.142 - 0.593	0.012 - 0.319	Burris et al. 1953 40]
3	360.9	68.9 - 103.4	0.235 - 0.278	0.075 - 0.190	Burris et al. 1953 40]
7	173.2	17.2 - 206.8	0.998 - 0.999	0.006 - 0.065	Trust et al. 1971 [45]
4	198.2	34.5 - 206.8	0.993 - 0.996	0.017 - 0.085	Trust et al. 1971 [45]
7	223.2	13.8 - 206.8	0.956 - 0.991	0.008 - 0.108	Trust et al. 1971 [45]
5	248.2	17.2 - 206.8	0.833 - 0.979	0.011 - 0.134	Trust et al. 1971 [45]
7	273.2	20.7 - 206.8	0.725 - 0.933	0.013 - 0.159	Trust et al. 1971 [45]
5	298.2	68.9 - 206.8	0.800 - 0.887	0.060 - 0.195	Trust et al. 1971 [45]
6	323.2	34.5 - 206.8	0.388 - 0.775	0.023 - 0.245	Trust et al. 1971 [45]
5	348.2	51.7 - 155.1	0.259 - 0.522	0.038 - 0.237	Trust et al. 1971 [45]
6	172.1	17.2 - 551.2	0.995 - 0.999	0.006 - 0.143	Williams et al. 1954 [42]
6	199.9	17.2 - 551.2	0.984 - 0.994	0.008 - 0.194	Williams et al. 1954 [42]
6	227.6	17.2 - 551.2	0.940 - 0.985	0.009 - 0.248	Williams et al. 1954 [42]
6	255.4	17.2 - 551.2	0.823 - 0.965	0.011 - 0.319	Williams et al. 1954 [42]
6	283.2	17.2 - 551.2	0.590 - 0.924	0.010 - 0.401	Williams et al. 1954 [42]

All the temperature-dependent k_{ij} values that were obtained through regression, are presented below in *Table 32*. The correlation between the optimal temperature-dependent binary interaction coefficient and the temperature is given in *Equation 35*. It is important to note that, when performing the polynomial regression, some pseudovalues of k_{ij} were added in the low temperatures of 100 and 110 K, by making an extrapolation, to shift the minimum of the equation to low temperatures and ensure the monotonically decreasing trend of the alpha function.

The optimal temperature-independent coefficient was determined to be equal to 0.1643.

The comparison between the calculations in the bubble point pressure and the composition of the vapor phase using the optimal temperature-independent k_{ij}, the optimal temperature-dependent and the calculated k_{ij} values from the correlation, are presented in *Table 32* below.

$$k_{ij}(T) = 5.10890 \cdot 10^{-6}T^2 - 1.03667 \cdot 10^{-3}T + 1.44286 \cdot 10^{-1} \qquad (Eq.\,35)$$
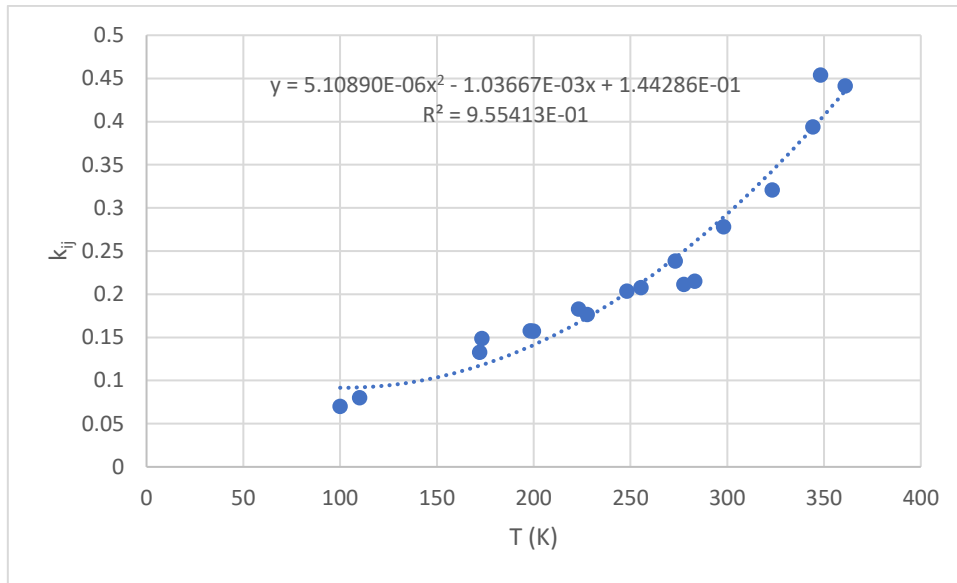
Figure 44: k_{ij} – T plot for binary mixture H_2-C_3

Table 32: Comparison between different binary interaction coefficient values in the VLE prediction of H_2-C_3

T (K)	P range (bar)	k_{ij} T independent			optimal k_{ij} T dependent			k_{ij} trendline		
		value	%AADP	100AADy	value	%AADP	100AADy	value	%AADP	100AADy
172.1	17.2 - 551.2	0.1643	13.0	0.07	0.1327	8.9	0.07	0.1172	9.2	0.07
173.2	17.2 - 206.8	0.1643	5.2	0.01	0.1489	3.2	0.01	0.1180	9.6	0.02
198.2	34.5 - 206.8	0.1643	1.7	0.05	0.1578	1.0	0.06	0.1395	4.7	0.08
199.9	17.2 - 551.2	0.1643	8.3	0.11	0.1572	8.3	0.10	0.1412	9.1	0.07
223.2	13.8 - 206.8	0.1643	3.9	0.53	0.1829	1.7	0.46	0.1674	3.3	0.52
227.6	17.2 - 551.2	0.1643	9.1	0.24	0.1765	8.6	0.21	0.1730	8.6	0.22
248.2	17.2 - 206.8	0.1643	6.8	0.99	0.2036	2.6	1.09	0.2017	2.6	1.08
255.4	17.2 - 551.2	0.1643	9.3	0.89	0.2078	7.5	0.55	0.2128	7.6	0.52
273.2	20.7 - 206.8	0.1643	12.9	1.07	0.2384	4.6	0.45	0.2424	4.6	0.45
277.6	34.5 - 551.6	0.1643	12.4	1.14	0.2113	9.1	0.71	0.2503	9.8	0.60
283.2	17.2 - 551.2	0.1643	10.9	2.52	0.2153	7.3	1.84	0.2604	8.0	1.41
298.2	68.9 - 206.8	0.1643	13.4	2.33	0.2782	3.6	0.46	0.2894	3.8	0.48
323.2	34.5 - 206.8	0.1643	13.6	2.77	0.3208	3.7	1.52	0.3429	3.7	1.93
344.3	34.5 - 206.8	0.1643	15.3	4.53	0.3938	4.9	3.51	0.3930	4.9	3.50
348.2	51.7 - 155.1	0.1643	16.6	4.74	0.4538	6.5	2.96	0.4027	7.1	2.45
360.9	68.9 - 103.4	0.1643	14.5	3.08	0.4412	5.8	3.72	0.4358	5.8	3.64
			10.4	**1.46**		**5.8**	**0.98**		**6.7**	**0.94**

Regarding the results of *Table 32* in the bubble point pressure calculations, the improvement in the prediction is more significant in the higher temperatures, notably in temperatures above 300 K, where it is observed that the deviation is brought down to the

half, or even less. That is because the binary interaction coefficient obtains high values as the temperature increases, and thus the considerable gap between the value obtained from the temperature-independent fitting and the optimal one (0.1643 and above 0.4), leads to poor predictions. Overall, the average deviation with the temperature-independent k_{ij} value is 10.4% and with the optimal and calculated k_{ij}, 5.8% and 6.7% respectively. The latter percentages are low due to the lack of high-pressure data points in the datasets examined which allows the prediction to be more precise.

For the binary mixture of H_2 and C_3 the absolute deviation in the composition of the vapor phase is comparable for all three k_{ij} values examined, and the average prediction of the model developed is optimal, although in most isothermal curves, nearly identical to the prediction with the optimal k_{ij}. The average absolute deviations multiplied by 100 for the three k_{ij} values are 1.46, 0.98 and 0.94.

4.6 H_2 – nC_4
The datasets that were used in the development of the model are listed in *Table 33* below.

Table 33: VLE datasets for binary mixture H_2 – nC_4

NDP	T (K)	P range (bar)	y range	x range	Reference
5	297.0	22.4 - 523.3	0.869 - 0.975	0.019 - 0.341	Aroyan et al. 1951 [46]
5	277.6	21.4 - 541.2	0.000 - 0.984	0.016 - 0.302	Aroyan et al. 1951 [46]
8	260.9	21.1 - 534.3	0.958 - 0.990	0.017 - 0.274	Aroyan et al. 1951 [46]
5	244.3	21.7 - 513.7	0.979 - 0.995	0.015 - 0.229	Aroyan et al. 1951 [46]
5	227.6	27.6 - 441.3	0.992 - 0.997	0.017 - 0.180	Aroyan et al. 1951 [46]
6	199.8	23.2 - 482.6	0.990 - 0.999	0.013 - 0.149	Aroyan et al. 1951 [46]
7	172.0	20.7 - 508.8	-	0.008 - 0.116	Aroyan et al. 1951 [46]
5	144.3	37.6 - 493.0	-	0.010 - 0.067	Aroyan et al. 1951 [46]
13	327.7	31.6 - 168.5	0.777 - 0.932	0.025 - 0.160	Klink et al. 1975 [47]
12	344.3	27.8 - 166.5	0.638 - 0.894	0.022 - 0.173	Klink et al. 1975 [47]
11	361.0	27.9 - 167.9	0.483 - 0.843	0.021 - 0.193	Klink et al. 1975 [47]
12	377.6	28.3 - 167.4	0.322 - 0.760	0.019 - 0.217	Klink et al. 1975 [47]
12	394.3	34.3 - 168.8	0.213 - 0.638	0.021 - 0.266	Klink et al. 1975 [47]
2	355.4	43.2 - -94.8	0.627 - 0.833	0.040 - 0.099	Nelson et al. 1943 [48]
2	388.7	49.5 - -93.0	0.420 - 0.624	0.051 - 0.111	Nelson et al. 1943 [48]

All the temperature-dependent k_{ij} values that were obtained through regression, are presented below in *Table 34*. The correlation between the optimal temperature-dependent binary interaction coefficient and the temperature is given in *Equation 36.* When performing the polynomial regression, some pseudovalues of k_{ij} were added in the low temperatures of 90 and 100 K, by making an extrapolation. Otherwise, the trendline would lead to a minimum at 180 K and to higher values at lower temperatures, and therefore the alpha function would not be monotonically decreasing.

The optimal temperature-independent coefficient was determined to be equal to 0.1600.

The comparison between the calculations in the bubble point pressure and the composition of the vapor phase using the optimal temperature-independent k_{ij}, the optimal temperature-dependent and the calculated k_{ij} values from the correlation, are presented in *Table 34* below.

$$k_{ij}(T) = 5.93859 \cdot 10^{-6}T^2 - 1.38650 \cdot 10^{-3}T + 1.46798 \cdot 10^{-1} \qquad (Eq.\,36)$$
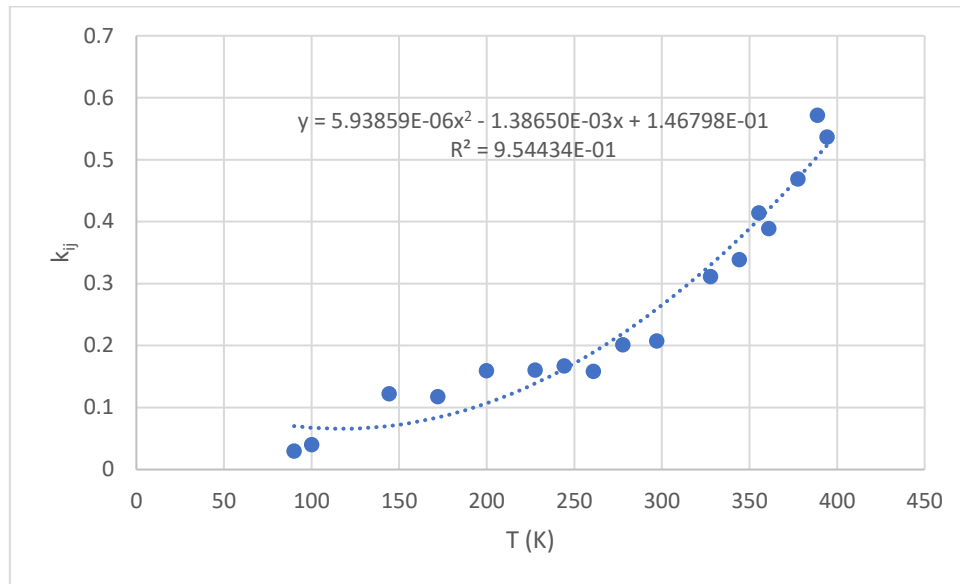
Figure 45: kij – T plot for binary mixture H_2-C_4

Table 34: Comparison between different binary interaction coefficient values in the VLE prediction of H_2-nC_4

T (K)	P range (bar)	k_{ij} T independent			optimal k_{ij} T dependent			k_{ij} trendline		
		value	%AADP	100AADy	value	%AADP	100AADy	value	%AADP	100AADy
144.3	37.6 - 493.0	0.1600	20.8	0.00	0.1220	5.3	0.00	0.0704	21.1	0.00
172.0	20.7 - 508.8	0.1600	14.7	0.01	0.1177	10.4	0.02	0.0841	16.5	0.02
199.8	23.2 - 482.6	0.1600	6.6	0.24	0.1592	6.6	0.23	0.1069	13.4	0.23
227.6	27.6 - 441.3	0.1600	3.4	0.15	0.1605	3.4	0.15	0.1389	5.5	0.14
244.3	21.7 - 513.7	0.1600	4.8	0.20	0.1671	4.6	0.21	0.1625	4.7	0.21
260.9	21.1 - 534.3	0.1600	3.6	0.22	0.1582	3.5	0.22	0.1894	7.2	0.23
277.6	21.4 - 541.2	0.1600	9.0	0.65	0.2012	5.4	0.52	0.2196	6.4	0.49
297.0	22.4 - 523.3	0.1600	8.8	0.68	0.2074	6.2	0.58	0.2591	8.2	0.47
327.7	31.6 - 168.5	0.1600	15.4	1.87	0.3114	4.2	0.34	0.3302	4.6	0.39
344.3	27.8 - 166.5	0.1600	15.4	2.95	0.3388	3.1	0.57	0.3734	4.1	0.62
355.4	43.2 - 94.8	0.1600	16.6	2.74	0.4141	0.6	2.88	0.4042	0.8	2.86
361.0	27.9 - 167.9	0.1600	16.4	4.11	0.3887	2.7	0.76	0.4202	3.1	0.90
377.6	28.3 - 167.4	0.1600	17.5	5.14	0.4687	3.7	1.66	0.4700	3.7	1.67
388.7	49.5 - 93.0	0.1600	16.5	5.66	0.5719	2.4	2.22	0.5054	3.0	1.14
394.3	34.3 - 168.8	0.1600	17.7	4.74	0.5234	4.2	3.85	0.5234	4.2	3.54
			13.3	**2.29**		**4.5**	**0.97**		**6.6**	**0.93**

The average deviation in the calculation of the bubble point pressure is nearly three times lower when using the optimal k_{ij} values than when using the temperature-independent k_{ij}, namely 4.5% and 13.3%. This big gap is explained by the fact that k_{ij} optimal values occupy a wide range, starting from 0.12 to 0.52 as the temperature increases, and thus the temperature-independent k_{ij} value that is at 0.16 is very low and can only accurately predict the bubble point pressure at low temperatures. The average deviation using the model is 6.6%, considerably higher than the deviation the optimal k_{ij} calculations yield. That is linked to the introduction of the pseudovalues of the binary interaction coefficient in the extrapolated low temperatures. More specifically, the pseudovalues force the trendline to extrapolate to low values of the coefficient and thus the actual plotted values in the temperature range of 140-200 K are significantly greater than the ones predicted from the trendline. That is why the deviation in the isothermal curves of 144.26, 172.04 and 199.82 K is above 10% for the calculations made from the derived trendline. The rest of the deviations in the other isothermal curves are closer to the deviations occurred with the optimal k_{ij} coefficients.

Similarly to the binary mixture of $H_2 - C_3$, the absolute average deviation in the prediction of the vapor phase composition is slightly better when using the derived model. All the calculations, however, have low discrepancies from the experimental data. The average absolute deviations multiplied by 100 for the three k_{ij} values are 2.29, 0.97 and 0.93.

4.7 $H_2 - nC_5$
The datasets that were used in the development of the model are listed in *Table 35* below.

Table 35: VLE datasets for binary mixture $H_2 - nC_5$

NDP	T (K)	P range (bar)	y range	x range	Reference
4	308.2	35.1 - 136.2	-	0.026 - 0.096	Connolly et al. 1986 [49]
4	313.2	34.2 - 132.0	-	0.026 - 0.096	Connolly et al. 1986 [49]
4	323.2	32.7 - 124.3	-	0.026 - 0.096	Connolly et al. 1986 [49]
4	333.2	31.4 - 117.1	-	0.026 - 0.096	Connolly et al. 1986 [49]
5	343.2	30.3 - 140.9	-	0.026 - 0.120	Connolly et al. 1986 [49]
5	353.2	29.5 - 132.6	-	0.026 - 0.120	Connolly et al. 1986 [49]
5	363.2	28.9 - 125.5	-	0.026 - 0.120	Connolly et al. 1986 [49]
5	373.2	28.6 - 118.7	-	0.026 - 0.120	Connolly et al. 1986 [49]
5	383.2	28.6 - 112.6	-	0.026 - 0.120	Connolly et al. 1986 [49]
5	393.2	28.9 - 106.9	-	0.026 - 0.120	Connolly et al. 1986 [49]
5	403.2	29.4 - 101.8	-	0.026 - 0.120	Connolly et al. 1986 [49]
5	413.2	30.4 - 96.7	-	0.026 - 0.120	Connolly et al. 1986 [49]
5	423.2	31.5 - 92.0	-	0.026 - 0.120	Connolly et al. 1986 [49]
5	433.2	33.1 - 87.4	-	0.026 - 0.120	Connolly et al. 1986 [49]
5	443.2	34.9 - 82.7	-	0.026 - 0.120	Connolly et al. 1986 [49]
9	273.2	10.3 - 275.8	0.967 - 0.997	0.006 - 0.161	Freitag et al. 1986 [50]
12	323.2	3.5 - 275.9	0.512 - 0.982	0.002 - 0.196	Freitag et al. 1986 [50]

9	373.2	10.4 - 275.9	0.373 - 0.942	0.005 - 0.259	Freitag et al. 1986 [50]				

By fitting each individual isothermal curve and plotting each temperature-dependent k_{ij} that was obtained, as shown in *Figure 46* below, the correlation of *Equation 37* was derived.

$$k_{ij}(T) = 1.26012 \cdot 10^{-5}T^2 - 6.36088 \cdot 10^{-3}T + 1.07977 \qquad (Eq.37)$$
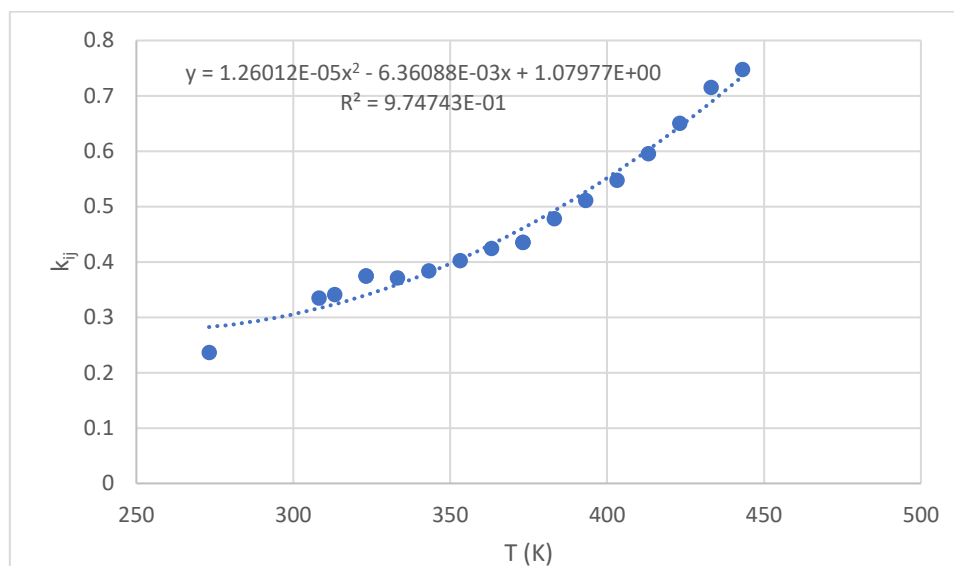
Figure 46: kij – T plot for binary mixture H_2-nC_5

By fitting all datasets that were used in the k_{ij} – T correlation, up to 700 bar, a temperature-independent value for k_{ij} equal to 0.3469 was obtained.

The comparison between all calculations with the different values for the binary interaction coefficient is displayed in *Table 36*.

Table 36: Comparison between different binary interaction coefficient values in the VLE prediction of H_2-nC_5

T (K)	P range (bar)	k_{ij} T independent			optimal k_{ij} T dependent			k_{ij} trendline		
		value	AADP	100AADy	value	AADP	100AADy	value	AADP	100AADy
273.2	10.3 - 275.8	0.3469	18.9	0.18	0.2363	4.6	0.10	0.2824	7.4	0.11
308.2	35.1 - 136.2	0.3469	1.7	-	0.3347	1.1	-	0.3161	2.5	-
313.2	34.2 - 132.0	0.3469	1.2	-	0.3408	1.0	-	0.3235	2.2	-
323.2	3.5 - 275.9	0.3469	4.9	0.25	0.3742	3.9	0.26	0.3400	5.4	0.27
333.2	31.4 - 117.1	0.3469	2.6	-	0.3707	0.9	-	0.3591	1.4	-
343.2	30.3 - 140.9	0.3469	3.9	-	0.3836	1.1	-	0.3807	1.1	-
353.2	29.5 - 132.6	0.3469	5.3	-	0.4023	1.1	-	0.4048	1.1	-
363.2	28.9 - 125.5	0.3469	6.7	-	0.4243	1.1	-	0.4315	1.1	-
373.2	10.4 - 275.9	0.3469	8.5	1.59	0.4349	4.2	1.04	0.4606	4.2	0.97
383.2	28.6 - 112.6	0.3469	9.2	-	0.4778	1.1	-	0.4923	1.3	-
393.2	28.9 - 106.9	0.3469	10.3	-	0.5111	1.1	-	0.5265	1.3	-

403.2	29.4 - 101.8	0.3469	11.1	-	0.5474	0.8	-	0.5633	1.2	-
413.2	30.4 - 96.7	0.3469	12.0	-	0.5955	1.2	-	0.6025	1.2	-
423.2	31.5 - 92.0	0.3469	12.6	-	0.6499	1.3	-	0.6443	1.3	-
433.2	33.1 - 87.4	0.3469	12.9	-	0.7149	1.4	-	0.6886	1.7	-
443.2	34.9 - 82.7	0.3469	10.4	-	0.7474	1.9	-	0.7354	2.4	-
			8.7	0.63		2.5	0.45		3.0	0.43

Regarding the bubble point pressure calculations, it is notable that using the temperature-dependent k_{ij} value, there is a significant improvement in the prediction, as the average deviation is brought down to 2.5% from 8.7%. The big gap between the average deviations is attributed to the wider range of optimal k_{ij} values obtained that cannot be represented with a single k_{ij} value, similarly to the binary mixture $H_2 – nC_4$. The prediction with the calculated k_{ij} values is relatively close in terms of precision to the temperature-dependent fitted values, as the average deviation is 3.0%. The deviation can be attributed to the fact that, as it is shown in *Figure 46*, the plotted points of the temperature-dependent k_{ij} values do not fully align with the trendline derived. Many of the isothermal curves, however, are predicted with equal accuracy.

The prediction of the vapor phase composition is highly accurate with all three k_{ij} values. That is attributed to the high asymmetry of the mixture, as the vapor phase mainly consists of of H_2, the much lighter molecule. More specifically, the average absolute deviation from the experimental data multiplied by 100 is merely 0.63 for the temperature-independent k_{ij} and 0.45 and 0.43 for the temperature-dependent ones.

4.8 $H_2 – nC_6$

The datasets that were used in the development of the model are listed in *Table 37* below.

Table 37: VLE datasets for binary mixture $H_2 – nC_6$

NDP	T(K)	P range (bar)	y range	x range	Reference
10	298.2	15.3 - 91.9	-	0.01076 - 0.06117	Brunner et al. 1985 [51]
7	323.2	13.8 - 88.2	-	0.01075 - 0.06757	Brunner et al. 1985 [51]
12	344.3	12.4 - 87.0	-	0.01050 - 0.07270	Gao et al. 2001 [52]
7	373.2	20.5 - 98.1	-	0.01909 - 0.09388	Brunner et al. 1985 [51]
11	377.6	13.8 - 151.1	-	0.01220 - 0.14300	Gao et al. 2001 [52]
11	410.9	19.7 - 110.8	-	0.01790 - 0.12040	Gao et al. 2001 [52]

By fitting each individual isothermal curve and plotting each temperature-dependent k_{ij} that was obtained, as shown in *Figure 47* below, the correlation of *Equation* 38 was derived.

$$k_{ij}(T) = 1.18615 \cdot 10^{-5}T^2 - 6.64229 \cdot 10^{-3}T + 1.25135 \qquad (Eq. 38)$$

Figure 47: k_{ij} – T plot for binary mixture H_2-nC_6

By fitting all datasets that were used in the k_{ij} – T correlation, up to 700 bar, a temperature-independent value for k_{ij} equal to 0.3737 was obtained.

The comparison between all calculations with the different values for the binary interaction coefficient is displayed in *Table 38*.

Table 38: Comparison between different binary interaction coefficient values in the VLE prediction of H_2-nC_6

		k_{ij} T independent			optimal k_{ij} T dependent			k_{ij} trendline		
T(K)	P range (bar)	value	AADP	100AADy	value	AADP	100AADy	value	AADP	100AADy
298.2	15.3 - 91.9	0.3737	7.0	-	0.3212	1.0	-	0.3252	1.1	-
323.2	13.8 - 88.2	0.3737	3.0	-	0.3438	1.4	-	0.3434	1.4	-
344.3	12.4 - 87.0	0.3737	1.7	-	0.3870	1.2	-	0.3703	1.9	-
373.2	20.5 - 98.1	0.3737	3.9	-	0.4194	1.3	-	0.4242	1.4	-
377.6	13.8 - 151.1	0.3737	4.1	-	0.4204	0.6	-	0.4342	1.2	-
410.9	19.7 - 110.8	0.3737	10.1	-	0.5311	1.1	-	0.5245	1.1	-
			5.1	**-**		**1.1**	**-**		**1.4**	**-**

The introduction of a temperature-dependent k_{ij} significantly improves the prediction of the bubble point pressure of the binary mixture of H_2 – nC_6. The average deviation is brought down from 5.1% to 1.1% for the optimal temperature-dependent k_{ij} values and 1.4% for a temperature-dependent, calculated from the trendline, value.

It can be noted that the prediction of the bubble point pressure derived from the model is very approximate to the results obtained from the optimal fittings. That is attributed to the excellent aggreement between the optimal temperature-dependent k_{ij} values and the trendline, owed to the smaller number of datasets used in the fittings and, the shorter pressure ranges of the datasets. These factors allow the polynomial regression of the k_{ij}

values to be performed with a high coefficient of determination R^2, and thus the model is accurate.

Regarding the temperature range studied, there does not seem to be a correlation between the temperature and the improvement achieved by introducing the temperature-dependent k_{ij}.

No experimental values for the vapor phase composition is available in the datasets examined and thus no comparison is made with experimental data.

4.9 H$_2$ – nC$_8$

The datasets that were used in the development of the model are listed in *Table 39* below.

Table 39: VLE datasets for binary mixture H$_2$ – nC$_8$

NDP	T (K)	P range (bar)	y range	x range	Reference
3	295.0	104.4 - 173.3	-	0.066 - 0.106	Peramanu et al. 1997 [53]
4	298.2	28.9 - 147.7	-	0.020 - 0.091	Brunner et al. 1985 [51]
4	323.2	24.0 - 143.7	-	0.019 - 0.102	Brunner et al. 1985 [51]
4	373.2	30.5 - 152.7	-	0.029 - 0.137	Brunner et al. 1985 [51]
5	463.2	10.1 - 63.6	0.495 - 0.900	0.009 - 0.087	Connolly et al. 1989 [54]
5	473.2	12.4 - 83.0	0.495 - 0.900	0.012 - 0.118	Connolly et al. 1989 [54]
5	483.2	15.3 - 110.0	0.495 - 0.900	0.015 - 0.162	Connolly et al. 1989 [54]
7	493.2	10.8 - 150.4	0.211 - 0.900	0.005 - 0.225	Connolly et al. 1989 [54]
6	503.2	12.9 - 125.3	0.211 - 0.863	0.007 - 0.201	Connolly et al. 1989 [54]
6	513.2	14.3 - 92.4	0.164 - 0.796	0.007 - 0.158	Connolly et al. 1989 [54]
5	523.2	18.5 - 125.5	0.211 - 0.796	0.013 - 0.226	Connolly et al. 1989 [54]

By fitting each individual isothermal curve and plotting each temperature-dependent k_{ij} that was obtained, as shown in *Figure 48* below, the correlation of *Equation 39* was derived. It is important to note that, when performing the polynomial regression, some pseudovalues of k_{ij} were added in the low temperatures of 230 and 280K, by making an extrapolation to maintain the monotonically decreasing trend of the alpha function.

$$k_{ij}(T) = 6.61124 \cdot 10^{-6}T^2 - 3.14536 \cdot 10^{-3}T + 6.47121 \cdot 10^{-1} \qquad (Eq.\,39)$$

Figure 48: kij – T plot for binary mixture H_2-nC_8

By fitting all datasets that were used in the k_{ij} – T correlation, up to 700 bar, a temperature-independent value for k_{ij} equal to 0.3877 was obtained.

The comparison between all calculations with the different values for the binary interaction coefficient is displayed in *Table 40*.

Table 40: Comparison between different binary interaction coefficient values in the VLE prediction of H_2-nC_8

| T (K) | P range (bar) | k_{ij} T independent | | | optimal k_{ij} T dependent | | | k_{ij} trendline | | |
		value	AADP	100AADy	value	AADP	100AADy	value	AADP	100AADy
295.0	104.4 - 173.3	0.3877	12.5	-	0.3087	1.8	-	0.2946	2.2	-
298.2	28.9 - 147.7	0.3877	5.9	-	0.3482	0.9	-	0.2970	6.5	-
323.2	24.0 - 143.7	0.3877	5.3	-	0.3441	1.1	-	0.3211	2.9	-
373.2	30.5 - 152.7	0.3877	3.1	-	0.3787	2.7	-	0.3940	3.4	-
463.2	10.1 - 63.6	0.3877	8.9	1.86	0.5918	0.8	0.35	0.6085	1.0	0.48
473.2	12.4 - 83.0	0.3877	9.8	2.10	0.6160	1.0	0.45	0.6390	1.1	0.57
483.2	15.3 - 110.0	0.3877	10.9	2.32	0.6396	1.5	0.62	0.6707	1.7	0.80
493.2	10.8 - 150.4	0.3877	10.1	2.80	0.6541	2.3	0.99	0.7038	2.3	1.02
503.2	12.9 - 125.3	0.3877	10.5	3.34	0.7234	2.0	1.18	0.7382	2.0	1.21
513.2	14.3 - 92.4	0.3877	9.7	3.92	0.8252	1.6	1.25	0.7740	2.0	1.29
523.2	18.5 - 125.5	0.3877	12.1	4.39	0.8635	3.2	2.07	0.8110	3.4	2.01
			9.2	**2.99**		**1.8**	**1.00**		**2.5**	**1.06**

A visualized comparison between the different sets of calculations is shown below in *Figure 49*.
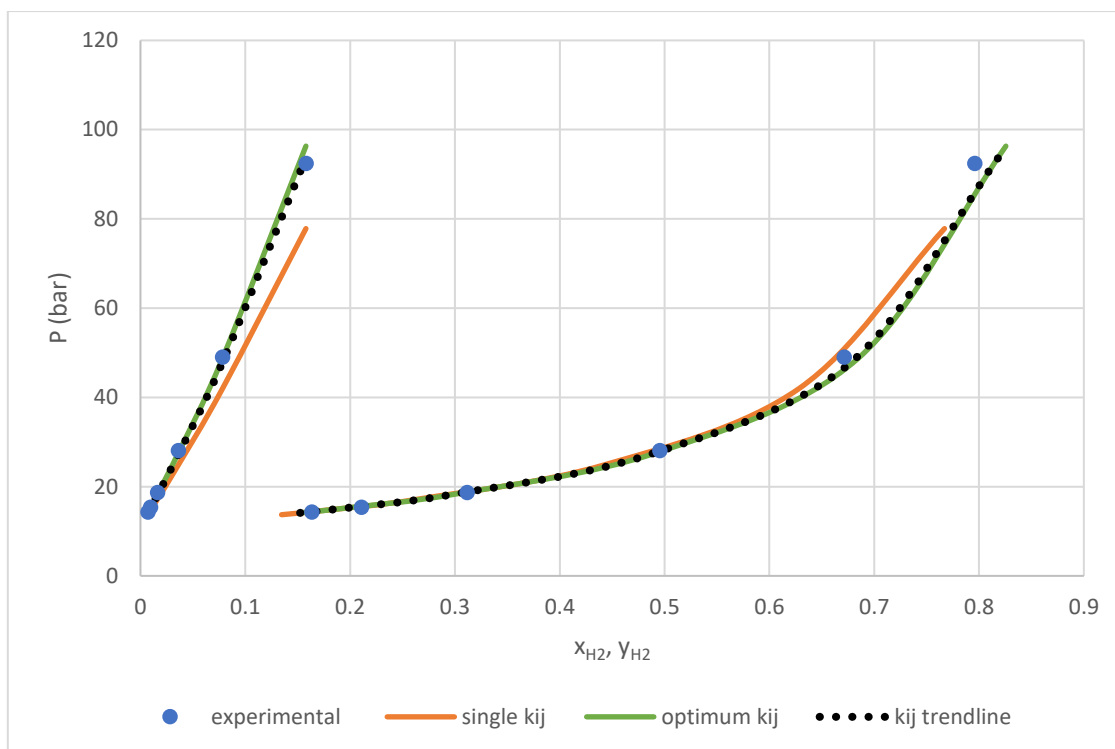
Figure 49: VLE envelope for $H_2 – nC_8$ in T=513.15K

The prediction of the bubble point pressure with the optimal k_{ij} values is much more accurate compared to the single, temperature-independent k_{ij} value, as the average deviation is brought down to 1.8% from 9.2%. The largest improvements are noticeable in temperatures above 460 K, as the optimal k_{ij} values in this temperature range are greater than the single k_{ij} obtained. The model derived yields an average deviation of 2.5% the larger discrepancy noted in the isothermal curve of 298.15, which is attributed to the high deviation between the trendline and the corresponding plotted k_{ij} value. The presence of pseudovalues lowers the value of the coefficient of determination and alters the trendline in a way that that it does not fully align with the plotted values. That leads to a more significant deviation between the calculated k_{ij} values and the optimal ones, making the gap between the average deviation of the optimal calculations and the model calclations larger.

Regarding the vapor phase composition prediction, the introduction of the temperature dependency halves the deviation from the experimental data in all isothermal curves examined. The results of the calculations with the derived model closely follow the calculations performed with the optimal k_{ij} values.

4.10 $H_2 – nC_{10}$
The datasets that were used in the development of the model are listed in *Table 41* below.

Table 41: VLE datasets for binary mixture $H_2 – nC_{10}$

NDP	T (K)	P range (bar)	y range	x range	Reference
3	293.2	23.7 - 103.5	-	0.016 - 0.067	Brunner et al. 1985 [51]

4	308.2	36.6 - 161.8	-	0.026 - 0.104	Connolly et al. 1986 [49]
2	323.2	33.7 - 148.3	-	0.026 - 0.104	Connolly et al. 1986 [49]
3	323.2	28.2 - 94.2	-	0.022 - 0.070	Brunner et al. 1985 [51]
5	343.2	30.4 - 167.5	-	0.026 - 0.127	Connolly et al. 1986 [49]
6	344.3	44.6 - 173.9	-	0.037 - 0.129	Park et al. 1995 [55]
3	373.2	20.4 - 94.0	-	0.020 - 0.088	Brunner et al. 1985 [51]
6	383.2	25.1 - 163.4	-	0.026 - 0.148	Connolly et al. 1986 [49]
6	413.2	22.2 - 141.9	-	0.026 - 0.148	Connolly et al. 1986 [49]
6	433.2	20.6 - 129.5	-	0.026 - 0.148	Connolly et al. 1986 [49]
6	453.2	19.4 - 118.4	-	0.026 - 0.148	Connolly et al. 1986 [49]
6	473.2	18.5 - 108.5	-	0.026 - 0.148	Connolly et al. 1986 [49]
6	493.2	17.9 - 99.4	-	0.026 - 0.148	Connolly et al. 1986 [49]
6	503.0	14.8 - 101.0	-	0.018 - 0.151	Schofield et al. 1992 [56]
6	513.2	17.8 - 91.2	-	0.026 - 0.148	Connolly et al. 1986 [49]
6	523.2	18.0 - 87.3	-	0.026 - 0.148	Connolly et al. 1986 [49]
6	533.2	18.2 - 83.6	-	0.026 - 0.148	Connolly et al. 1986 [49]
6	543.2	18.6 - 80.0	-	0.026 - 0.148	Connolly et al. 1986 [49]
6	553.2	19.1 - 76.5	-	0.026 - 0.148	Connolly et al. 1986 [49]
6	563.2	19.7 - 73.1	-	0.026 - 0.148	Connolly et al. 1986 [49]
6	573.2	20.6 - 69.6	-	0.026 - 0.148	Connolly et al. 1986 [49]

By fitting each individual isothermal curve and plotting each temperature-dependent k_{ij} that was obtained, as shown in *Figure 50* below, the correlation of *Equation 40* was derived. It is important to note that, when performing the polynomial regression, pseudovalues of k_{ij} were added in the low temperatures of 200 and 220 K.

$$k_{ij}(T) = 7.27190 \cdot 10^{-6}T^2 - 4.17350 \cdot 10^{-3}T + 9.03628 \cdot 10^{-1} \qquad (Eq.\,40)$$
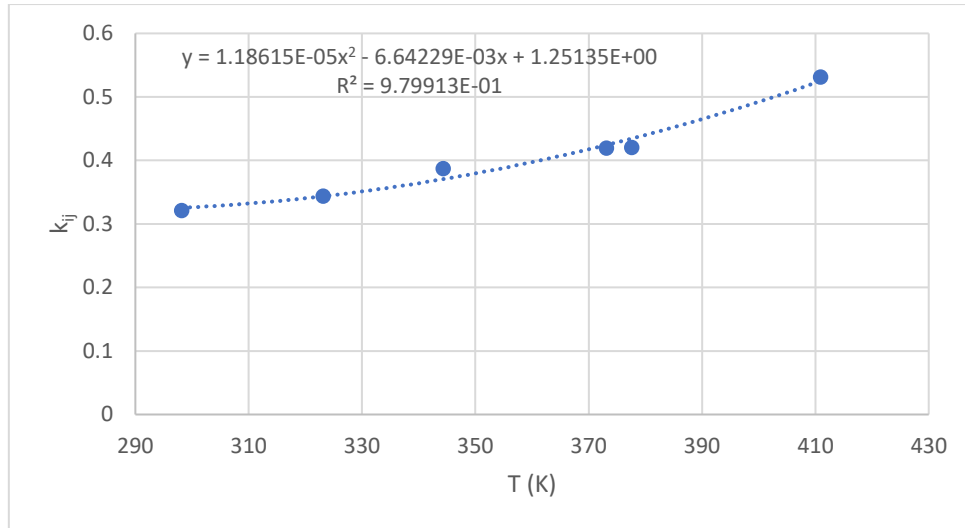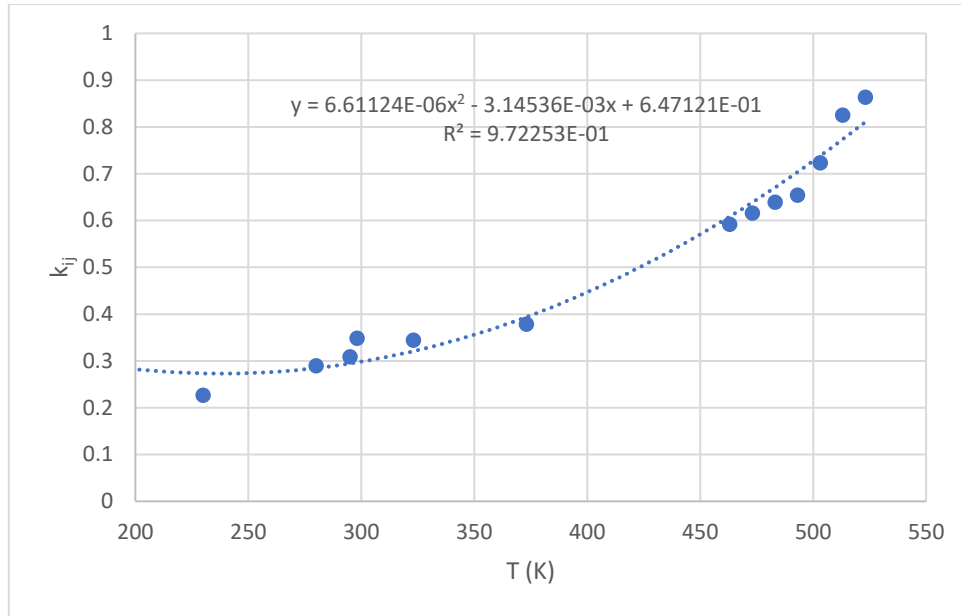

Figure 50: kij – T plot for binary mixture H_2-nC_{10}

By fitting all datasets that were used in the k_{ij} – T correlation, up to 700 bar, a temperature-independent value for k_{ij} equal to 0.3965 was obtained.

The comparison between all calculations with the different values for the binary interaction coefficient is displayed in *Table 42*.

Table 42: Comparison between different binary interaction coefficient values in the VLE prediction of H_2-nC_{10}

T (K)	P range (bar)	k_{ij} T independent			optimal k_{ij} T dependent			k_{ij} trendline		
		value	AADP	100AADy	value	AADP	100AADy	value	AADP	100AADy
293.2	23.7 - 103.5	0.3965	5.4	-	0.3552	2.7	-	0.3051	6.6	-
308.2	36.6 - 161.8	0.3965	4.1	-	0.3648	1.3	-	0.3081	7.2	-
323.2	28.2 - 148.3	0.3965	4.7	-	0.4222	1.5	-	0.3143	5.0	-
343.2	30.4 - 167.5	0.3965	3.3	-	0.3709	1.0	-	0.3278	4.3	-
344.3	44.6 - 173.9	0.3965	1.1	-	0.3893	1.0	-	0.3287	6.6	-
373.2	20.4 - 94.0	0.3965	2.6	-	0.3680	0.8	-	0.3588	1.0	-
383.2	25.1 - 163.4	0.3965	1.3	-	0.3819	0.8	-	0.3721	1.1	-
413.2	22.2 - 141.9	0.3965	0.9	-	0.4073	0.6	-	0.4206	1.0	-
433.2	20.6 - 129.5	0.3965	2.6	-	0.4313	0.6	-	0.4602	2.1	-
453.2	19.4 - 118.4	0.3965	4.4	-	0.4627	0.7	-	0.5057	2.9	-
473.2	18.5 - 108.5	0.3965	6.3	-	0.5042	0.6	-	0.5569	3.2	-
493.2	17.9 - 99.4	0.3965	8.2	-	0.5569	0.7	-	0.6140	3.0	-
503.0	14.8 - 101.0	0.3965	9.3	-	0.5917	4.0	-	0.6442	5.1	-
513.2	17.8 - 91.2	0.3965	10.1	-	0.6271	0.9	-	0.6769	2.2	-
523.2	18.0 - 87.3	0.3965	11.1	-	0.6701	0.9	-	0.7105	1.7	-
533.2	18.2 - 83.6	0.3965	12.0	-	0.7201	1.0	-	0.7456	1.2	-
543.2	18.6 - 80.0	0.3965	12.8	-	0.7770	1.1	-	0.7821	1.1	-
553.2	19.1 - 76.5	0.3965	13.5	-	0.8446	1.2	-	0.8201	1.4	-
563.2	19.7 - 73.1	0.3965	14.1	-	0.9195	1.3	-	0.8595	2.1	-
573.2	20.6 - 69.6	0.3965	14.7	-	1.0111	1.6	-	0.9004	3.4	-
			7.4			**1.2**			**3.0**	

The accuracy of the prediction of the bubble point pressure is significantly improved when applying a temperature dependency on the calculations, as the average deviation using the optimal k_{ij} is brought down to 1.2% from 7.4%. The largest improvements are noted in the higher temperatures, above 470K, as in this temperature range the optimal k_{ij} values are substantially greater than the single k_{ij} obtained. An important improvement is also achieved with the calculations from the derived model, with an average deviation of 3.0%, although the calculations are not highly accurate in the lowest temperature range of 293.15 – 344.30 K. This is attributed to the fact that pseudovalues in low temperatures were added, and thus the trendline was altered, with a more direct effect on this low temperature range, as it is evident on *Figure 50* above. The shifting of the trendline to

include the extrapolated points leads to a general deviation between the the optimal k_{ij} values and the calculated ones, impacting the accuracy of the calculations.

No experimental data regarding the vapor phase composition was available in the datasets examined and therefore no comments on the accuracy of the calculations can be made.

4.11 Binary interaction coefficient correlation with carbon number

Having examined the binary mixtures of hydrogen with hydrocarbons with carbon number up to 10, it is of special interest to investigate the correlation between the binary interaction coefficient and the carbon number. The goal of this correlation is to propose suitable k_{ij} values for mixtures of hydrogen with hydrocarbons with a carbon number up to 10. The correlation is derived from the temperature-independent k_{ij} values obtained and it is shown in *Figure 51* below. From the figure it can be observed that the plotted temperature-independent k_{ij} values approximate a constant value of 0.4 and therefore this value is proposed for use in hydrogen – hydrocarbon binary mixtures with a carbon number higher than 10.
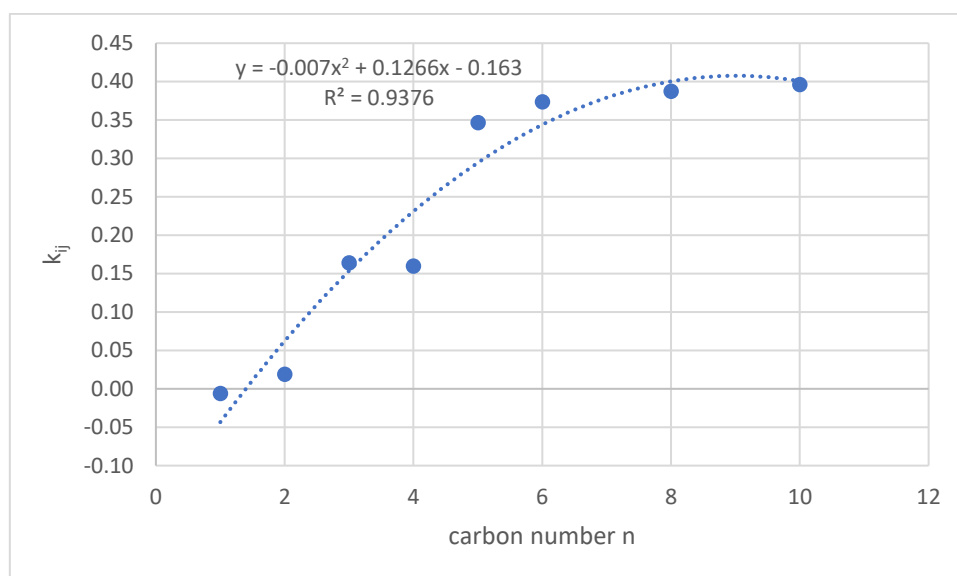
Figure 51: Binary interaction coefficient correlation with carbon number

4.12 H$_2$ - CO$_2$

The datasets that were used in the development of the model are listed in *Table 43* below.

Table 43: VLE datasets for binary mixture H$_2$ – CO$_2$

NDP	T (K)	P range (bar)	y range	x range	Reference
8	259.9	32.7 - 203.2	0.206 - 0.745	0.005 - 0.093	Spano et al. 1968 [57]
6	289.9	65.8 - 175.3	0.102 - 0.422	0.013 - 0.139	Spano et al. 1968 [57]
8	229.9	25.8 - 203.0	0.614 - 0.905	0.006 - 0.059	Spano et al. 1968 [57]
9	244.9	20.8 - 203.2	0.523 - 0.841	0.003 - 0.073	Spano et al. 1968 [57]

7	274.9	49.9 - 200.6	0.180 - 0.518	0.010 - 0.115	Spano et al. 1968 [57]
3	239.7	185.8 - 192.7	0.871 - 0.910	0.062 - 0.071	Augood et al. 1957 [58]
3	293.2	96.4 - 195.0	0.213 - 0.321	0.044 - 0.179	Kaminishi et al. 1966 [59]
3	283.2	96.4 - 195.1	0.439 - 0.469	0.044 - 0.134	Kaminishi et al. 1966 [59]
5	273.2	50.8 - 195.1	0.212 - 0.606	0.011 - 0.118	Kaminishi et al. 1966 [59]
4	253.2	52.7 - 200.0	0.522 - 0.775	0.016 - 0.084	Kaminishi et al. 1966 [59]
4	233.2	52.7 - 200.0	0.746 - 0.875	0.014 - 0.061	Kaminishi et al. 1966 [59]
12	218.2	5.6 - 149.6	0.000 - 0.926	0.000 - 0.036	Fandino et al. 2015 [60]
11	243.2	14.3 - 149.5	0.000 - 0.818	0.000 - 0.053	Fandino et al. 2015 [60]
10	258.1	22.9 - 154.4	0.000 - 0.715	0.000 - 0.068	Fandino et al. 2015 [60]
10	273.2	34.9 - 148.7	0.000 - 0.560	0.000 - 0.086	Fandino et al. 2015 [60]
9	280.7	42.3 - 149.7	0.000 - 0.471	0.000 - 0.090	Fandino et al. 2015 [60]
9	288.2	50.9 - 150.9	0.000 - 0.366	0.000 - 0.103	Fandino et al. 2015 [60]

By fitting each individual isothermal curve and plotting each temperature-dependent k_{ij} that was obtained, as shown in *Figure 52* below, the correlation of *Equation 41* was derived.

$$k_{ij}(T) = 1.6397 \cdot 10^{-5} T^2 - 6.20316 \cdot 10^{-3} T + 7.32613 \cdot 10^{-1} \qquad (Eq.41)$$
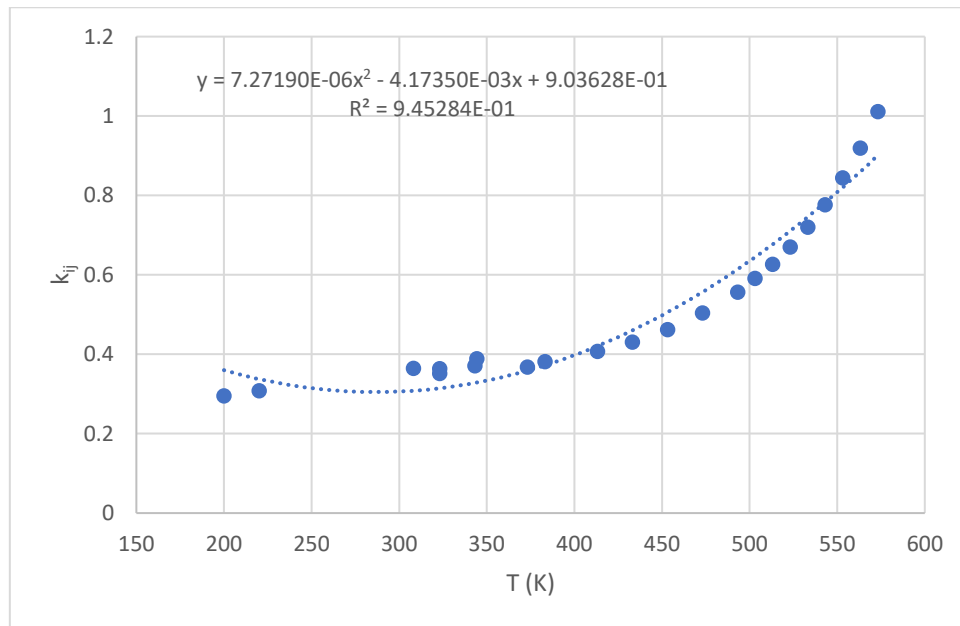

Figure 52: k_{ij} – T plot for binary mixture H_2-CO_2

By fitting all datasets that were used in the k_{ij} – T correlation, up to 700 bar, a temperature-independent value for k_{ij} equal to 0.1846 was obtained.

The comparison between all calculations with the different values for the binary interaction coefficient is displayed in *Table 44*.

Table 44: Comparison between different binary interaction coefficient values in the VLE prediction of H_2-CO_2

T (K)	P range (bar)	k_{ij} T independent			optimal k_{ij} T dependent			k_{ij} trendline		
		value	AADP	100AADy	value	AADP	100AADy	value	AADP	100AADy
218.2	5.6 - 149.6	0.1846	4.5	0.61	0.1641	2.8	0.57	0.1580	3.1	0.68
219.9	10.8 - 198.3	0.1846	6.0	0.45	0.1598	2.2	0.93	0.1598	2.2	0.74
229.9	25.8 - 203.0	0.1846	4.2	0.36	0.1626	2.0	0.97	0.1720	2.6	0.71
233.2	10.1 - 200.0	0.1846	2.1	0.45	0.1838	2.1	0.43	0.1766	2.4	0.28
239.7	185.8 - 192.7	0.1846	5.2	2.97	0.1846	5.2	2.97	0.1870	5.8	2.91
243.2	14.3 - 149.5	0.1846	2.9	0.41	0.2018	2.0	0.62	0.1931	2.2	0.44
244.9	20.8 - 203.2	0.1846	1.3	0.90	0.1914	0.7	0.80	0.1963	1.0	0.72
253.2	52.7 - 200.0	0.1846	4.6	0.68	0.2128	2.3	0.58	0.2128	2.3	0.61
258.1	22.9 - 154.4	0.1846	4.9	0.76	0.2355	1.3	0.76	0.2239	1.9	0.43
259.9	32.7 - 203.2	0.1846	5.6	1.81	0.2272	1.5	0.33	0.2280	1.6	0.31
273.2	50.8 - 195.1	0.1846	5.9	1.89	0.2336	3.6	1.30	0.2621	4.1	1.27
273.2	34.9 - 148.7	0.1846	4.9	1.29	0.2657	2.3	0.76	0.2622	2.4	0.73
274.9	49.9 - 200.6	0.1846	8.4	2.98	0.2708	2.0	1.64	0.2670	2.1	1.68
280.7	42.3 - 149.7	0.1846	5.3	1.45	0.2989	1.4	0.91	0.2839	1.7	0.82
283.2	96.4 - 195.1	0.1846	9.7	1.39	0.2856	2.6	3.35	0.2916	2.6	3.61
288.2	50.9 - 150.9	0.1846	6.6	1.26	0.3241	1.8	1.51	0.3076	1.9	1.27
289.9	65.8 - 175.3	0.1846	9.2	4.00	0.2954	4.1	1.42	0.3134	4.5	0.95
293.2	96.4 - 195.0	0.1846	8.6	2.65	0.3244	2.9	4.84	0.3244	2.9	4.73
			4.9	**1.21**		**2.2**	**1.00**		**2.4**	**0.88**

The VlE envelopes of the different sets of calculations at 258.14 K are illustrated below in *Figure 53*.
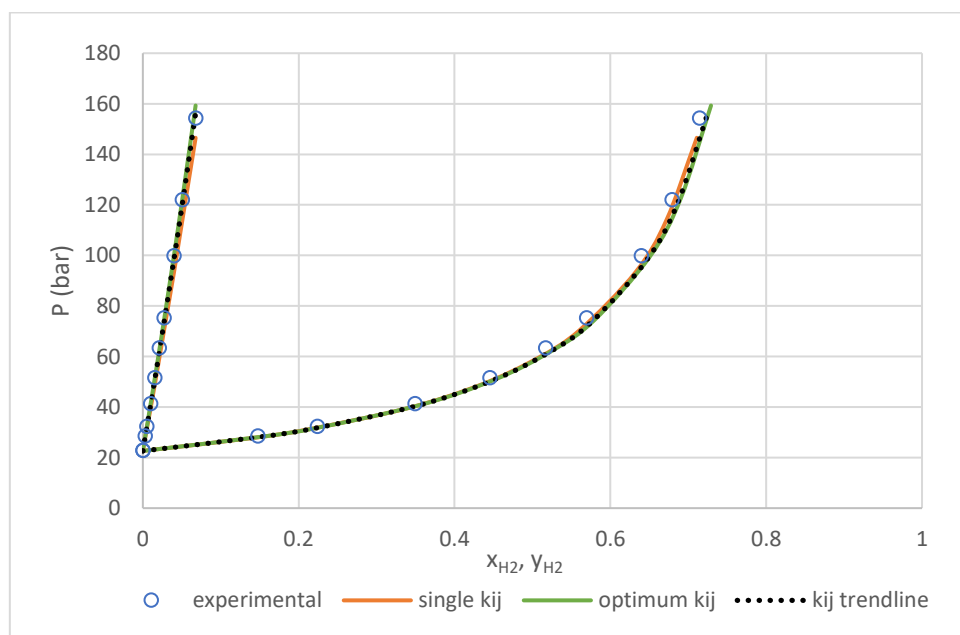
Figure 53: VLE envelope for H_2 – CO_2 in T=258.14 K

The prediction of the bubble point pressure is substantially improved when using the optimal k_{ij} values, as the average deviation is 50% less compared to using a single value independently of the temperature examined. In more detail, the average deviation with the temperature-independent coefficient is 4.9% whereas the optimal coefficients yield a 2.2% average deviation. The improvement in the prediction is more evident in the higher temperatures, above 274 K, where the value for the coefficient needs to be higher than the one obtained from the temperature-independent fitting. The prediction using the values calculated from the model developed closely aligns with the prediction of the optimal k_{ij} values, as the average deviation is 2.4%. The efficacy of the model is attributed to the restricted pressure range of the datasets, as there is no pressure higher than 205 bar.

The calculations regarding the vapor phase composition are comparable with all three values for the binary interaction coefficient examined. The model derived yields a better prediction in the vapor phase, because as explained above, the objective function when determining the optimal k_{ij} values is the minimization of the deviation in the bubble point pressure calculations. The average absolute deviations multiplied by 100 for the three sets of calculations is 1.21, 1.00 and 0.88.

4.13 H_2 – benzene

The datasets that were used in the development of the model are listed in *Table 45* below.

Table 45: VLE datasets for binary mixture H_2 – benzene

NDP	T (K)	P range (bar)	y range	x range	Reference
4	295.0	69.9 - 173.3	-	0.017 - 0.042	Peramanu et al. 1997 [53]
5	433.2	20.9 - 115.1	0.615 - 0.908	0.009 - 0.066	Connolly et al. 1962 [61]
6	443.2	19.0 - 152.2	0.492 - 0.908	0.007 - 0.092	Connolly et al. 1962 [61]
5	453.2	23.1 - 153.7	0.492 - 0.890	0.009 - 0.097	Connolly et al. 1962 [61]
5	463.2	22.5 - 105.6	0.390 - 0.829	0.008 - 0.069	Connolly et al. 1962 [61]
4	473.2	34.0 - 135.8	0.492 - 0.829	0.016 - 0.095	Connolly et al. 1962 [61]
5	483.2	32.4 - 178.0	0.390 - 0.829	0.014 - 0.132	Connolly et al. 1962 [61]
4	493.2	38.7 - 120.8	0.390 - 0.738	0.018 - 0.092	Connolly et al. 1962 [61]
4	503.2	46.2 - 155.9	0.390 - 0.738	0.024 - 0.129	Connolly et al. 1962 [61]
4	513.2	37.2 - 109.5	0.203 - 0.615	0.013 - 0.090	Connolly et al. 1962 [61]
4	523.2	35.8 - 142.0	0.100 - 0.615	0.007 - 0.132	Connolly et al. 1962 [61]
3	533.2	41.6 - 114.7	0.100 - 0.492	0.010 - 0.108	Connolly et al. 1962 [61]
6	323.2	40.7 - 157.3	-	0.012 - 0.046	Park et al. 1996 [62]
6	373.2	25.5 - 127.1	-	0.010 - 0.052	Park et al. 1996 [62]
6	423.2	40.5 - 107.3	-	0.021 - 0.059	Park et al. 1996 [62]
9	338.7	5.3 - 689.3	0.875 - 0.996	0.002 - 0.180	Thompson et al. 1965 [63]
8	394.3	6.7 - 688.3	0.514 - 0.982	0.002 - 0.243	Thompson et al. 1965 [63]
4	433.2	29.5 - 90.3	0.708 - 0.890	0.014 - 0.051	Thompson et al. 1965 [63]
7	308.2	50.5 - 147.8	-	0.014 - 0.039	Sattler et al. 1940 [64]
11	288.2	50.1 - 493.0	-	0.011 - 0.102	Krichevsky et al. 1935 [65]

2	366.5	33.2 - 77.9	0.956 - 0.977	0.014 - 0.033	Brainard et al. 1967 [66]

By fitting each individual isothermal curve and plotting each temperature-dependent k_{ij} that was obtained, as shown in *Figure 54* below, the correlation of *Equation 42* was derived.

$$k_{ij}(T) = 7.25533 \cdot 10^{-6}T^2 - 4.06987 \cdot 10^{-3}T + 8.93293 \cdot 10^{-1} \qquad (Eq.\,42)$$
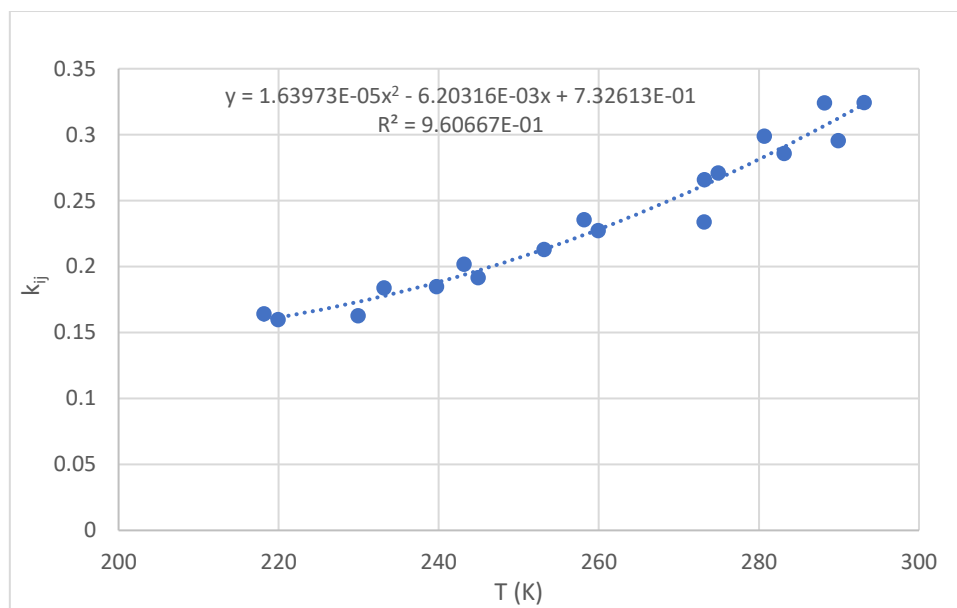

Figure 54: k_{ij} – T plot for binary mixture H_2-benzene

By fitting all datasets that were used in the k_{ij} – T correlation, up to 700 bar, a temperature-independent value for k_{ij} equal to 0.3592 was obtained.

The comparison between all calculations with the different values for the binary interaction coefficient is displayed in *Table 46*.

Table 46: Comparison between different binary interaction coefficient values in the VLE prediction of H_2-benzene

T(K)	P range	k_{ij} T independent			optimal k_{ij} T dependent			k_{ij} trendline		
		value	AADP	100AADy	value	AADP	100AADy	value	AADP	100AADy
288.2	50.1 - 493.0	0.3592	16.5	-	0.2871	7.3	-	0.322973	8.9	-
295.0	69.9 - 173.3	0.3592	7.2	-	0.3204	2.5	-	0.324076	2.9	-
308.2	50.5 - 147.8	0.3592	2.8	-	0.3455	1.4	-	0.328103	2.9	-
323.2	40.7 - 157.3	0.3592	2.4	-	0.3744	1.2	-	0.33579	5.8	-
338.7	5.3 - 689.3	0.3592	6.4	0.11	0.3593	6.4	0.11	0.347151	6.4	0.14
366.5	33.2 - 77.9	0.3592	1.0	0.52	0.3503	0.2	0.56	0.376213	3.0	0.44
373.2	25.5 - 127.1	0.3592	5.6	-	0.4080	1.3	-	0.384927	2.8	-
394.3	6.7 - 688.3	0.3592	5.7	0.59	0.3853	4.8	0.39	0.416481	5.1	0.19
423.2	40.5 - 107.3	0.3592	9.0	-	0.4714	0.8	-	0.470341	0.8	-
433.2	20.9 - 115.1	0.3592	9.7	1.46	0.4989	1.0	0.56	0.491666	1.2	0.51
443.2	19.0 - 152.2	0.3592	9.4	1.72	0.5096	1.6	0.55	0.514546	1.7	0.63

453.2	23.1 - 153.7	0.3592	10.0	2.15	0.5346	1.6	0.65	0.538877	1.7	0.71
463.2	22.5 - 105.6	0.3592	9.9	2.86	0.5642	1.0	0.59	0.564658	1.0	0.59
473.2	34.0 - 135.8	0.3592	11.4	2.93	0.5754	1.6	0.71	0.591891	1.6	0.97
483.2	32.4 - 178.0	0.3592	11.4	3.27	0.6173	2.3	1.09	0.620575	2.3	1.12
493.2	38.7 - 120.8	0.3592	11.8	4.00	0.6559	1.6	1.07	0.650711	1.6	1.02
503.2	46.2 - 155.9	0.3592	12.8	4.21	0.6794	2.4	1.52	0.682297	2.4	1.55
513.2	37.2 - 109.5	0.3592	11.5	4.63	0.7417	1.6	1.33	0.715334	1.7	1.21
523.2	35.8 - 142.0	0.3592	10.4	4.19	0.7324	2.3	1.80	0.749822	2.3	1.78
533.2	41.6 - 114.7	0.3592	11.3	4.35	0.7920	1.6	1.78	0.785762	1.7	1.70
			8.9	**2.28**		**2.7**	**0.78**		**3.4**	**0.77**

The comparison is also visualized in *Figure 55* below.
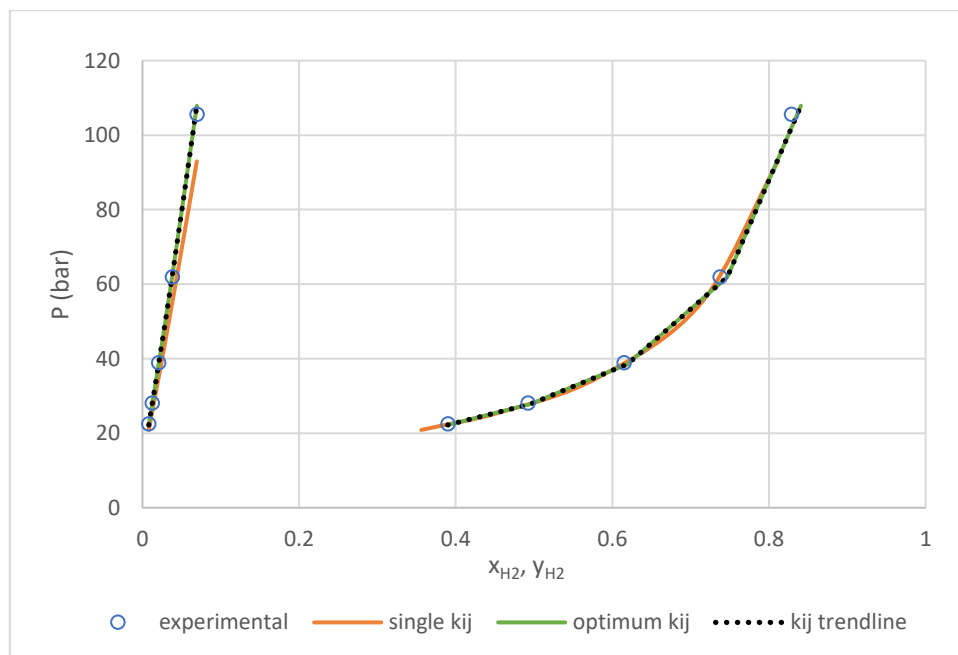
Figure 55: VLE envelope for H_2 – benzene in T=463.15 K

The great difference between the average deviations in the bubble point pressure calculations for the temperature-independent k_{ij} value and the optimal values obtained from the fittings, is attributed to the wide temperature range examined and subsequently the wide range of optimal k_{ij} values that cannot be represented adequately with just one value. That is why the prediction with the temperature-dependent optimal k_{ij} values yields an averade deviation of 2.7%, three times lower than the 8.9% yielded by the temperature-independent optimal k_{ij}. The average deviation when using the derived model is 3.4%. The biggest discrepancies between the second and the third set of calculations regard the lower temperature range, up to 380 K where as it can be seen in *Figure 55* above, the plotted optimal values do not fully align with the trendline derived. Above 380 K, the predictions are essentialy equivalent as the trendline matches more closely the plotted data. That is because most of the datasets in these temperatures belong to the same experimentalist.

As far as the vapor phase composition prediction is concerned, the introduction of a temperature-dependent binary interaction coefficient leads to a significant improvement, by more than 50%, as the original average absolute deviation multiplied by 100 is 2.28 and it is brought down to 0.78. Comparing the results from the optimal k_{ij} calculations and the model derived calculations, the vapor phase composition prediction is fundametally equally accurate as the average absolute deviation is 0.77.

4.14 H_2 – toluene

The datasets that were used in the development of the model are listed in *Table 47* below.

Table 47: VLE datasets for binary mixture H2 – toluene

NDP	T (K)	P range (bar)	y range	x range	Reference
10	298.2	8.7 - 101.2	-	0.003 - 0.030	Brunner et al. 1985 [51]
8	323.2	10.2 - 98.8	-	0.004 - 0.036	Brunner et al. 1985 [51]
7	373.2	9.8 - 97.9	-	0.005 - 0.047	Brunner et al. 1985 [51]
4	295.0	69.90- 173.3	-	0.022 - 0.051	Peramanu et al. 1997 [53]
7	542.2	34.6 - 323.0	-	0.019 - 0.327	Laugier et al. 1980 [67]
7	461.9	20.3 - 253.7	0.667 - 0.943	0.011 - 0.165	Simnick et al. 1978 [68]
7	502.2	20.2 - 252.6	0.350 - 0.891	0.08 - 0.202	Simnick et al. 1978 [68]
6	542.2	30.4 - 253.1	0.210 - 0.799	0.012 - 0.258	Simnick et al. 1978 [68]
5	305.0	14.8 - 69.0	-	0.005 - 0.020	Yin et al. 2006 [69]
5	323.0	17.2 - 71.0	-	0.006 - 0.023	Yin et al. 2006 [69]

By fitting each individual isothermal curve and plotting each temperature-dependent k_{ij} that was obtained, as shown in *Figure 56* below, the correlation of *Equation 43* was derived. It is important that compared to all the previous binary mixtures examined, this is the first linear equation derived. It is possible that if there were datasets available in the temperature range between 375 and 460 K, a significant gap of experimental data, the equation derived could be polynomial, of second order.

$$k_{ij}(T) = 1.33902 \cdot 10^{-3}T - 5.48573 \cdot 10^{-2} \qquad (Eq.\,43)$$
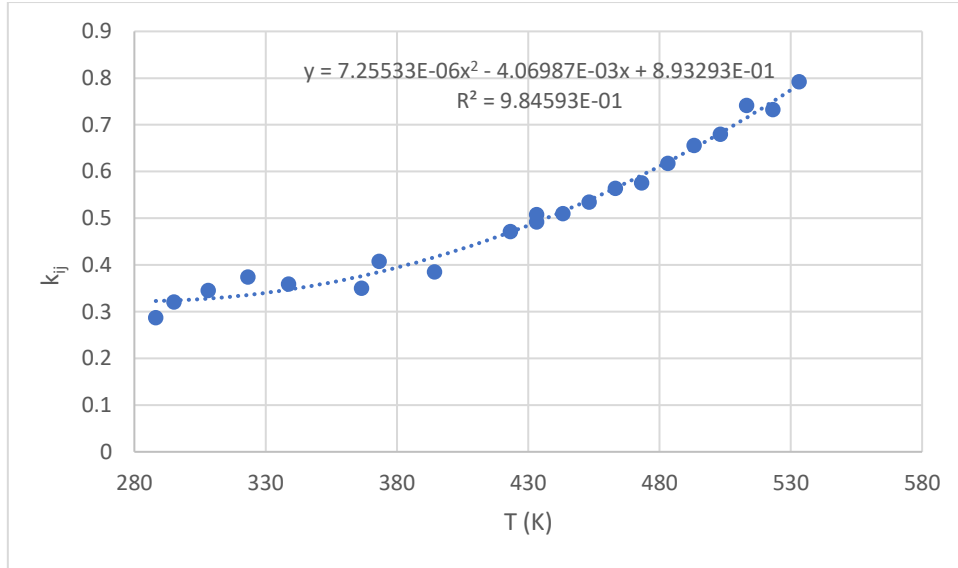
Figure 56: k_{ij} – T plot for binary mixture H_2-toluene

By fitting all datasets that were used in the k_{ij} – T correlation, up to 700 bar, a temperature-independent value for k_{ij} equal to 0.3684 was obtained.

The comparison between all calculations with the different values for the binary interaction coefficient is displayed in *Table 48*.

Table 48: Comparison between different binary interaction coefficient values in the VLE prediction of H_2-toluene

T (K)	P range (bar)	k_{ij} T dependent			optimal k_{ij} T dependent			k_{ij} trendline		
		value	AADP	100AADy	value	AADP2	100AADy	value	AADP	100AADy
295.0	69.9 - 173.3	0.3684	9.4	-	0.3149	1.5	-	0.340154	4.1	-
298.2	8.7 - 101.2	0.3684	3.2	-	0.3488	1.6	-	0.344371	1.7	-
305.0	14.8 - 68.9	0.3684	3.6	-	0.3820	2.7	-	0.353544	4.9	-
323.0	17.2 - 71.0	0.3684	7.9	-	0.4269	2.7	-	0.377646	6.7	-
323.2	10.2 - 98.8	0.3684	2.3	-	0.3543	1.8	-	0.377847	3.3	-
373.2	9.8 - 97.9	0.3684	3.2	-	0.4208	1.4	-	0.444798	5.4	-
461.9	20.3 - 253.7	0.3684	13.2	1.55	0.5620	1.7	1.21	0.563569	1.7	1.21
502.2	10.2 - 252.6	0.3684	14.7	3.51	0.6433	3.3	1.82	0.617532	3.4	1.79
542.2	30.4 - 323.0	0.3684	16.3	5.65	0.6258	4.9	3.11	0.671092	5.3	2.94
			8.7	3.47		2.6	1.99		4.0	1.93

Similarly to the binary mixture of H_2 – benzene, the introduction of the temperature-dependency in the predicition of the bubble point pressure leads to remarkably improved results, as the average deviation occurred is 2.6%, compared to 8.7% when the temperature-independent k_{ij} is used in the calculations. The improvement is especially noticeable in the highest temperatures, above 460 K, where the binary interaction coefficient has a high value and the value of the temperature-independent fitting cannot represent it adequately. The overall gap in the deviations is explained in the binary

mixture of H_2 – benzene. The calculations using the model derived, yield an average deviation of 4.0%. The deviation between the optimal calculations and the calculations from the model is due to the different experimental uncertainty of the datasets in approximate temperatures by different experimentalists. In *Figure 56* above it can be observed that in the temperatures around 323.15 and 542.15 K, there are differnet datasets with different optimal k_{ij} values. The trendline derived thus does not fully align with the plotted optimal k_{ij} values.

Regarding the prediction of the vapor phase composition, the temperature-independent calculations lead to an average deviation multiplied by 100 equal to 3.47 whereas with the temperature-dependent calculations the results are essently equivalent, at 1.99 and 1.93.

4.15 H_2 – m-xylene
The datasets that were used in the development of the model are listed in *Table 49* below.

Table 49: VLE datasets for binary mixture H2 – m-xylene

NDP	T (K)	P range (bar)	y range	x range	Reference
1	323.2	64.5 - 64.5	-	0.025 - 0.025	Connolly et al. 1986 [49]
3	383.2	46.1 - 153.4	-	0.025 - 0.079	Connolly et al. 1986 [49]
3	413.2	40.1 - 131.2	-	0.025 - 0.079	Connolly et al. 1986 [49]
4	433.2	37.1 - 156.9	-	0.025 - 0.102	Connolly et al. 1986 [49]
4	453.2	34.7 - 142.3	-	0.025 - 0.102	Connolly et al. 1986 [49]
5	473.2	33.0 - 167.2	-	0.025 - 0.129	Connolly et al. 1986 [49]
1	483.2	62.0 - 62.0	-	0.051 - 0.051	Connolly et al. 1986 [49]
5	493.2	31.9 - 152.0	-	0.025 - 0.129	Connolly et al. 1986 [49]
5	513.2	31.7 - 138.6	-	0.025 - 0.129	Connolly et al. 1986 [49]
5	523.2	31.8 - 132.5	-	0.025 - 0.129	Connolly et al. 1986 [49]
5	533.2	32.2 - 126.5	-	0.025 - 0.129	Connolly et al. 1986 [49]
5	543.2	32.7 - 120.8	-	0.025 - 0.129	Connolly et al. 1986 [49]
5	553.2	33.5 - 115.4	-	0.025 - 0.129	Connolly et al. 1986 [49]
5	563.2	34.5 - 110.1	-	0.025 - 0.129	Connolly et al. 1986 [49]
5	573.2	35.8 - 104.8	-	0.025 - 0.129	Connolly et al. 1986 [49]
5	583.2	37.2 - 99.2	-	0.025 - 0.129	Connolly et al. 1986 [49]
3	295.0	104.4 - 173.3	-	0.034 - 0.056	Peramanu et al. 1997 [53]
7	462.4	19.9 - 251.3	0.826 - 0.972	0.013 - 0.172	Simnick et al. 1979 [70]
7	502.3	20.0 - 252.6	0.615 - 0.948	0.013 - 0.204	Simnick et al. 1979 [70]
7	542.6	19.9 - 254.4	0.287 - 0.890	0.009 - 0.249	Simnick et al. 1979 [70]
4	308.2	147.8 - 152.7	-	0.052 - 0.053	Sattler et al. 1940 [64]

By fitting each individual isothermal curve and plotting each temperature-dependent k_{ij} that was obtained, as shown in *Figure 57* below, the correlation of *Equation 44* was derived.

$$k_{ij}(T) = 9.07536 \cdot 10^{-6}T^2 - 5.87795 \cdot 10^{-3}T + 1.29824 \qquad (Eq.\,44)$$
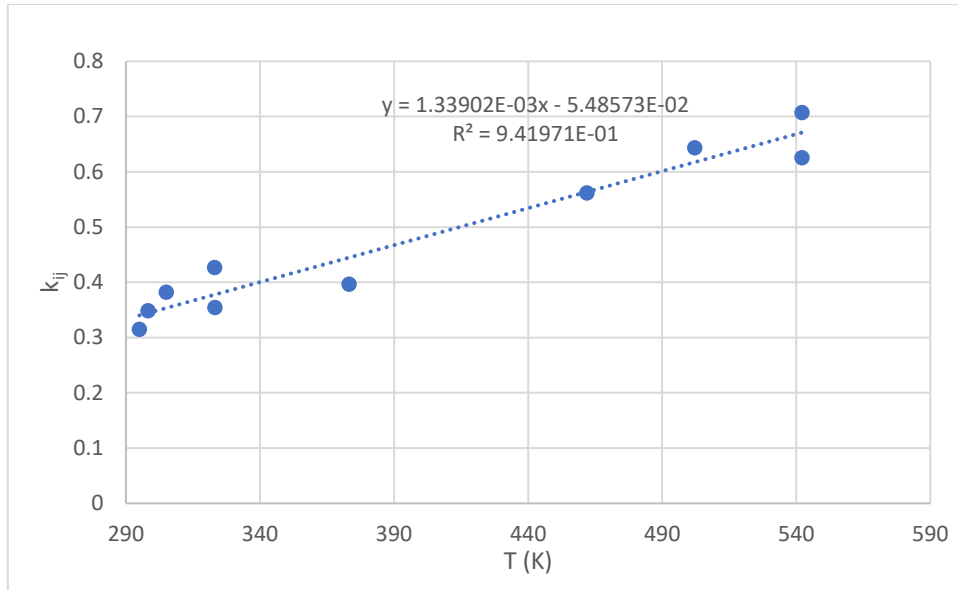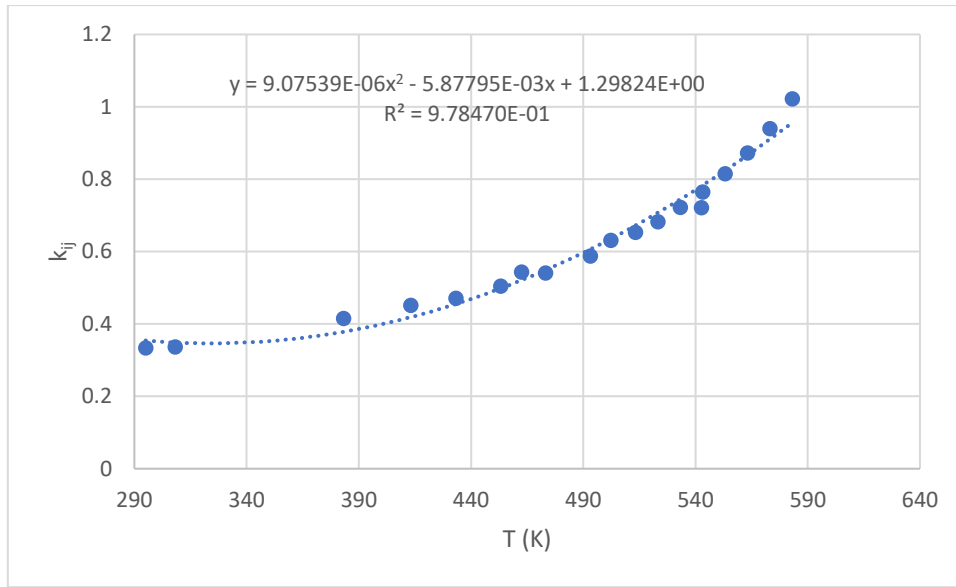

Figure 57: k_{ij} – T plot for binary mixture H_2 - m-xylene

By fitting all datasets that were used in the k_{ij} – T correlation, up to 700 bar, a temperature-independent value for k_{ij} equal to 0.5112 was obtained.

The comparison between all calculations with the different values for the binary interaction coefficient is displayed in *Table 50*.

Table 50: Comparison between different binary interaction coefficient values in the VLE prediction of H_2 – m-xylene

T (K)	P range (bar)	kij T independent			optimal kij T dependent			kij trendline		
		value	AADP	100AADy	value	AADP	100AADy	value	AADP	100AADy
295.0	104.4 - 173.3	0.5112	38.0	-	0.3340	1.5	-	0.3540	4.3	-
308.2	71.0 - 150.5	0.5112	34.2	-	0.3366	0.2	-	0.3487	2.0	-
383.2	46.1 - 153.4	0.5112	11.4	-	0.4153	1.1	-	0.3784	4.1	-
413.2	40.1 - 131.2	0.5112	6.1	-	0.4513	0.9	-	0.4189	3.0	-
433.2	37.1 - 156.9	0.5112	3.6	-	0.4711	1.2	-	0.4549	1.6	-
453.2	34.7 - 142.3	0.5112	1.2	-	0.5049	1.2	-	0.4982	1.2	-
462.4	19.9 - 251.3	0.5112	3.9	0.78	0.5439	3.1	0.69	0.5207	3.5	0.75
473.2	33.0 - 167.2	0.5112	2.1	-	0.5407	1.5	-	0.5488	1.6	-
493.2	31.9 - 152.0	0.5112	5.0	-	0.5874	1.5	-	0.6066	1.8	-
502.3	20.0 - 252.6	0.5112	8.5	1.89	0.6308	3.6	1.29	0.6355	3.6	1.27
513.2	31.7 - 138.6	0.5112	7.6	-	0.6534	1.5	-	0.6717	1.9	-
523.2	31.8 - 132.5	0.5112	8.8	-	0.6820	1.6	-	0.7070	1.8	-
533.2	32.2 - 126.5	0.5112	9.9	-	0.7224	1.6	-	0.7441	1.8	-
542.6	19.9 - 254.4	0.5112	11.1	3.36	0.7211	3.6	2.09	0.7808	3.9	2.24
543.2	32.7 - 120.8	0.5112	10.8	-	0.7644	1.7	-	0.7830	1.7	-
553.2	33.5 - 115.4	0.5112	11.7	-	0.8149	1.7	-	0.8237	1.7	-
563.2	34.5 - 110.1	0.5112	12.3	-	0.8724	1.8	-	0.8662	1.9	-

573.2	35.8 - 104.8	0.5112	12.8	-	0.9400	1.9	-	0.9106	2.3	-
583.2	37.2 - 99.2	0.5112	13.0	-	1.0222	2.1	-	0.9567	2.7	-
			10.4	**2.01**		**1.9**	**1.36**		**2.5**	**1.42**

Similarly to the mixtures of hydrogen with benzene and toluene, the single temperature-independent k_{ij} value cannot represent the wide range of the temperature-dependent k_{ij} values obtained from the fittings. That is why the average deviation in the prediction of the bubble point pressure with the optimal k_{ij} values is five times lower than with the temperature-independent k_{ij}, and more specifically 1.9% and 10.4% respectively. The average deviation occurred with the calculations from the developed model is 2.5%, with the most significant deviations from the optimal calculations found in the lower temperatures, from 295 K to 413.15 K, as in this temperature range the trendline does not fully align with the plotted points.

The prediction of the vapor phase composition is also improved by the introduction of temperature-dependent k_{ij} values. The prediction is in general better as the temperature decreases and the average absolute deviation multiplied by 100 for the three sets of calculations is 2.01, 1.36 and 1.42.

4.16 H$_2$ – p-xylene
The datasets that were used in the development of the model are listed in *Table 51* below.

Table 51: VLE datasets for binary mixture H2 – p-xylene

NDP	T (K)	P range (bar)	y range	x range	Reference
3	353.2	51.7 - 147.8	-	0.028 - 0.076	Connolly et al. 1986 [49]
3	363.2	49.0 - 140.0	-	0.028 - 0.076	Connolly et al. 1986 [49]
3	373.2	46.6 - 132.9	-	0.028 - 0.076	Connolly et al. 1986 [49]
3	383.2	44.3 - 126.2	-	0.028 - 0.076	Connolly et al. 1986 [49]
3	393.2	42.2 - 120.1	-	0.028 - 0.076	Connolly et al. 1986 [49]
3	403.2	40.3 - 114.1	-	0.028 - 0.076	Connolly et al. 1986 [49]
5	413.2	38.6 - 148.7	-	0.028 - 0.100	Connolly et al. 1986 [49]
4	423.2	37.0 - 141.9	-	0.028 - 0.100	Connolly et al. 1986 [49]
5	433.2	35.4 - 135.5	-	0.028 - 0.100	Connolly et al. 1986 [49]
4	443.2	34.1 - 129.5	-	0.028 - 0.100	Connolly et al. 1986 [49]
5	453.2	32.8 - 123.8	-	0.028 - 0.100	Connolly et al. 1986 [49]
4	463.2	31.7 - 118.5	-	0.028 - 0.100	Connolly et al. 1986 [49]
6	473.2	30.6 - 147.4	-	0.028 - 0.127	Connolly et al. 1986 [49]
5	483.2	29.7 - 141.0	-	0.028 - 0.127	Connolly et al. 1986 [49]
5	493.2	28.9 - 135.0	-	0.028 - 0.127	Connolly et al. 1986 [49]
5	503.2	28.2 - 129.3	-	0.028 - 0.127	Connolly et al. 1986 [49]
5	513.2	27.6 - 124.0	-	0.028 - 0.127	Connolly et al. 1986 [49]
6	523.2	27.2 - 148.4	-	0.028 - 0.155	Connolly et al. 1986 [49]
6	533.2	26.9 - 142.0	-	0.028 - 0.155	Connolly et al. 1986 [49]
6	543.2	26.7 - 136.0	-	0.028 - 0.155	Connolly et al. 1986 [49]
6	553.2	26.7 - 130.0	-	0.028 - 0.155	Connolly et al. 1986 [49]

| 6 | 563.2 | 26.8 - 124.3 | - | 0.028 - 0.155 | Connolly et al. 1986 [49] |
| 6 | 573.2 | 27.0 - 118.9 | - | 0.028 - 0.155 | Connolly et al. 1986 [49] |

By fitting each individual isothermal curve and plotting each temperature-dependent k_{ij} that was obtained, as shown in *Figure 58* below, the correlation of *Equation 45* was derived.

$$k_{ij}(T) = 5.90530 \cdot 10^{-6}T^2 - 4.06659 \cdot 10^{-3}T + 9.84956 \cdot 10^{-1} \qquad (Eq.\,45)$$
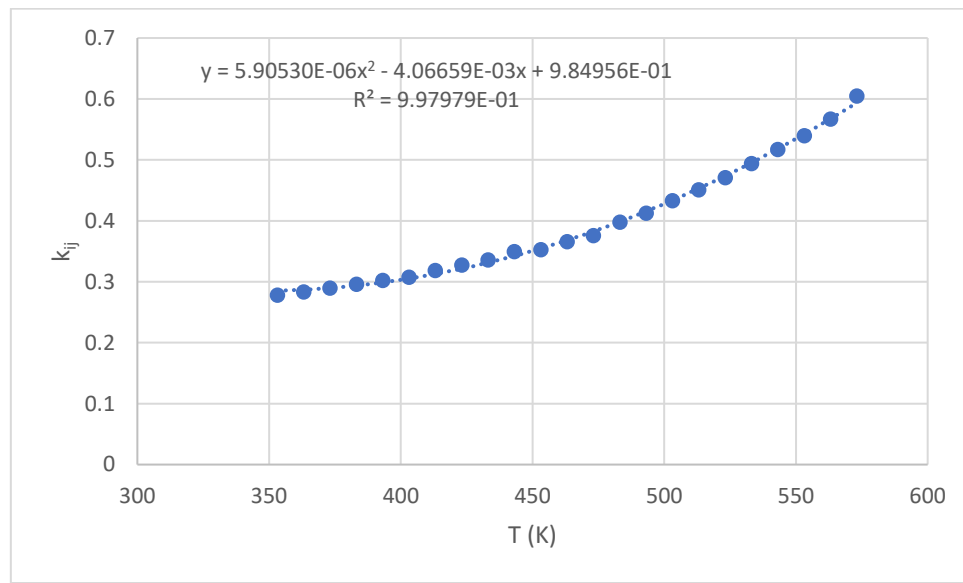
Figure 58: k_{ij} – T plot for binary mixture H_2 - p-xylene

By fitting all datasets that were used in the k_{ij} – T correlation, up to 700 bar, a temperature-independent value for k_{ij} equal to 0.3204 was obtained.

The comparison between all calculations with the different values for the binary interaction coefficient is displayed in *Table 52*.

Table 52: Comparison between different binary interaction coefficient values in the VLE prediction of H_2 – p-xylene

T(K)	P range (bar)	k_{ij} T independent			optimal k_{ij} T dependent			k_{ij} trendline		
		value	AADP	100AADy	value	AADP	100AADy	value	AADP	100AADy
353.2	51.7 - 147.8	0.3204	5.5	-	0.2780	0.7	-	0.2858	1.0	-
363.2	49.0 - 140.0	0.3204	4.5	-	0.2833	0.5	-	0.2873	0.7	-
373.2	46.6 - 132.9	0.3204	3.5	-	0.2897	0.5	-	0.2900	0.5	-
383.2	44.3 - 126.2	0.3204	2.7	-	0.2958	0.3	-	0.2939	0.3	-
393.2	42.2 - 120.1	0.3204	1.9	-	0.3021	0.2	-	0.2989	0.3	-
403.2	40.3 - 114.1	0.3204	1.3	-	0.3075	0.1	-	0.3052	0.2	-
413.2	38.6 - 148.7	0.3204	0.2	-	0.3182	0.2	-	0.3126	0.5	-
423.2	37.0 - 141.9	0.3204	0.6	-	0.3272	0.3	-	0.3212	0.5	-
433.2	35.4 - 135.5	0.3204	1.2	-	0.3355	0.5	-	0.3310	0.6	-
443.2	34.1 - 129.5	0.3204	2.0	-	0.3496	0.8	-	0.3420	0.9	-

453.2	32.8 - 123.8	0.3204	2.3	-	0.3523	1.2	-	0.3541	1.2	-
463.2	31.7 - 118.5	0.3204	3.1	-	0.3659	1.5	-	0.3675	1.5	-
473.2	30.6 - 147.4	0.3204	3.7	-	0.3759	2.2	-	0.3820	2.2	-
483.2	29.7 - 141.0	0.3204	5.1	-	0.3977	2.2	-	0.3977	2.2	-
493.2	28.9 - 135.0	0.3204	5.9	-	0.4123	2.8	-	0.4146	2.8	-
503.2	28.2 - 129.3	0.3204	6.6	-	0.4327	3.3	-	0.4327	3.3	-
513.2	27.6 - 124.0	0.3204	7.3	-	0.4508	4.0	-	0.4520	4.0	-
523.2	27.2 - 148.4	0.3204	8.8	-	0.4707	4.6	-	0.4724	4.6	-
533.2	26.9 - 142.0	0.3204	9.6	-	0.4941	5.4	-	0.4941	5.4	-
543.2	26.7 - 136.0	0.3204	10.3	-	0.5169	6.3	-	0.5169	6.3	-
553.2	26.7 - 130.0	0.3204	11.0	-	0.5396	7.3	-	0.5409	7.3	-
563.2	26.8 - 124.3	0.3204	12.2	-	0.5667	8.4	-	0.5661	8.4	-
573.2	27.0 - 118.9	0.3204	13.4	-	0.6048	9.7	-	0.5925	9.8	-
			6.0			**3.3**			**3.3**	

The use of the temperature indpendent k_{ij} yields an average deviation of 6.0% in the calculation of the bubble point pressure. The prediction is improved to 3.3% with the optimal k_{ij} values obtained from the fittings whereas the model calculations lead to a 3.3% average deviation, following closely the second set of calculations. It is important to note that the model developed for the binary mixture of H_2 – p-xylene closely replicates the same results in the calculations, as all datasets examined belong to the same experimentalist, and consequently the relative experimental uncertainty is minimized between datasets. This means that the optimal k_{ij} values all follow closely the trendline derived and that is why the coefficient of determination is really high, almost 0.998.

No experimental data for the vapor composition was available and therefore no comparisons were made.

4.17 H_2 – cyclohexane
The datasets that were used in the development of the model are listed in *Table 53* below.

Table 53: VLE datasets for binary mixture H_2 – cyclohexane

NDP	T (K)	P range (bar)	y range	x range	Reference
3	343.2	38.6 - 160.1	-	0.020 - 0.078	Connolly et al. 1986 [49]
3	353.2	36.5 - 150.3	-	0.020 - 0.078	Connolly et al. 1986 [49]
3	363.2	34.8 - 141.5	-	0.020 - 0.078	Connolly et al. 1986 [49]
3	373.2	33.3 - 133.5	-	0.020 - 0.078	Connolly et al. 1986 [49]
4	383.2	32.0 - 164.8	-	0.020 - 0.100	Connolly et al. 1986 [49]
4	393.2	30.9 - 155.9	-	0.020 - 0.100	Connolly et al. 1986 [49]
4	403.2	30.1 - 147.5	-	0.020 - 0.100	Connolly et al. 1986 [49]
4	413.2	29.5 - 140.5	-	0.020 - 0.100	Connolly et al. 1986 [49]
4	423.2	29.2 - 133.6	-	0.020 - 0.100	Connolly et al. 1986 [49]
4	433.2	29.1 - 127.4	-	0.020 - 0.100	Connolly et al. 1986 [49]
5	443.2	29.2 - 159.1	-	0.020 - 0.130	Connolly et al. 1986 [49]

5	453.2	29.5 - 151.5	-	0.020 - 0.130	Connolly et al. 1986 [49]
5	463.2	30.1 - 144.3	-	0.020 - 0.130	Connolly et al. 1986 [49]
5	473.2	31.0 - 137.7	-	0.020 - 0.130	Connolly et al. 1986 [49]
6	483.2	31.7 - 131.4	-	0.019 - 0.130	Connolly et al. 1986 [49]
5	493.2	33.5 - 125.2	-	0.020 - 0.130	Connolly et al. 1986 [49]
4	295.0	69.9 - 173.3	-	0.029 - 0.068	Peramanu et al. 1997 [53]
8	338.7	6.9 - 690.4	0.903 - 0.994	0.004 - 0.262	Thompson et al. 1965 [63]
13	310.9	34.5 - 551.6	0.992 - 0.997	0.014 - 0.189	Berty et al. 1966 [71]
13	377.6	34.5 - 551.6	0.935 - 0.984	0.019 - 0.264	Berty et al. 1966 [71]
13	410.9	34.5 - 551.6	0.858 - 0.968	0.022 - 0.292	Berty et al. 1966 [71]
3	332.0	5.7 - 46.0	-	0.003 - 0.023	Ronze et al. 2002 [72]
24	293.2	49.6 - 658.6	-	0.022 - 0.188	Krichevskii et al. 1958 [73]
25	313.2	50.6 - 677.9	-	0.022 - 0.217	Krichevskii et al. 1958 [73]
26	333.2	50.1 - 667.7	-	0.026 - 0.266	Krichevskii et al. 1958 [73]

By fitting each individual isothermal curve and plotting each temperature-dependent k_{ij} that was obtained, as shown in *Figure 59* below, the correlation of *Equation 46* was derived.

$$k_{ij}(T) = 5.24957 \cdot 10^{-6}T^2 - 2.44214 \cdot 10^{-3}T + 5.41541 \cdot 10^{-1} \qquad (Eq.\,46)$$
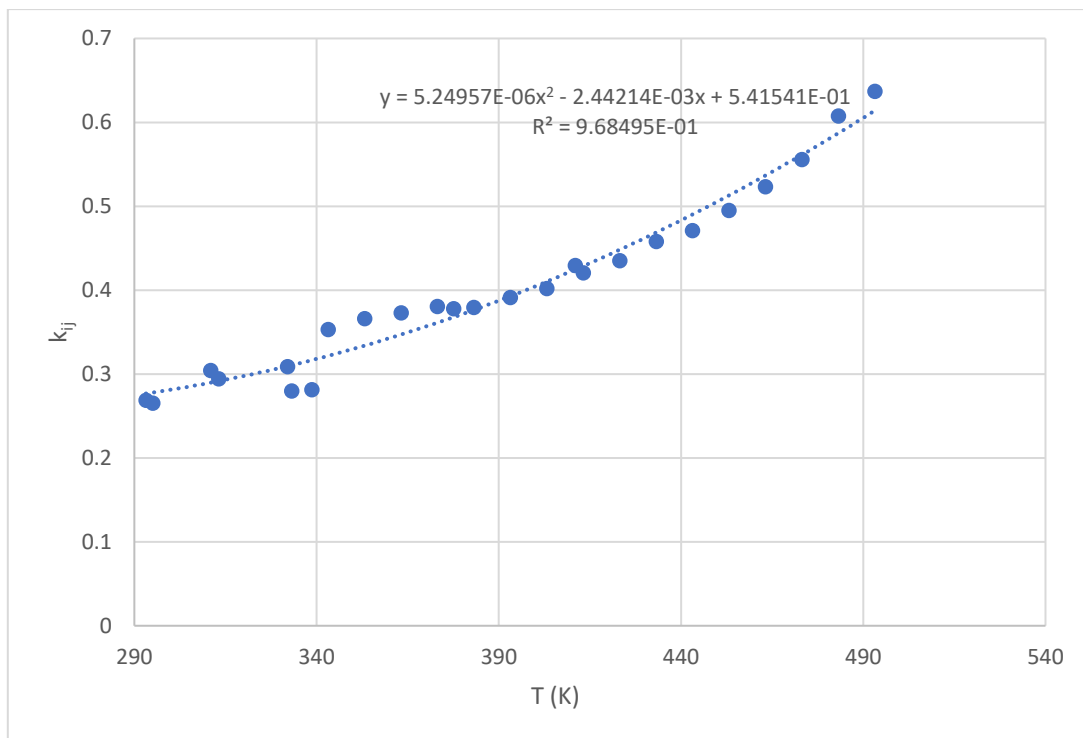

Figure 59: k_{ij} – T plot for binary mixture H_2 - cyclohexane

By fitting all datasets that were used in the k_{ij} – T correlation, up to 700 bar, a temperature-independent value for k_{ij} equal to 0.2995 was obtained.

The comparison between all calculations with the different values for the binary interaction coefficient is displayed in *Table 54*.

Table 54: Comparison between different binary interaction coefficient values in the VLE prediction of H_2 – cyclohexane

		kij T independent			optimal kij T dependent			kij trendline		
T(K)	P range (bar)	value	AADP	100AADy	value	AADP	100AADy	value	AADP	100AADy
293.2	49.6 - 658.6	0.2995	6.7	-	0.2684	3.5	-	0.2768	3.8	-
295.0	69.9 - 173.3	0.2995	5.8	-	0.2652	2.0	-	0.2780	2.1	-
310.9	34.5 - 551.6	0.2995	7.7	0.04	0.3043	7.6	0.04	0.2897	8.0	0.04
313.2	34.5 - 551.6	0.2995	4.0	-	0.2940	4.0	-	0.2916	4.1	-
332.0	5.7 - 46.0	0.2995	1.9	-	0.3087	1.7	-	0.3094	1.7	-
333.2	50.1 - 667.7	0.2995	5.7	-	0.2798	5.3	-	0.3106	6.5	-
338.7	6.9 - 690.4	0.2995	5.6	0.12	0.2814	5.0	0.12	0.3166	6.3	0.13
343.2	38.6 - 160.1	0.2995	6.7	-	0.3530	1.5	-	0.3217	4.1	-
353.2	36.5 - 150.3	0.2995	7.1	-	0.3659	1.4	-	0.3338	3.2	-
363.2	34.8 - 141.5	0.2995	7.5	-	0.3728	1.2	-	0.3470	2.4	-
373.2	33.3 - 133.5	0.2995	8.0	-	0.3805	1.1	-	0.3612	1.7	-
377.6	34.5 - 551.6	0.2995	11.5	0.27	0.3776	6.6	0.25	0.3679	6.8	0.24
383.2	32.0 - 164.8	0.2995	8.1	-	0.3791	1.4	-	0.3765	1.4	-
393.2	30.9 - 155.9	0.2995	8.7	-	0.3913	1.4	-	0.3928	1.4	-
403.2	30.1 - 147.5	0.2995	9.1	-	0.4018	1.3	-	0.4102	1.3	-
410.9	34.5 - 551.6	0.2995	14.9	0.67	0.4292	3.6	0.43	0.4245	3.8	0.42
413.2	29.5 - 140.5	0.2995	10.0	-	0.4206	1.3	-	0.4286	1.4	-
423.2	29.2 - 133.6	0.2995	10.5	-	0.4351	1.2	-	0.4481	1.4	-
433.2	29.1 - 127.4	0.2995	11.1	-	0.4579	1.2	-	0.4686	1.3	-
443.2	29.2 - 159.1	0.2995	11.7	-	0.4710	1.5	-	0.4902	1.9	-
453.2	29.5 - 151.5	0.2995	12.2	-	0.4949	1.5	-	0.5129	1.8	-
463.2	30.1 - 144.3	0.2995	12.7	-	0.5232	1.5	-	0.5365	1.6	-
473.2	31.0 - 137.7	0.2995	13.1	-	0.5554	1.5	-	0.5613	1.5	-
483.2	31.7 - 131.4	0.2995	12.8	-	0.6074	1.7	-	0.5870	1.7	-
493.2	33.5 - 125.2	0.2995	13.7	-	0.6367	1.6	-	0.6139	1.9	-
			8.4	0.29		3.6	0.22		4.0	0.22

Similarly to the binary mixtures of H_2-benzene and H_2-toluene, the calculations with the fitted k_{ij} values are remarkably more accurate than those performed with the temperature-independent coefficient, as the deviation for the first set of calculations is 2.5% and for the latter 9.1%. The explanation for this discrepancy is stated in the binary mixture of H_2-benzene and it is more noticeable in the higher temperature range, above 400 K. The average deviation in the calculations with the derived model is close to the optimal, 2.9%. The biggest discrepancies are found in the isothermal curves of 343.15 – 373.15 K where the trendline does not fully align with the plotted optimal k_{ij} values.

The vapor phase composition calculations are comparable with all values for the binary interaction coefficient examined, and especially the calculations with the temperature-dependent values are essentially equal. More specifically, the average absolute deviation

multiplied by 100 for the temperature-independent calculations is 0.29 and for the others it is 0.22.

4.18 H$_2$ – methylcyclohexane

The datasets that were used in the development of the model are listed in *Table 55* below.

Table 55: VLE datasets for binary mixture H$_2$ – methylcyclohexane

NDP	T (K)	P range (bar)	y range	x range	Reference
5	295.0	69.9 - 207.8	-	0.033 - 0.095	Peramanu et al. 1997 [53]
9	424.2	24.5 - 882.6	0.925 - 0.978	0.022 - 0.492	Peter et al. 1960 [74]
9	471.7	24.5 - 882.6	0.707 - 0.941	0.023 - 0.597	Peter et al. 1960 [74]
9	498.9	24.5 - 784.5	0.464 - 0.900	0.017 - 0.638	Peter et al. 1960 [74]

By fitting each individual isothermal curve and plotting each temperature-dependent k$_{ij}$ that was obtained, as shown in *Figure 60* below, the correlation of *Equation 47* was derived.

$$k_{ij}(T) = 6.03321 \cdot 10^{-4}T + 9.49419 \cdot 10^{-2} \qquad (Eq.47)$$
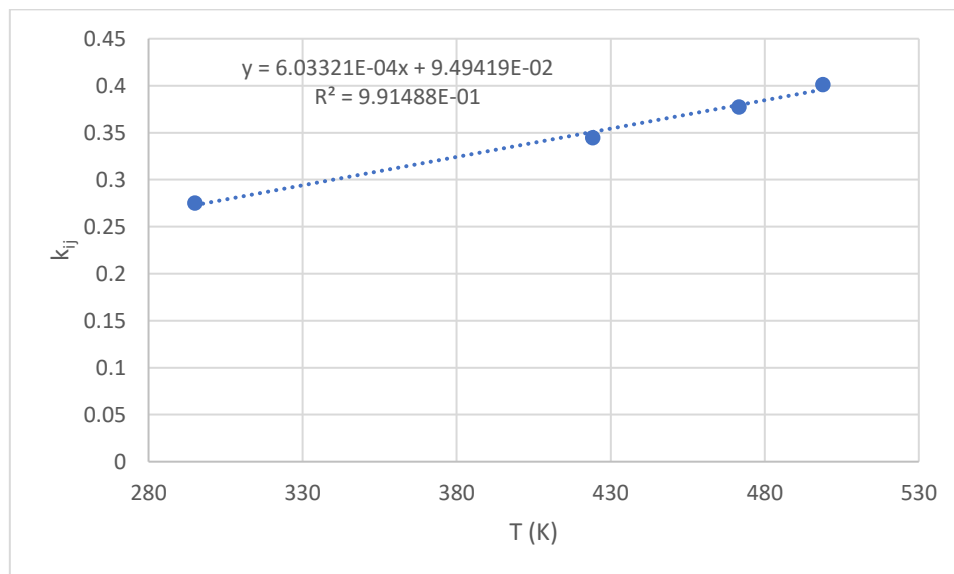
Figure 60: k$_{ij}$ – T plot for binary mixture H$_2$ - methylcyclohexane

By fitting all datasets that were used in the k$_{ij}$ – T correlation, up to 700 bar, a temperature-independent value for k$_{ij}$ equal to 0.3323 was obtained.

The comparison between all calculations with the different values for the binary interaction coefficient is displayed in *Table 56*.

Table 56: Comparison between different binary interaction coefficient values in the VLE prediction of H$_2$ – methylcyclohexane

T(K)	P range (bar)	k$_{ij}$ T independent			optimal k$_{ij}$ T dependent			k$_{ij}$ trendline		
		value	AADP	100AADy	value	AADP	100AADy	value	AADP	100AADy

295.0	69.9 - 207.8	0.3323	9.4	-	0.2754	3.9	-	0.2729	3.8	-
424.2	24.5 - 686.5	0.3323	4.5	2.26	0.3449	4.5	2.18	0.3508	4.5	2.15
471.7	24.5 - 686.5	0.3323	5.4	3.97	0.3775	4.6	3.61	0.3795	4.6	3.59
498.9	24.5 - 588.4	0.3323	8.3	5.80	0.4014	5.2	5.20	0.3959	5.4	5.23
			6.6	**4.01**		**4.6**	**3.66**		**4.6**	**3.66**

A visual comparison between the different sets of calculations is shown in *Figure 61* below.
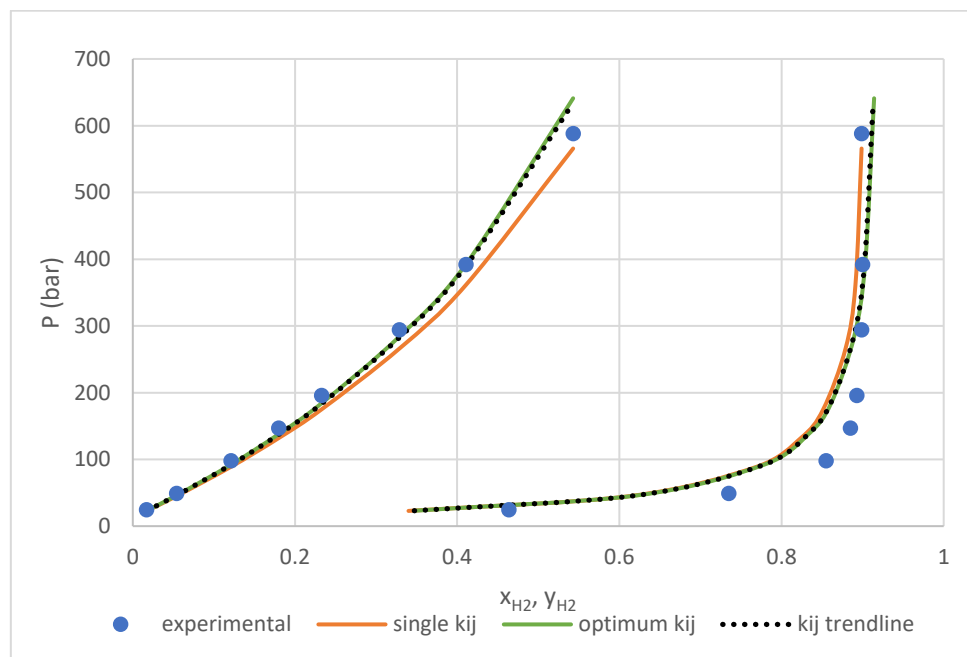
Figure 61: VLE envelope for H_2 – methylcyclohexane in T=498.85K

The prediction of the bubble point pressure for the binary mixture of H_2 – methylcyclohexane is of lower accuracy compared to the rest of the binary mixtures examined in this work. Considering that most of the datasets examined belong to the same experimentalist, it can be concluded that the datasets have higher experimental uncertainty. The average deviation with the optimal k_{ij} calculations is 4.6%, an improvement from 6.6% yielded by the calculations with the temperature-independent k_{ij}. The same average deviation of 4.6% is obtained with the calculations made with the developed model. The close match of the calculations was expected since the trendline derived is linear and the coefficient of determination is very high, above 0.99.

The prediction of the vapor phase composition is also relatively poor compared to other binary mixtures examined, as seen in *Figure 61* and by the values of *Table 56*. The average absolute deviation multiplied by 100 for the calculations with the temperature-independent k_{ij} is 4.01 and for the temperature-dependent calculations 3.66.

4.19 General remarks

While conducting the fittings of the binary interaction parameter for the mixtures examined, some remarks were concluded:

- The heavier the second compound of the binary mixture, the higher the value for the binary interaction coefficient, as expected, due to the increase of size asymmetry.

- For hydrocarbons with a carbon number equal or higher than 10, a constant value of 0.4 is proposed for the temperature-independent binary interaction coefficient. In the mixtures of hydrogen with hydrocarbons with a carbon number of 5 and up it is observed that the optimal temperature-independent k_{ij} value increases at a decreasing rate and stabilizes around 0.4 for a carbon number of 10. This value is therefore proposed for heavier hydrocarbons.

- It is very important to note that the work analyzed here is based on experimental data. As with all experimental data, experimental uncertainty should be considered. One very important factor that can lead to unconcise data is the different experimental procedures, techniques and equipment used by various researchers. That is why, while performing the regression analysis, an evaluation of the datasets' reliability was carried out and unreliable datasets were not involved in trendline derivation. More specifically, apart from the evaluation described in Section 4.1, if a value for the optimal temperature-dependent coefficient exhibited high discrepancy from the optimal values obtained in adjacent temperatures, the particular dataset was considered unreliable and not used in the correlation.

- When determining a k_{ij} value for datasets that contained points in a wide pressure range, the k_{ij} was highly influenced by the high pressures and thus the final value was very different from others obtained from nearby isotherms that contained data in a shorter pressure range. However, choice of the equation of state coupled with classical mixing rules imply that the interaction parameters are independent of pressure and composition. As it is known, classic cubic EoS fall short on predicting the phase envelope at the high pressures. As it was observed in this work, the EoS cannot reproduce the curvature of the phase envelope at this region.

- In general, the vapor phase composition is more accurately predicted than the bubble point pressure at lower pressures. That is because in the vapor phase the intermolecular forces are weaker and therefore the model's performance is stronger compared to the liquid phase. At higher pressures however, the intermolecular forces are significant and therefore the model's accuracy is compromised.

4.20 UMR-PRU Comparison

To validate the efficiency of the model, a comparison with the model UMR-PRU is made for the experimental data of the binary mixtures evaluated. The results of the average deviations for the bubble point pressure and the vapor phase composition are presented in *Table 57* below.

Mixture	optimal T ind kij		optimal T dep kij		trendline kij		UMR-PRU	
	%AADP	100AADy	%AADP	100AADy	%AADP	100AADy	%AADP	100AADy
$H_2 - C_1$	13.3	2.73	6.0	1.79	6.9	1.83	2.8	1.65
$H_2 - C_2$	19.0	2.28	8.9	1.15	10.1	1.18	4.4	1.08
$H_2 - C_3$	10.4	1.46	5.8	0.98	6.7	0.94	7.4	0.94
$H_2 - nC_4$	13.3	2.29	4.5	0.97	6.6	0.93	9.4	1.05
$H_2 - nC_5$	8.7	0.63	2.5	0.45	3.0	0.43	8.1	0.69
$H_2 - nC_6$	5.1	-	1.1	-	1.4	-	3.3	-
$H_2 - nC_8$	9.2	2.99	1.8	1.00	2.5	1.06	2.9	0.71
$H_2 - nC_{10}$	7.4	-	1.2	-	3.0	-	5.4	-
$H_2 - CO_2$	4.9	1.21	2.2	1.00	2.4	0.88	3.1	1.32
$H_2 - benzene$	8.9	2.28	2.7	0.78	3.4	0.77	5.0	1.02
$H_2 - toluene$	8.7	3.47	2.6	1.99	4.0	1.93	6.8	2.17
$H_2 - cyclohexane$	8.4	0.29	3.6	0.22	4.0	0.22	6.6	0.17
$H_2 - methylcylohexane$	6.6	4.01	4.6	3.66	4.6	3.66	5.9	2.77
$H_2 - pxylene$	6.0	-	3.3	-	3.3	-	5.1	-
$H_2 - mxylene$	10.4	2.01	1.9	1.36	2.5	1.42	8.2	2.05

Examining the results displayed in *Table 57* above, it can be concluded that the two models are comparable. More specifically, UMR-PRU has the edge over the model developed in this work for the smaller molecules, namely methane and ethane, as they consist of only one group, as described in the development of UMR-PRU [16]. For the more complex molecules that consist of more groups, the model developed in this work yields better results in the bubble point pressure calculations. As far as the vapor phase composition prediction is concerned, for the mixtures of $H_2 - C_3$ up to $H_2 - nC_5$ and for most aromatic mixtures, this work's model has better performance.

5 Multicomponent Mixtures

In order to further validate the models developed in this work for the prediction of the VLE of the binary mixtures, the calculated binary interaction coefficients will be applied to multicomponent systems to make VLE predictions. The binary interaction coefficients between the other components of the mixture are retrieved from Aspen HYSYS. A comparison will be made between the developed model and UMR-PRU.

The multicomponent mixtures evaluated in this work are presented in *Table 58* below.

Table 58: Multicomponent mixtures evaluated in this work

Mixture	T range (K)	P range (bar)	H_2 liquid composition range	H_2 range vapor composition range	Reference	Experimental points
$H_2 - C_1 - C_2$	115.3 – 255.5	13.5 – 137.9	0.0000 – 0.2030	0.0000 – 0.9974	Cosway et al. 1959 [75]	113
$H_2 - C_1 - C_3$	144.3 – 255.4	34.5 – 69.0	0.0000 – 0.0781	0.0000 – 0.9990	Benham et al. 1957 [76]	40
$H_2 - C_1 - CO_2$	227.4 – 258.2	68.9 – 276.1	0.0000 – 0.2270	0.0000 – 0.8285	Freitag et al. 1986 [50]	35
$H_2 - CO_2 - nC_5$	273.15 – 323.2	68.9 – 276.1	0.0036 – 0.2710	0.0268 – 0.9136	Freitag et al. 1986 [50]	28
$H_2 - CO_2$ - toluene	305.0 – 343.0	12.3 – 103.5	0.0030 – 0.0420	0.6330 – 0.9540	Yin et al. 2006 [69]	65
$H_2 -$ benzene $- cyC_6 - nC_6$	366.5 – 422.0	34.8 – 139.5	0.0204 – 0.1105	0.7975 – 0.9787	Brainard et al. 1967 [66]	36

The results of the calculations for each mixture examined are presented in *Table 59* below. It is noted that the deviations in the vapor phase composition regard hydrogen.

Table 59: Trendline-calculated kij and UMR-PRU VLE comparison on multicomponent systems

Mixture	k_{ij} trendline			UMR-PRU		
	%AADP	$100AADy_{H2}$	$100AADy_2$*	%AADP	$100AADy_{H2}$	$100AADy_2$*
$H_2 - C_1 - C_2$	15.5	3.25	2.48	17.6	1.55	1.44
$H_2 - C_1 - C_3$	8.4	2.18	2.02	11.8	2.80	2.40
$H_2 - C_1 - CO_2$	10.5	2.59	1.12	6.4	0.83	0.44
$H_2 - CO_2 - nC_5$	6.3	1.86	1.71	6.6	1.68	1.59
$H_2 - CO_2 -$ toluene	7.7	2.67	2.61	4.1	1.66	1.62
$H_2 -$ benzene $- cyC_6 - nC_6$	5.9	0.37	0.12	3.2	0.51	0.21

*$AADy_2$ refers to the second compound of the examined mixture

From the results presented in *Table 59* above it can be concluded that the two models have comparable performance, although UMR-PRU is more robust. It is important to note that the k_{ij} between the compounds other than hydrogen in the case of the trendline calculations are retrieved from Aspen HYSYS and they have not been therefore evaluated

in this work, whereas the UMR-PRU calculations use coefficients that have been derived by the model.

Overall, efficient binary mixture correlations do not necessarily yield good results in multicomponent systems. This observation is apparent in mixtures like H_2 – benzene – cyclohexane – normal hexane where the k_{ij}s derived from the trendline of this work outperform VLE calculations of UMR-PRU but in ternary systems UMR-PRU is more accurate. The opposite is also observed.

6 Conclusions

For the optimal design, operation and scaling up of the hydrogen technology processes, accurate knowledge of pure hydrogen's and hydrogen-containing mixtures' behavior remains a highly important challenge. Many attempts have been made to develop or modify popular thermodynamic models to accurately reproduce experimental data but it is difficult to conclude to a single model that is very precise in all the properties of interest and in all temperature and pressure ranges. In addition, a lack of experimental data especially in the cryogenic area is identified, limiting the possible modifications of the models. A lack of experimental data is also found for mixtures of hydrogen, especially consisting of more than two compounds. As mentioned in Section 1.1.4, in order to achieve the transition to clean energy, an intermediate solution that involves hydrogen – natural gas blends is promising. These blends are complex mixtures and more experimental data is needed to extend existing models and evaluate their performance.

In this work the first objective was to identify a model based on the Peng-Robinson EoS that couples high accuracy with low complexity for the prediction of pure hydrogen's thermodynamic and thermophysical properties. Among various alpha functions examined, it was found that the Soave proposed one using the NIST proposed acentric factor achieves high accuracy both in the subcritical and in the supercritical region while having a low level of complexity. While it is possible to obtain higher accuracy results with other alpha functions, like the Mathias-Copeman one, if the parameters are regressed to experimental data, the compliance to the consistency criteria developed for the alpha functions has to be compromised. The other model compared in this work, SAFT-VRQ-Mie outperforms Peng-Robinson in most properties examined in the supercritical temperature range, namely in density, speed of sound and Joule-Thompson although Peng-Robinson yields better results in the subcritical region except for the saturated liquid density calculations. Due to SAFT-VRQ-Mie's high complexity, Peng-Robinson is more suitable for use in a wider variety of software.

Overall, in the saturation area, the accuracy of the Peng-Robinson calculations regarding the vapor pressure, saturated vapor volume and saturated liquid volume with volume translation is satisfactory although the average deviations are larger than 3.5%.

In the supercritical region, the accuracy of the examined properties' calculations increases with temperature. It was found that the prediction for the isobaric heat capacity, the speed of sound and the Joule Thomson coefficient is poor below 100 K. In relation to pressure, each property is affected differently, with speed of sound exhibiting the largest deviations in very high pressures, above 1000 bar. The accuracy of the isobaric heat capacity and the calculations is also compromised at high pressures. Overall, the isobaric heat capacity and the speed of sound at lower supercritical temperatures are the hardest properties to describe precisely by the model.

The introduction of the volume translation leads to important improvement in the density calculations, as expected, and also improves the Joule-Thomson coefficient but degrades the speed of sound calculations.

Taking into consideration the above observations, Peng-Robinson with the NIST proposed acentric factor employed is recommended for calculations of properties of pure hydrogen, especially when examining the saturation area. For applications, however, that higher accuracy is needed in supercritical property calculations and there are no limitations in the computational complexity, the SAFT-VRQ-Mie model is suggested.

The second objective of this work was to modify the Peng-Robinson EoS to accurately predict the vapor liquid equilibrium (VLE) of binary mixtures of hydrogen with various compounds of interest. The introduction of a temperature dependency in the binary interaction coefficient is necessary to improve the model's performance, as it has been stated in literature and confirmed in this work. Generally, higher temperatures and heavier – more asymmetric in relation to hydrogen – compounds, require higher values for the coefficient. In addition, it has been confirmed that the cubic EoS fails to accurately predict the phase envelope at high pressures. That is where the largest deviations from experimental data are noted, as the model cannot reproduce the curvature of the phase envelope there.

Out of the binary mixtures examined, the ones with methane and ethane exhibited the largest deviations from experimental data in VLE calculations, using all types of binary interaction coefficients. The higher deviation in the binary mixture with methane is linked to the higher experimental uncertainty of the datasets used. Regarding ethane, the large deviation is attributed to the presence of many experimental points at high pressures that greatly influence the regression.

Focusing on the bubble point calculations, the trendlines derived from the regression of the experimental data yield deviations close to the ones obtained from the optimal k_{ij} calculations. The discrepancy in the deviations highlights the effect of the different experimental uncertainty between different researchers, and consequently different methods of measuring data. It is important to note that the trendlines derived in this work are suitable for application in the temperature range that the binary interaction coefficients were regressed in, as well as a small extrapolation in lower and higher temperatures. To ensure safe extrapolation in lower temperatures, some pseudovalues were added in certain mixtures that exhibited a second degree polynomial trendline that would project a non-physical minimum in a high temperature. The use of pseudovalues however leads to a shift in the curvature of the regressed trendline, leading to a compromise in the efficiency of the developed model. Extension to temperatures well above or below the examined temperature ranges does not guarantee efficient performance of the model as there is a lack of experimental data that could have been used in the regressions.

As far as the vapor phase composition is concerned, overall, the trendline replicates in higher accuracy the optimal calculations, compared to the bubble point pressure. The performance of the model is efficient even though the objective function employed for its development did not take into consideration the vapor phase composition. The largest deviations from experimental data are observed in the hydrogen – methylcyclohexane mixture. There is no clear effect of the mixture asymmetry in the prediction of the vapor phase composition. It is important to note however, that the average deviations calculate,

regard a smaller number of points compared to the vapor phase composition. That is because there was a significant lack of experimental data in various mixtures, as well as complete lack in others e.g. H_2- nC6, H_2 -nC10 and H_2-pxylene.

In general, it was confirmed that the introduction of a temperature dependency on the binary interaction coefficient results to significant improvement in the VLE predictive capabilities of Peng-Robinson. That becomes evident as the temperature-dependent coefficient exhibits a broad range of values to achieve optimal calculations while the temperature-independent coefficient, represented by a single value, cannot account for the extensive variability exhibited by the first one.

The model chosen for validating the efficiency of the developed trendlines in this work is UMR-PRU which exhibits much higher accuracy in the bubble point pressure calculations in the binary mixtures with methane and ethane, as these compounds consist of only one group according to the grouping method used in the development. The vapor phase composition is predicted with comparable accuracy for both models. For VLE calculations of binary mixtures therefore the UMR-PRU model is recommended when the second compound is either methane or ethane, and the trendlines developed in this work are recommended for other binaries.

7 Further Work

In this work 15 binary mixtures of interest in the hydrogen technology were examined. There are however, many more compounds that need to be examined, as CO, N_2, H_2S which are also components of natural gas and therefore coexist with hydrogen in natural gas blends. Another compound of interest is NH_3 which is a promising hydrogen carrier used for the transport of hydrogen. In addition, a value for the temperature-independent binary interaction coefficient has been suggested for hydrocarbons with a carbon number great than 10, but it would be interesting to also examine the temperature dependency of the coefficient in such compounds.

In this work, while describing the vapor-liquid equilibrium of hydrogen binary mixtures, two separate correlations have been identified: one between the binary interaction coefficient and the temperature, and another between the coefficient and the carbon number of linear hydrocarbons. In further work, it would be highly valuable to develop a unified equation that correlates both the temperature and the carbon number with the binary interaction coefficient. This would enable the proposal of a suitable coefficient for accurately describing the vapor-liquid equilibrium of hydrogen binary mixtures at any given temperature and carbon number.

Additionally, it would be interesting to test the derived trendlines in calculations regarding thermodynamic and thermophysical properties of binary mixtures. It is important to note however that there is a lack of experimental data for properties such as isobaric heat capacities, speed of sounds etc. for a lot of the binary mixtures examined in this work.

The trendlines derived in this work can be used in the temperature range of the experimental data used in their development. Extrapolations are possible but only in a short range. To ensure the efficient performance of the model in an extended temperature range, more experimental data would need to be used for regression. This could also alter the type of regression required, increasing the complexity of the model.

The cryogenic region in particular, is of great importance in the hydrogen technology but there is a lack of experimental data there. This highlights the need for the conduction of measurements in cryogenic conditions so that existing and new models can be modified to be applied to cryogenic processes.

Regarding pure hydrogen's properties, in this work a temperature-and-pressure-independent volume translation was introduced for the improvement of the accuracy of the model. As it was observed, this volume translation resulted in improvement in some of the properties but also led to poorer performance in properties such as the speed of sound or in certain conditions in other properties. An implementation of a temperature-dependent volume translation would improve the results, however it is not advised as it is not considered as a consistent thermodynamic approach [13].

References

1.   Dawood, F., M. Anda, and G.M. Shafiullah, *Hydrogen production for energy: An overview.* International Journal of Hydrogen Energy, 2020. **45**(7): p. 3847-3869.

2.   Lozano-Martín, D., A. Moreau, and C.R. Chamorro, *Thermophysical properties of hydrogen mixtures relevant for the development of the hydrogen economy: Review of available experimental data and thermodynamic models.* Renewable Energy, 2022. **198**: p. 1398-1429.

3.   Nikolaidis, P. and A. Poullikkas, *A comparative overview of hydrogen production processes.* Renewable and Sustainable Energy Reviews, 2017. **67**: p. 597-611.

4.   United Nations; Available from: https://unfccc.int/process-and-meetings/the-paris-agreement?gclid=CjwKCAjw4ZWkBhA4EiwAVJXwqdhQ1Trm6foIQYkDFxr7BpJJ1dheNPDnm85PnlRlunxlit6WRdYOXhoCZN4QAvD_BwE.

5.   Abdin, Z., et al., *Hydrogen as an energy vector.* Renewable and Sustainable Energy Reviews, 2020. **120**: p. 109620.

6.   Kumar, A., et al., *Absorption based solid state hydrogen storage system: A review.* Sustainable Energy Technologies and Assessments, 2022. **52**: p. 102204.

7.   Linde Engineering; Available from: https://www.engineering.linde.com/h2101?utm_source=YouTube&utm_medium=Video&utm_campaign=powerfuture.

8.   Le Guennec, Y., et al., *A consistency test for α-functions of cubic equations of state.* Fluid Phase Equilibria, 2016. **427**: p. 513-538.

9.   Soave, G., *Equilibrium constants from a modified Redlich-Kwong equation of state.* Chemical Engineering Science, 1972. **27**(6): p. 1197-1203.

10. Mathias, P.M. and T.W. Copeman, *Extension of the Peng-Robinson equation of state to complex mixtures: Evaluation of the various forms of the local composition concept.* Fluid Phase Equilibria, 1983. **13**: p. 91-108.

11. Twu, C.H., J.E. Coon, and J.R. Cunningham, *A new cubic equation of state.* Fluid Phase Equilibria, 1992. **75**: p. 65-79.

12. Voutsas, E., et al., *Thermodynamic Modeling of Natural Gas and Gas Condensate Mixtures.* 2018. p. 57-88.

13. Jaubert, J.-N., et al., *Note on the properties altered by application of a Péneloux–type volume translation to an equation of state.* Fluid Phase Equilibria, 2016. **419**: p. 88-95.

14. Voutsas, E., K. Magoulas, and D. Tassios, *Universal Mixing Rule for Cubic Equations of State Applicable to Symmetric and Asymmetric Systems: Results with the Peng–Robinson Equation of State.* Industrial & Engineering Chemistry Research, 2004. **43**(19): p. 6238-6246.

15. Fredenslund, A., R.L. Jones, and J.M. Prausnitz, *Group-contribution estimation of activity coefficients in nonideal liquid mixtures.* AIChE Journal, 1975. **21**(6): p. 1086-1099.

16. Koulocheris, V., et al., *Modelling of hydrogen vapor-liquid equilibrium with oil & gas components.* Fluid Phase Equilibria, 2019. **494**: p. 125-134.

17. Aasen, A., et al., *Equation of state and force fields for Feynman–Hibbs-corrected Mie fluids. I. Application to pure helium, neon, hydrogen, and deuterium.* The Journal of Chemical Physics, 2019. **151**(6): p. 064508.

18. Aasen, A., et al., *Equation of state and force fields for Feynman–Hibbs-corrected Mie fluids. II. Application to mixtures of helium, neon, hydrogen, and deuterium.* The Journal of Chemical Physics, 2020. **152**(7): p. 074507.

19. Turns, S.R. and L.L. Pauley, *Thermodynamics: Concepts and Applications*. 2 ed. 2020, Cambridge: Cambridge University Press.

20. Sakoda, N., et al., *Review of the Thermodynamic Properties of Hydrogen Based on Existing Equations of State.* International Journal of Thermophysics, 2010. **31**(2): p. 276-296.

21. Jacobsen, R.T., et al., *Current Status of Thermodynamic Properties of Hydrogen.* International Journal of Thermophysics, 2007. **28**(3): p. 758-772.

22. Leachman, J.W., et al., *Fundamental Equations of State for Parahydrogen, Normal Hydrogen, and Orthohydrogen.* Journal of Physical and Chemical Reference Data, 2009. **38**(3): p. 721-748.

23. B.A. Younglove, *Thermophysical properties of fluids. I. Argon, ethylene, parahydrogen, nitrogen, nitrogen trifluoride, and oxygen*, J. Phys. Chem. Ref. Data 11 (Suppl. No. 1) (1982) 1–353

24. Aasen, A., et al., *Accurate quantum-corrected cubic equations of state for helium, neon, hydrogen, deuterium and their mixtures.* Fluid Phase Equilibria, 2020. **524**: p. 112790.

25. Kunz, O.K., R; Wagner, W; Jaeschke, M, *The GERG-2004 wide-range equation of state for natural gases and other mixtures*. 2007, Germany.

26. Kunz, O. and W. Wagner, *The GERG-2008 Wide-Range Equation of State for Natural Gases and Other Mixtures: An Expansion of GERG-2004.* Journal of Chemical & Engineering Data, 2012. **57**(11): p. 3032-3091.

27. Qian, J.-W., J.-N. Jaubert, and R. Privat, *Phase equilibria in hydrogen-containing binary systems modeled with the Peng–Robinson equation of state and temperature-dependent binary interaction parameters calculated through a group-contribution method.* The Journal of Supercritical Fluids, 2013. **75**: p. 58-71.

28. Wenchuan, W. and Z. Chongli, *Mixing rules for hydrogen-containing systems.* Fluid Phase Equilibria, 1989. **47**(1): p. 103-114.

29. Huang, H., S.I. Sandler, and H. Orbey, *Vapor-liquid equilibria of some hydrogen + hydrocarbon systems with the Wong-Sandler mixing rule.* Fluid Phase Equilibria, 1994. **96**(C): p. 143-153.

30. Ioannidis, S. and D.E. Knox, *Vapor-liquid equilibria predictions of hydrogen-hydrocarbon mixtures with the Huron-Vidal mixing rule.* Fluid Phase Equilibria, 1999. **165**(1): p. 23-40.

31. Twu, C.H., et al., *An approach for the application of a cubic equation of state to hydrogen-hydrocarbon systems.* Industrial and Engineering Chemistry Research, 1996. **35**(3): p. 905-910.

32. Mohammed, F., et al., *Generalized binary interaction parameters for hydrogen-heavy-n-alkane systems using Peng–Robinson equation of state.* Chemical Engineering Communications, 2018. **205**(9): p. 1226-1238.

33. Poling, B.E., J.M. Prausnitz, and J.P. O'Connell, *Properties of Gases and Liquids*. 5th Edition ed. 2001, New York: McGraw-Hill Education.

34. Benham, A.L. and D.L. Katz, *Vapor-liquid equilibria for hydrogen–light-hydrocarbon systems at low temperatures.* AIChE Journal, 1957. **3**(1): p. 33-36.

35.   Sagara, H., Y. Arai, and S. Saito, *VAPOR-LIQUID EQUILIBRIA OF BINARY AND TERNARY SYSTEMS CONTAINING HYDROGEN AND LIGHT HYDROCARBONS.* Journal of Chemical Engineering of Japan, 1972. **5**(4): p. 339-348.

36.   Hong, J.H. and R. Kobayashi, *Vapor-liquid equilibrium study of the hydrogen-methane system at low temperatures and elevated pressures.* Journal of Chemical & Engineering Data, 1981. **26**(2): p. 127-131.

37.   Tsang, C.Y., et al., *PHASE EQUILIBRIA IN THE H2/CH4 SYSTEM AT TEMPERATURES FROM 92.3 TO 180.0 K AND PRESSURES TO 140 MPa*.* Chemical Engineering Communications, 1980. **6**(6): p. 365-383.

38.   B. S. Kirk and W. T. Ziegler. *Proc. Int. Adv. Cryog. Eng. Conf.*, 10:160–170, 1965.

39.   Yorizane, M., et al., *Phase Behavior of Three Hydrogen-Containing Ternary Systems*, in *Advances in Cryogenic Engineering*, K.D. Timmerhaus and H.A. Snyder, Editors. 1980, Springer US: Boston, MA. p. 654-661.

40.   Hu, M., et al., *Isothermal vapor–liquid equilibrium in CH4/H2/N2 system at a cryogenic temperature range from 100.0K to 125.0K.* Fluid Phase Equilibria, 2014. **366**: p. 16-23.

41.   Hiza, M., C. Heck, and A. Kidnay. *Liquid-vapor and solid-vapor equilibrium in the system hydrogen-ethane*. in *Advances in Cryogenic Engineering: Proceedings of the 1967 Cryogenic Engineering Conference Stanford University Stanford, California August 21–23, 1967*. 1995. Springer.

42.   Williams, R.B. and D.L. Katz, *Vapor-Liquid Equilibria in Binary Systems. Hydrogen with Ethylene, Ethane, Propylene, and Propane.* Industrial & Engineering Chemistry, 1954. **46**(12): p. 2512-2520.

43.   Heintz, A. and W.B. Streett, *Phase equilibriums in the hydrogen/ethane system at temperatures from 92.5 to 280.1 K and pressures to 560 MPa.* Journal of Chemical & Engineering Data, 1982. **27**(4): p. 465-469.

44.   Burriss, W.L., et al., *Phase Behavior of the Hydrogen-Propane System.* Industrial & Engineering Chemistry, 1953. **45**(1): p. 210-213.

45.   Trust, D.B. and F. Kurata, *Vapor-liquid phase behavior of the hydrogen-propane and hydrogen-carbon monoxide-propane systems.* AIChE Journal, 1971. **17**(1): p. 86-91.

46.   Aroyan, H.J. and D.L. Katz, *Low Temperature Vapor-Liquid Equilibria in Hydrogen-n-Butane System.* Industrial & Engineering Chemistry, 1951. **43**(1): p. 185-189.

47.   Klink, A.E., H.Y. Cheh, and E.H. Amick Jr, *The vapor-liquid equilibrium of the hydrogen—n-butane system at elevated pressures.* AIChE Journal, 1975. **21**(6): p. 1142-1148.

48.   Nelson, E.E. and W.S. Bonnell, *Solubility of Hydrogen in n-Butane.* Industrial & Engineering Chemistry, 1943. **35**(2): p. 204-206.

49.   Connolly, J.F. and G.A. Kandalic, *Gas solubilities, vapor-liquid equilibria, and partial molal volumes in some hydrogen-hydrocarbon systems.* Journal of Chemical & Engineering Data, 1986. **31**(4): p. 396-406.

50.   Freitag, N.P. and D.B. Robinson, *Equilibrium phase properties of the hydrogen—methane—carbon dioxide, hydrogen—carbon dioxide—n-pentane and hydrogen—n-pentane systems.* Fluid Phase Equilibria, 1986. **31**(2): p. 183-201.

51.   Brunner, E., *Solubility of hydrogen in 10 organic solvents at 298.15, 323.15, and 373.15 K.* Journal of Chemical & Engineering Data, 1985. **30**(3): p. 269-273.

52.   Gao, W., R.L. Robinson, and K.A.M. Gasem, *Solubilities of Hydrogen in Hexane and of Carbon Monoxide in Cyclohexane at Temperatures from 344.3 to 410.9 K and*

Pressures to 15 MPa. Journal of Chemical & Engineering Data, 2001. **46**(3): p. 609-612.

53. Peramanu, S. and B.B. Pruden, *Solubility study for the purification of hydrogen from high pressure hydrocracker off-gas by an absorption-stripping process.* The Canadian Journal of Chemical Engineering, 1997. **75**(3): p. 535-543.

54. Connolly, J.F. and G.A. Kandalic, *Thermodynamic properties of solutions of hydrogen in n-octane.* The Journal of Chemical Thermodynamics, 1989. **21**(8): p. 851-858.

55. Park, J., R.L.J. Robinson, and K.A. Gasem, *Solubilities of hydrogen in heavy normal paraffins at temperatures from 323.2 to 423.2 K and pressures to 17.4 MPa.* Journal of Chemical and Engineering Data, 1995. **40**(1): p. 241-244.

56. Schofield, B.A., Z.E. Ring, and R.W. Missen, *Solubility of hydrogen in a white oil.* The Canadian Journal of Chemical Engineering, 1992. **70**(4): p. 822-824.

57. Spano, J.O., C.K. Heck, and P.L. Barrick, *Liquid-vapor equilibria of the hydrogen-carbon dioxide system.* Journal of Chemical & Engineering Data, 1968. **13**(2): p. 168-171.

58. D. R. Augood. *Trans. Inst.* Chem. Eng., 35:394–408, 1957.

59. Kaminishi, G.-i. and T. Toriumi, *Vapor-Liquid Phase Equilibrium in the CO2-112, C O2-N2 and CO2-02 Systems.* The Journal of the Society of Chemical Industry, Japan, 1966. **69**(2): p. 175-178.

60. Fandiño, O., J.P.M. Trusler, and D. Vega-Maza, *Phase behavior of (CO2+H2) and (CO2+N2) at temperatures between (218.15 and 303.15)K at pressures up to 15MPa.* International Journal of Greenhouse Gas Control, 2015. **36**: p. 78-92.

61. Connolly, J.F., *Thermodynamic Properties of Hydrogen in Benzene Solutions.* The Journal of Chemical Physics, 2004. **36**(11): p. 2897-2904.

62. Park, J., R.L. Robinson Jr, and K.A.M. Gasem, *Solubilities of hydrogen in aromatic hydrocarbons from 323 to 433 K and pressures to 21.7 MPa.* Journal of Chemical and Engineering Data, 1996. **41**(1): p. 70-73.

63. Thompson, R.E. and W.C. Edmister, *Vapor-liquid equilibria in hydrogen-benzene and hydrogen-cyclohexane mixtures.* AIChE Journal, 1965. **11**(3): p. 457-461.

64. Sattler, H., *Solubility of hydrogen in liquid hydrocarbons.* Z. Tech. Phys, 1940. **21**: p. 410-413.

65. Krichevsky, I.R. and J.S. Kasarnovsky, *Thermodynamical Calculations of Solubilities of Nitrogen and Hydrogen in Water at High Pressures.* Journal of the American Chemical Society, 1935. **57**(11): p. 2168-2171.

66. Brainard, A.J. and B. Williams, *Vapor-liquid equilibrium for the system hydrogen—benzene—cyclohexane—n-hexane.* AIChE Journal, 1967. **13**(1): p. 60-69.

67. Laugier, S., D. Richon, and H. Renon, *Vapor-liquid equilibriums of hydrogen-2,2,4-trimethylpentane and hydrogen-toluene systems at high pressures and temperatures.* Journal of Chemical & Engineering Data, 1980. **25**(3): p. 274-276.

68. Simnick, J.J., et al., *Solubility of hydrogen in toluene at elevated temperatures and pressures.* Journal of Chemical & Engineering Data, 1978. **23**(4): p. 339-340.

69. Yin, J.-Z. and C.-S. Tan, *Solubility of hydrogen in toluene for the ternary system H2+CO2+toluene from 305 to 343K and 1.2 to 10.5MPa.* Fluid Phase Equilibria, 2006. **242**(2): p. 111-117.

70. Simnick, J.J., et al., *Gas-liquid equilibrium in mixtures of hydrogen + m-xylene and + m-cresol.* The Journal of Chemical Thermodynamics, 1979. **11**(6): p. 531-537.

71.   Berty, T.E., H.H. Reamer, and B.H. Sage, *Phase Behavior in the Hydrogen-Cyclohexane System.* Journal of Chemical & Engineering Data, 1966. **11**(1): p. 25-30.

72.   Ronze, D., et al., *Hydrogen solubility in straight run gasoil.* Chemical Engineering Science, 2002. **57**(4): p. 547-553.

73.   Krichevskii, I. R., and Sorina, G. A., *Zh. Fiz. Khim.*, 32, 2080 (1958).

74.   Peter, S., *Phase Equilibrium in the Systems H_2-n-Heptane, H_2-Methyl Cyclohexame, and H_2-2, 2, 4-Trimethyl Pentane at Elevated Pressures and Temperatures.* Z. Physik. Chemm. Frankfurt, 1960. **24**: p. 103-118.

75.   Cosway, H.F. and D.L. Katz, *Low-temperature vapor-liquid equilibria in ternary and quaternary systems containing hydrogen, nitrogen, methane, and ethane.* AIChE Journal, 1959. **5**(1): p. 46-50.

76.   Young, C.L., *Hydrogen and deuterium.* Solubility Data Series, 1981. **5**: p. 428-429.

Appendix 1

Table 60: DIPPR proposed parameters for calculation of ideal isobaric heat capacity of hydrogen

A	B	C	D	E	Min T	Max T	Data Type	Error
2.76E+04	9.56E+03	2.47E+03	3.76E+03	5.68E+02	250	1500	Extrapolated	< 1%
A	B	C	D	E	Min T	Max T	Data Type	Error
6.50E+04	-7.88E+02	5.83E+00	-1.85E-02	2.16E-05	50	250	Experimental	< 3%

Table 61: NIST proposed parameters for calculation of ideal isobaric heat capacity of hydrogen

Temperature (K)	298. - 1000.	1000. - 2500.	2500. - 6000.
A	33.066178	18.563083	43.41356
B	-11.363417	12.257357	-4.293079
C	11.432816	-2.859786	1.272428
D	-2.772874	0.268238	-0.096876
E	-0.158558	1.97799	-20.533862
F	-9.980797	-1.147438	-38.515158
G	172.707974	156.288133	162.081354
H	0	0	0

Table 62: Poling et al. proposed parameters for calculation of ideal isobaric heat capacity of hydrogen

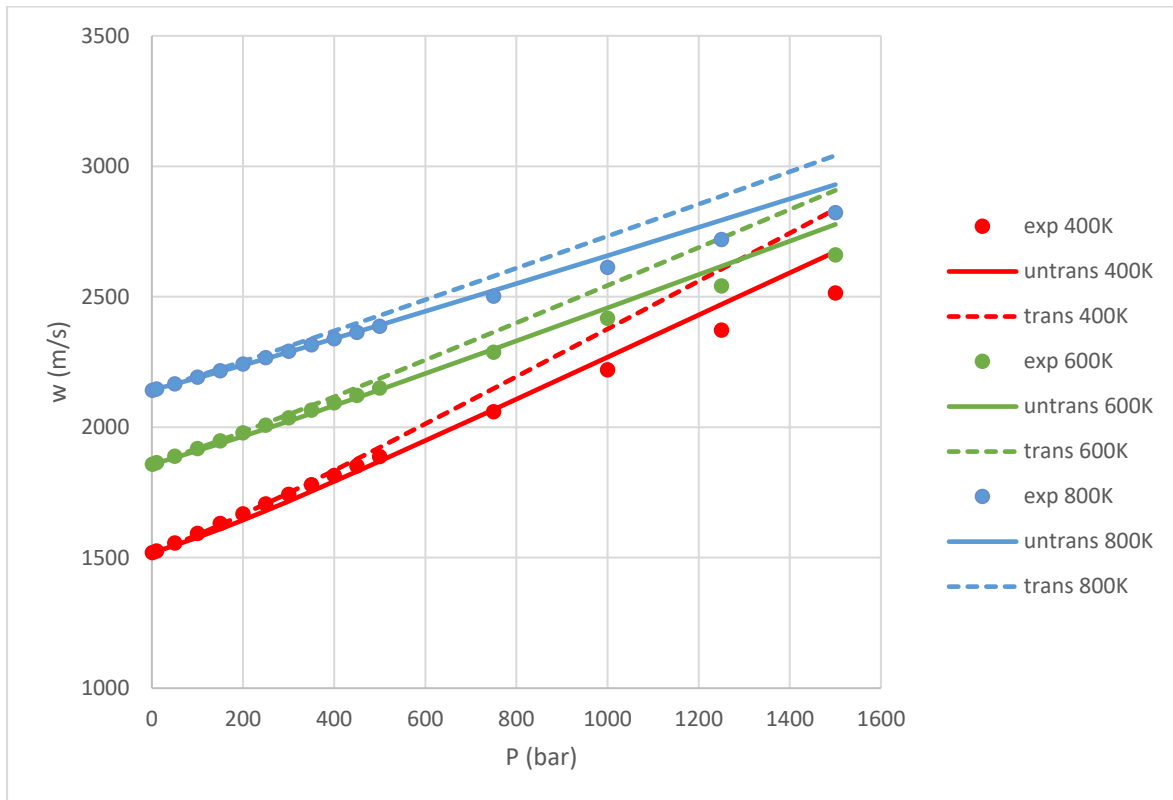| T range: 50-1000 K	
a0	2.883
a1	3.681e-3
a2	-0.772e-5
a3	6.92e-9
a4	-2.13e-12

Appendix 2

Figure 62: Speed of sound calculations for pure hydrogen at 400, 600, 800 K
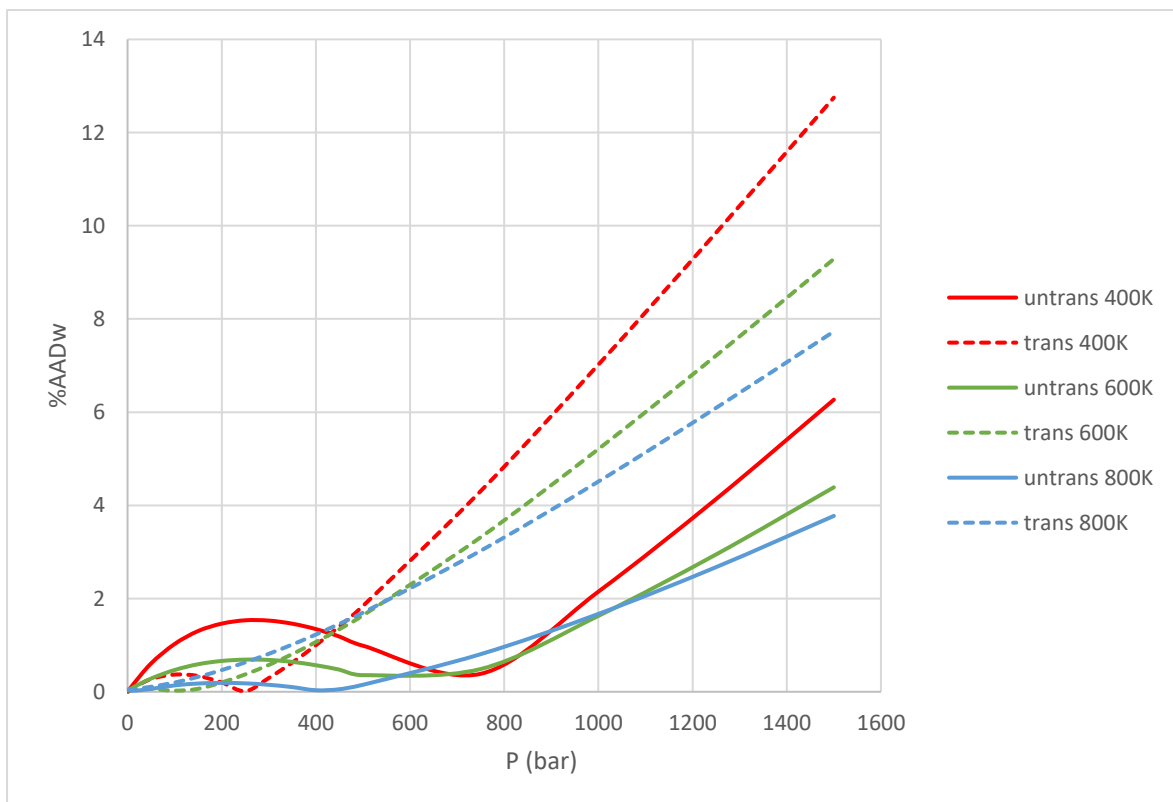

Figure 63: Speed of sound calculation deviations at 400, 600, 800 K
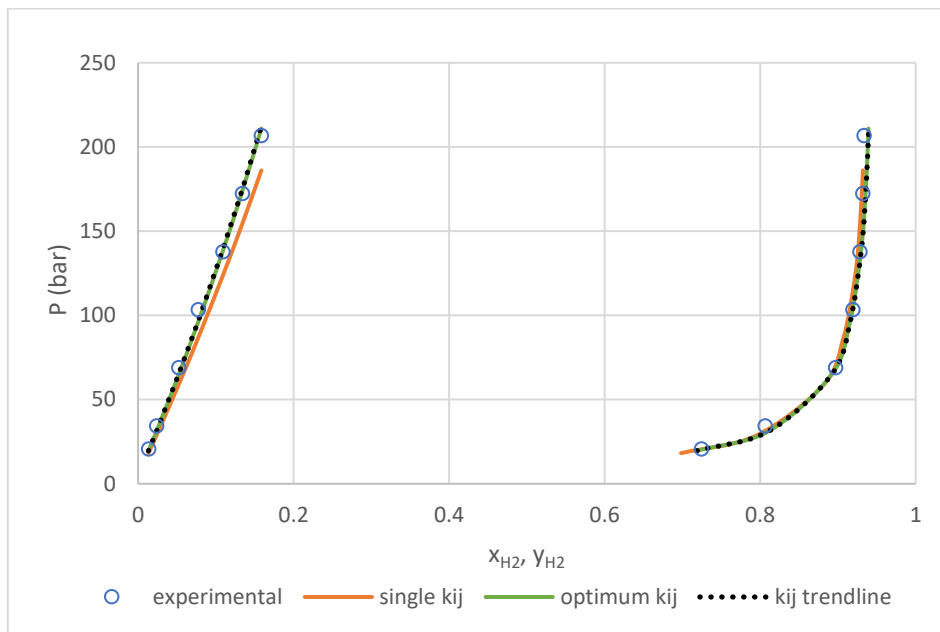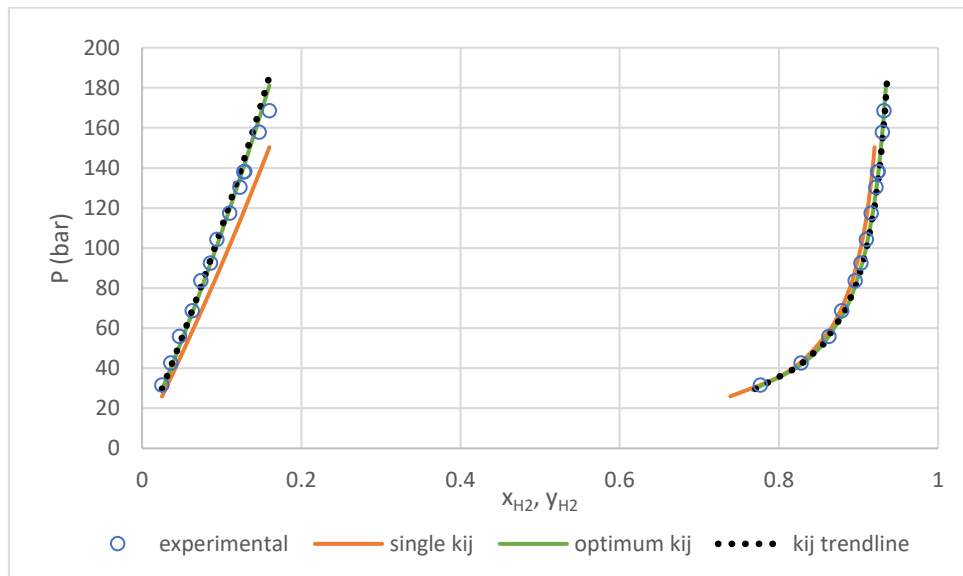
Appendix 3

Figure 66: VLE envelope for H_2 – C_3 in T=273.15K

Figure 67: VLE envelope for H_2 – nC_4 in T=327.65K